REVIEW ARTICLE

DOI: 10.1039/C9CS00594C

Electrical conductivity and magnetic bistability in metal–organic frameworks and coordination polymers: charge transport and spin crossover at the nanoscale

Víctor Rubio-Giménez,[a, b] Sergio Tatay[a] and Carlos Martí-Gastaldo*[a]

Materials scientists are currently shifting from purely inorganic, organic and silicon-based materials towards hybrid organic-inorganic materials to develop increasingly complex and powerful electronic devices. In this context, it is undeniable that conductive metal-organic frameworks (MOFs) and bi-stable coordination polymers (CPs) are carving a niche for themselves in the electronics world. The tunability and processability of these materials alongside the combination of electrical conductivity with porosity or spin transition offers unprecedented technological opportunities for their integration into functional devices. This review aims to summarise the chemical strategies that have guided the design of this type of materials and the identified opportunities for further development. We also examine the strategies to process them as thin films and stress the importance of analysing the effects of nanostructuration on their physical properties that might be crucial for device performance. Finally, we showcase relevant examples of functional devices that have received increasing attention from researchers and highlight the opportunities available for more sophisticated applications that could take full advantage of the combination of conductivity and magnetic bistability.

1. Introduction

Electronic devices shape the world as we know it. The tremendous technological advances that we experienced in the last 50 years relied on the progressive miniaturization of these devices and their components to construct increasingly complex and powerful platforms. This achievement has been possible thanks to low-cost production through scalable complementary metal-oxide-semiconductor (CMOS) microfabrication. However, traditional CMOS materials (metal chalcogenides) suffer from a fundamental design limitation due to the scarcity of usable inorganic anions. As a consequence, the electronics field is on the verge of a dramatic transition from a materials point of view. As suggested by the International Roadmap for Devices and Systems (IRDS),[1,2] the industry should move on from inorganic and silicon-based materials towards organic and hybrid organic-inorganic "beyond CMOS" materials that can improve existing properties and bring additional ones to the table. Presently, materials scientists are shifting from purely inorganic, organic and silicon-based materials towards hybrid organic-inorganic materials to construct increasingly complex and powerful electronic devices. In this context, it is undeniable that coordination polymers (CPs) and metal-organic frameworks (MOFs) are carving a niche for themselves in the electronics world amongst these "beyond CMOS" materials.

CPs are hybrid organic-inorganic systems that crystallize by the assembly of metal ions and polytopic organic ligands to form 2D or 3D extended structures. Compared to classical CMOS materials used in electronic devices, CPs combine the extended structure and high crystallinity of inorganic solids with the synthetic versatility (structural and electronic manipulation through chemical modification of ligands and metal clusters),[3,4] easy processability and mechanical flexibility[5,6] of organic materials. Furthermore, in some cases the structural disposition of metallic nodes and organic ligands creates voids or pores that can be occupied by gases or other guests. First reported as such by Robson and co-workers,[7] this particular class of CPs denoted as metal-organic frameworks (MOFs)[8,9] or porous coordination polymers (PCPs)[10] offer the possibility of indirectly manipulating their properties and even introduce extra functionalities simply by infiltration with active guests.[11] Nevertheless, most consolidated applications, employ MOFs as innocent non-active frameworks to store[12–17] or separate gases and other guests.[18,19] Later, the possibility to exploit pore chemistry emerged with the use of MOFs heterogeneous as catalysts.[20–22] Still, all the above applications are focused on the physical and chemical properties of the internal pores of MOFs while the rest of the framework remains in a secondary role. When MOFs and other CPs become fundamental parts of electronic devices an opposite situation takes place, the framework plays a central role in device performance, manipulating the electrons that come into contact with it. The way in which these systems interact with electrons is fundamentally manifested through their electronic properties, i.e. magnetism and electrical conductivity. Coincidently, MOFs and CPs offer a very competitive advantage to tune these properties by chemical design thanks to their molecular nature. Chemists have the capability of easily producing tailor-made materials with an almost infinite palette of ligands and metal ion combinations. Furthermore, the connectivity in between them can also be altered, and in the case of MOFs there is the option of incorporating functional guests into the pores. Nevertheless, material design and bulk synthesis is only the first step in the device integration course. The subsequent one being processing

[a] Instituto de Ciencia Molecular, Universitat de València, Catedrático José Beltrán 2, 46980 Paterna, Spain. E-mail: carlos.marti@uv.es
[b] Centre for Membrane Separations, Adsorption, Catalysis, and Spectroscopy for Sustainable Solutions (cMACS), Department of Microbial and Molecular Systems, KU Leuven, Celestijnenlaan 200F, Leuven 3001, Belgium.
See DOI: 10.1039/C9CS00594C

these active materials into nanometric thin films to be integrated in the final electronic devices.

In this review, we re-examine the different approaches to render MOFs and CPs materials electrically conductive, as well as the strategies to nanostructure and process them as thin films to act as active interfaces in electronic devices. In this sense, various reviews have recently highlighted their potential[23–28] centring around the electronic properties of MOFs and CPs. However, most of them miss out on a second relevant property: magnetism, and mostly on the interplay between both electronic and magnetic properties of these materials. Regarding magnetic properties, we center on magnetic bistability as mainly represented by spin crossover (SCO), the magnetic propertythat has received the most attention from a device point of view for MOFs and CPs. These bi-stable materials have great potential for the development of functional nanodevices,[29] provided that the critical effects of nanostructuration (particle size reduction, crystallinity, interparticle organization, surface defects, etc.) on the spin transition are well understood along with the electronic properties of the respective spin states. In other words, comprehending how the spin state may impact the electrical response of the SCO material in a device setting.

Finally, we examine a selection of the most prominent examples of working devices based on MOFs and CPs, which in our eyes exemplify the potential perspectives of device integration for these materials. The search for novel crystalline polymeric materials and their nanostructuration into electronic devices is a challenging task ahead of chemists, physicists and chemical engineers. This review aims to reassess the steps taken so far towards integrating CPs and MOFs as active components in electronic and bi-stable devices. To the best of our knowledge, no other published review highlights the importance of processing MOFs and CPs as high-quality ultrathin films together with the careful examination of their electronic and magnetic properties at the nanoscale, the ultimate target being the fabrication of functional nanodevices.

2. Electrical conductivity in framework materials

This property measures the ability of a material to conduct electrical current, that is, the ease with which charge carriers (electrons or holes) can travel across it. The magnitude experimentally measured is conductivity (σ; units: $S \cdot cm^{-1}$ or $\Omega^{-1} \cdot cm^{-1}$) which is the inverse of resistivity (ρ), an intrinsic property of materials calculated by taking into account the geometrical dimensions of the sample (length between the contacts and cross-sectional area) and its electrical resistance (R) at a given voltage (V). In principle, the highly ordered crystal structure of MOFs or CPs warrants the application of band theory to rationalize their electrical conductivity and electronic structure. According to it, the discrete energy levels that an electron can occupy in an ordered solid merge to form continuous energy bands. At absolute zero, the filled bands are referred to as the valence band (VB), while the unoccupied band with the lowest energy is the conduction band (CB).[30] Thus, solids can be generally classified as metals, semiconductors and insulators (**Figure 1**) owing to their respective electronic band structures and the separation between the maximum of the VB and the CB minimum, defined as the bandgap (E_g). In metallic conductors the CB and VB overlap ($E_g = 0$), the Fermi level (E_F) crosses a partially filled band and all the electrons are free charge carriers. Owing to its high charge density the electrical conductivity is in turn very high. For semiconductors and insulators there is an energy gap, which is small for semiconductors ($0 < E_g < 3$ eV) and large for insulators ($E_g > 3$ eV). However, the boundary between the two is sometimes blurry as large bandgap semiconductors are considered insulators or vice versa and additional information about the conduction mechanism has to be gathered as discussed below. In these cases, the Fermi level is located in the energy gap between the VB and the CB, either in the middle (intrinsic semiconductors), closer to the VB (p-type semiconductor) or closer to the CB (n-type semiconductor). The energy difference between the Fermi level and the VB maximum or the CB maximum is the activation energy (E_a). At finite temperature, VB electrons can be thermally promoted into the CB, leaving holes in the VB. Both electrons and holes become free charges. Therefore, the conductivity increases with temperature in the case of semiconductors. Solids with different band structures will yield different electrical conductivity values depending also on the mobility of electrons and holes, which reflects the efficiency of the charge transport.

Charge carriers in a crystal are not completely free to move, but instead interact with the periodic potential of the lattice. Poorer orbital overlaps will lead to higher interactions and lower mobility. Moreover, a high density of charge scattering sites, such as disorder, defects, impurities or grain boundaries will further reduce carrier mobility to the point that charge carriers will become localized at specific sites with discrete energy levels, and charge transport will be possible only when charge carries hop

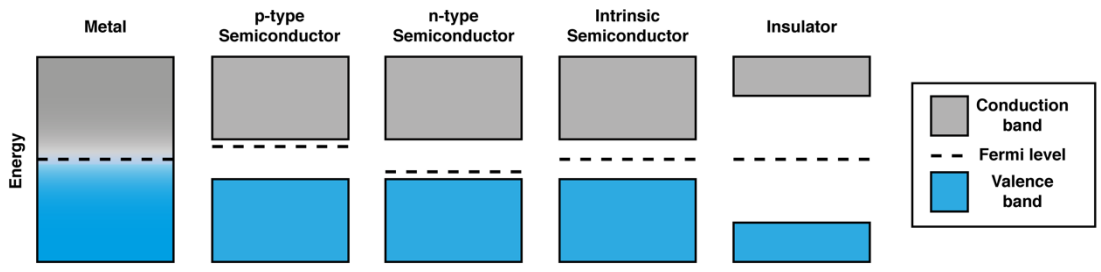

Figure 1. Schematic band structure representations of the different types of solids.

between neighbouring sites with hopping probability scaling with temperature. However, the magnitude of this dependence can be different to that expected for band transport regime. In general, band transport yields higher charge mobility and higher conductivity than hopping. From a design perspective, both modes of transport require good spatial and energetic overlap between orbitals of appropriate symmetry.

Despite being fundamental for their device integration, the ability to transport charge carriers through 2D or 3D CPs and MOFs has not been studied as in-depth as their purely organic counterparts,[31–34] especially if we include graphene[35–39] and other carbon nanoforms[40–43] in the latter group. In fact, the popularity of these materials in electronics does not compare with the explosion of low dimensional materials during the last decade. Traditionally, conductivity has not been a targeted property in CPs (except in 1D metal-organic wires)[44] and specially in MOFs, so most of them are composed of hard metal ions and redox innocent organic ligands which does not favour charge carrier mobility. Thus, most CPs qualify as insulators, due to their low conductivity at room temperature. However, in the last decade this situation has started to change with the appearance of various strategies to produce highly conductive CPs[27,44–46] and specially MOFs.[26,47–56] This has allowed researchers to envision the future integration of these materials as active elements in functional electronic devices.[24,25,57,58] Next, a brief description and classification of the different mechanistic approaches for conductive MOFs and CPs is presented. This section is directed towards familiarizing the reader with the materials and approaches for the subsequent discussion on nanostructuration strategies, combination with magnetic bistability and serves to hightlight the relative immaturity of the field. For more comprehensive assesments of electrical conductivity in framework materials, we direct the reader to the recent specific reviews on the matter.[52–55]

2.1. Guest-induced conductivity

The guest-induced conductivity approach can obviously be used only with porous materials. In this tactic, an insulating network is turned conductive thanks to an adsorbed guest molecule, organic polymer or metallic nanoparticle. The obvious downside of this strategy is that a fraction of the MOF's porosity is sacrificed at the cost of electrical conductivity. In some cases, the guest is itself conductive, and simply provides a viable channel for charge transport to go through, while in others the guest induces, either a redox transformation (leading to the generation of charge carriers within the framework) or structural transformations resulting in new conductive pathways that make the previously insulating framework conductive.

2.1.1. Infiltration of conductive guests

When metal nanoparticles (NPs), nanoclusters (NC) or conductive organic polymers (**Figure 2**) are infiltrated into a MOF, they do not interact with the framework to create additional conductive channels but act as conductive channels of their own. As visible in **Figure 2a**, Grzybowski *et al.* infiltrated Rb-CD-MOF with $AgNO_3$ which spontaneously reduced in the pores to form Ag nanoclusters (Ag-NCs).[59] Charge transport (σ = $2.15 \cdot 10^{-7}$ $S \cdot cm^{-1}$ upon light irradiation) then occurred via tunnelling between the spatially separated Ag-NCs that did not entirely fill the pores, thus the MOF was still porous afterwards (BET > 600 $m^2 \cdot g^{-1}$). This light-assisted tunnelling conductivity was reproduced in NC-loaded MIL-53 crystals as well.[59] A more sophisticated methodology was recently used by Farha, Hupp and collaborators who grew continuous strands tetratin(IV)oxy clusters along the pore channels of NU-1000 (**Figure 2b**).[60] However, the final material displayed similar conductivity (σ =

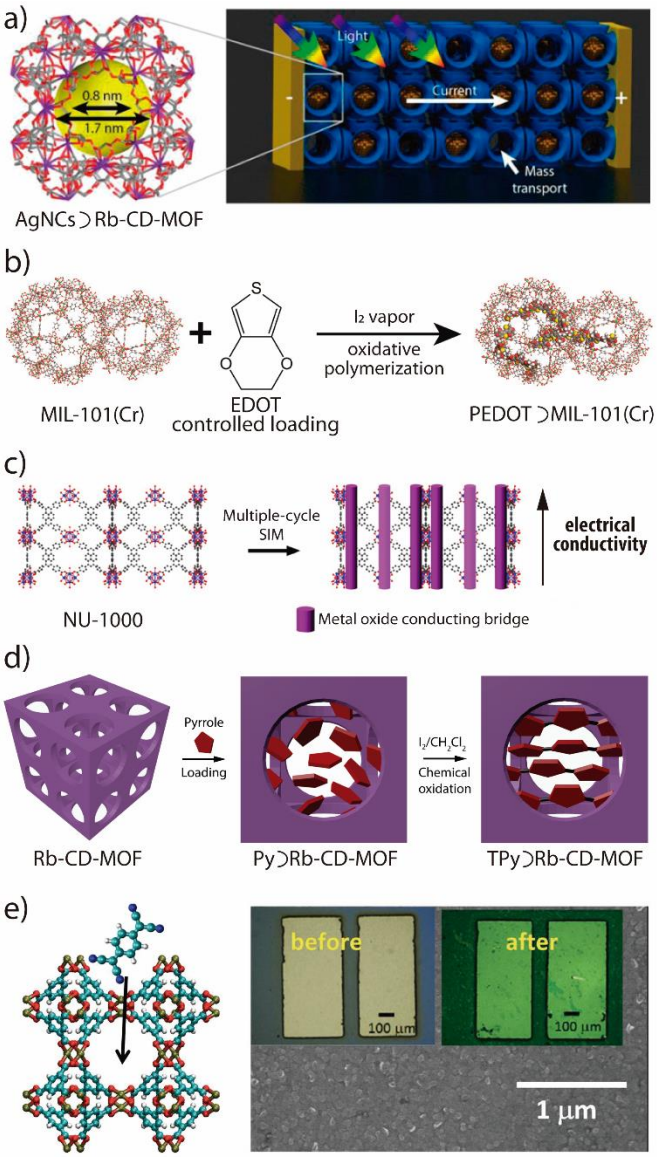

Figure 2. Different variants of the guest-induced conductivity strategy. a) Infiltration with metallic NCs (Ag-NCs). b) Generation of a conductive metal oxide strands. c) Generation of a conductive polymer in the MOF pores. d) Generation of charge transfer salts templated by the framework host-guest chemistry. e) Infiltration with a redox-active, conjugated guest molecule (TCNQ). a) Reproduced from ref. 80 with permission from American Association for the Advancement of Science, copyright 2014. b) Reproduced from ref. 59 with permission from American Chemical Society, copyright 2015. c) Reproduced from ref. 63 with permission from American Chemical Society, copyright 2016. d) Reproduced from ref. 60 with permission from American Chemical Society, copyright 2018. e) Reproduced from ref. 65 with permission from Wiley, copyright 2019.

$1.8 \cdot 10^{-7}$ S·cm^{-1}) and is less porous (BET = 650 m^2·g^{-1}) than the NiCB⊃NU-1000 system (see below).[61] Lastly, in the category of conductive polymers as guests, there are examples with polypyrrole (PPy), polyethylenedioxythiophene (PEDOT) and polythiophene (PT). Similar conductivities were achieved in PPy⊃[Cd(NDC)$_{0.5}$(PCA)][62] (σ = $1 \cdot 10^{-3}$ S·cm^{-1}; H_2NDC = 2,6-naptha–lenedicarboxylic acid; HPCA: 4-pyridinecarboxylic acid) and PEDOT⊃Cr-MIL-101 (σ = $1.1 \cdot 10^{-3}$ S·cm^{-1}, **Figure 2c**),[63] but only the latter maintained a high porosity (BET = 803 m^2·g^{-1}). For PT⊃NU-1000 the retained porosity was much larger (BET = 1560 m^2·g^{-1}) but the conductivity was again relatively low (σ = $1.3 \cdot 10^{-7}$ S·cm^{-1}) for this particular Zr-MOF system.[64] Martí-Gastaldo and co-workers also demonstrated the possibility of restricting the growth of polypyrrole by confined oxidation of pyrrole (Py) monomers after encapsulation in Rb-CD-MOF to generate terpyrrole (TPy) charge transfer salts (**Figure 2d**).[65] Whereas Rb-CD-MOF and Rb-CD-MOF⊃Py behave as insulators (σ = 10^{-11}-10^{-12} S·cm^{-1}), Rb-CD-MOF⊃TPy displays a million-fold enhancement of the electrical conductivity up to $5 \cdot 10^{-6}$ S·cm^{-1}. More recently, Ballav and co-workers polymerized PEDOT and PPy inside the pores of UiO-66. Hence, boosting its conductivity up to $2 \cdot 10^{-2}$ S·cm^{-1} for PPy⊃UiO-66 and 10^{-3} S·cm^{-1} for PEDOT⊃UiO-66. Moreover, thanks to the polymerization mainly taking place in one of the pores of UiO-66, the infiltrated MOFs also kept 69% (PPy⊃UiO-66) and 57% (PEDOT⊃UiO-66) of the original BET values. In all three cases, the MOF was first infiltrated with oligomers that were later polymerized inside the pores.[66]

2.1.2. Infiltration of non-conductive guests

The first example of this strategy was reported by Zeng *et al.* in 2010, the insulating [Zn_3($_{DL}$-lac)$_2$(pybz)$_2$] ($_{DL}$-lac = lactate; pybz = 4-pyridylbenzoate) was turned semiconductive (σ = $3.4 \cdot 10^{-3}$ S·cm^{-1}) by loading the pores with I_2.[67] Afterwards, the I_2-doping strategy has been successfully reproduced with a considerable number of insulating MOFs. The appearance of electrical conductivity was due to either donor-acceptor interactions between I_2 and ligand π electrons,[68–72] the oxidation of the network[73–75] or conduction through polyiodide ions.[76–78] Although in some of these conduction mechanisms were not clearly elucidated. It is worth mentioning the particular case of {[Cu_6(pybz)$_8$(OH)$_2$]·I_5^-·I_7^-}$_n$, directly synthesized with an array of polyiodide ions inside the framework.[79] Another variation of this strategy to tune electrical conductivity in MOFs is to infiltrate the nanopores with redox-active, conjugated guest molecules. Allendorf and co-workers demonstrated this by using thin-film devices of the MOF $Cu_3(BTC)_2$ (also known as HKUST-1; BTC, benzene-1,3,5-tricarboxylic acid) infiltrated with 7,7,8,8-tetracyanoquinododimethane (TCNQ).[80] An increase of over six orders of magnitude in electrical conductivity was achieved (**Figure 2e**), reaching values as high as $7 \cdot 10^{-2}$ S·cm^{-1}, tuneable by changing the exposure time to TCNQ solutions. Moreover, in this case, the MOF maintained a moderate porosity (BET = 214 m^2·g^{-1}) after guest infiltration. Spectroscopic data and first-principles modelling suggested that the conductivity arose from TCNQ guest molecules bridging the binuclear copper paddlewheels in the framework, leading to strong electronic coupling between the dimeric Cu subunits.[80] Later, Wöll and collaborators further clarified the conductivity mechanism with an extended hopping transport model in which carriers hop from guest to guest mediated by virtual occupancy of a MOF site.[81] This TCNQ-induced conductivity was successfully replicated by Loh *et al.* with a 2D Cu-porphyrin MOF.[82] Likewise, ferrocene has also been used as redox-active guest in HKUST-1 by Wöll and collaborators.[83,84] However, significantly lower conductivity values (σ = $2 \cdot 10^{-9}$ S·cm^{-1}) were obtained due to the larger size of ferrocene compared to TCNQ, which implies a lower guest loading in the pores. Finally, cationic methyl viologen,[85] metallacarboranes[61] and fullerene (C_{60})[86,87] have also been incorporated to MOFs to achieve conductivity via donor-acceptor interactions with the framework. Remarkably, in the second case, nickel(IV) bis(dicarbollide) was infiltrated in the micropores of NU-1000 leaving the larger mesopores free (BET = 1260 m^2·g^{-1} after infiltration), although the measured conductivity was rather moderate (σ = $2.7 \cdot 10^{-7}$ S·cm^{-1}).[61] Nevertheless, for the latter case, C_{60}⊃NU-901 exhibited even higher porosity (BET = 1550 m^2·g^{-1} after infiltration) and conductivity (σ = $1 \cdot 10^{-3}$ S·cm^{-1}) values.[86]

2.2. Intrinsic conductivity through the framework: through-space and through-bond approaches

As mentioned above, the other pathway to achieve MOF conductivity is to design intrinsically conductive frameworks. This can be more challenging from a synthetic point of view but has several advantages towards the guest-doping approach: i) The porosity is obviously preserved, ii) there is no need for post-synthetic modifications, which can have a negative effect on crystallinity, and most importantly iii) conductivity values are higher on average. In the intrinsically conductive MOFs and CPs group we can distinguish two different mechanisms: through-space and through-bond conduction.

2.2.1. Through-space conductivity

In the through-space approach, π-π stacking interactions between electroactive moieties in the framework offer

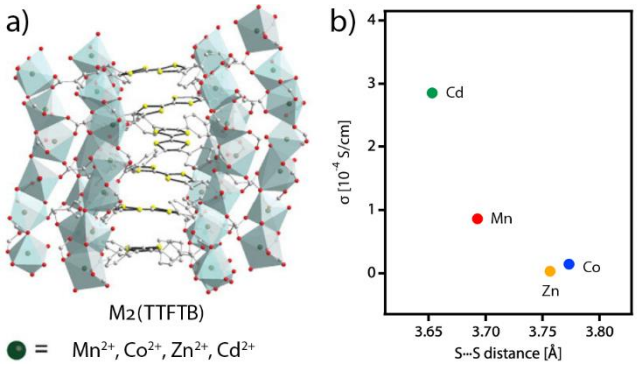

Figure 3. Example of through-space conductivity with TTF derivatives as ligands highlighting the importance of short contacts between the TTF motifs. a) Structure of the M_2(TTFTB)2 MOF reported by Dincă and co-workers. b) Correlation between the TTF motifs S···S distances and electrical conductivity in M_2(TTFTB). Adapted from ref. 97 with permission from American Chemical Society, copyright 2015.

conduction paths responsible for charge transport. The most widespread option to produce this type of conductive MOFs is the use of tetrathiafulvalene (TTF) derivatives as ligands, based on this molecule's huge popularity to prepare charge transfer salts and organic conductors.[88–91] Although examples of 1D metallic chains had appeared earlier,[44,92] the first examples of conductive TTF-based 2D or 3D CPs are non-porous and date back to 2002 with the report of Ag^{I} 3D CP with an S-donor TTF ligand.[93] After another example of a conductive Ag^{I} 3D with S-donor TTF ligands by Wang and co-workers in 2008,[94] the first family of CPs with carboxylate-TTFs was reported by Férey and collaborators. Among them MIL-135(K) presented the highest conductivity known to date for a TTF-based CP (σ = $1 \cdot 10^{-3}$ $S \cdot cm^{-1}$).[95] Then Dincă's group used extended carboxylate-TTFs to produce porous frameworks,[96,97] which showed a close dependence between the conductivity and the strength of the S···S interactions between neighbouring TTF cores which can be tuned by changing the radii of the metallic centers. This series of semiconductive MOFs with tetrathiafulvalene tetrabenzoate (TTFTB) ligands show moderate porosities with BET values around 600 $m^2 \cdot g^{-1}$, and rather moderate conductivities (**Figure 3**). Dincă also accessed a different MOF topology using lanthanides as metal ions, but did not increase conductivity values.[98]

The synthesis of new conductive TTF-based MOFs using crystal engineering is key to deliver the expected properties. In order to get good charge carrier mobilities and conductivity values, the relative orientation and the distance between the aromatic groups of the linkers has to be within certain limits for good alignment and sufficient orbital overlapping between the adjacent ligands. On paper, this could be achieved through the restrictions imposed by choosing the appropriate secondary building units (SBUs) through coordination chemistry. However, recent works by Zhou[99] and Dincă[100] point to the fact that inter-linker π-π interactions might be dominant over the formation of common inorganic SBUs in determining the final packing of the solid. As a result, metallic and superconductive behaviours, reminiscent of TTF organic salts, have not been yet reported in TTF-based MOFs, in spite of their potential to surpass those of 2D π-conjugated MOFs (see below).

Other than TTF, another case in which close π-π interactions between ligands can induce high charge carrier mobilities, is the In(III)-isophthalate based MOF prepared by Panda *et al.*[101] The presence of the π-π stacking arrangement among the phenyl rings of the ligands facilitates the high charge carrier mobility (μ = $4.6 \cdot 10^{-3}$ $cm^2 \cdot V^{-1} \cdot s^{-1}$ at V_G = -40 V) displayed by a field-effect transistor (FET) fabricated with this 2D MOF, the first realization of a FET-MOF ever reported. Another example of through space conductivity is NNU-27, a 3D MOF based on ZnII and 4,4'-(anthracene-9,10-diylbis(ethyne-2,1-diyl))dibenzoic acid ligands. The π–π stacking of the anthracene cores provide a conjugated pathway for charge carriers (σ = $1.3 \cdot 10^{-3}$ $S \cdot cm^{-1}$).[102] The addition of the same anthracene core to MOF-74 also provided through space conductivity to a series of MOFs with different metals.[103] Similar charge transport paths occur for $[Zn_2(BPPTzTz)_2(tdc)_2]^n$, (BPPTzTz = 2,5-bis(4-(pyridine-4-yl)phenyl)thiazolo[5,4-d]thiazole), a mixed-valence frameworks in which electrons travel through the cofacial thiazolo[5,4-d]thiazole units.[104] Yamashita and co-workers also presented the 2D MOF $[Cd(NDI\text{-}py)(OH_2)_4](NO_3)_{1.3\pm0.1} \cdot nDMA$, that yields a conductivity in the order of 10^{-3} $S \cdot cm^{-1}$ thanks to through space conduction via the face-to-face helical π-stacked columns of NDI cores.[105] Dincă reported a different case of charge transport through space with the MOF ZnNDI (NDI = naphthalene diimide). The redox active ligand NDI can undergo a reversible reduction into a radical form, which creates a conductive pathway for charge carriers along the stacked naphthalene moieties.[106] The measured conductivity of the fully reduced framework was not very high (σ = $2 \cdot 10^{-7}$ $S \cdot cm^{-1}$), but this is the first example of a 3D MOF in which conductivity can be reversibly modulated with a redox reaction. **2.2.2. Through-bond conductivity**

For the through-bond conductivity formalism, the charge transport happens via metal nodes and linkers and thus requires a certain degree of covalency in the bonding interactions between conjugated organic ligands and metal ions that contain loosely bound electrons. Also, both orbital symmetry and energy overlap between them are needed to promote good charge transport and higher conductivity values. When this overlap is poor, we can have systems based on localized states that still exhibit electrical conductivity due hopping mechanism.[107] Vital to such a mechanism is the need for the redox centers to have similar or the same reduction potentials and individual immobilized units to be close enough for efficient hopping. Otherwise, an entire molecular component can act as an insulating block to electronic communication across the material. This is the case for the 2D honeycomb-like CP $[\{Rh_2(acam)_4\}_3(\mu_3\text{-}Cl)_2] \cdot 4H_2O$ (acam = acetamide) based on mixed valent $[Rh_2(acam)_4]$ units, which displayed a conductivity of $2 \cdot 10^{-7}$ $S \cdot cm^{-1}$.[108] A 3D diamond-like network built with the same $[Rh_2(acam)_4]$ dimers but connected via a μ_4-I bridges instead of μ_3-Cl, displayed much higher conductivity (σ = $1.4 \cdot 10^{-3}$ $S \cdot cm^{-1}$). Electron paramagnetic resonance (EPR) results indicated that electrons hop over the Rh_2 units with a low activation barrier. Dehydration breaks the symmetry, thus hindering electron delocalization for a drop in conductivity of 6 orders of magnitude. Another example of conductive CPs based on mixed valency is $[Cu_2Br(IN)_2]_n$ (IN = isonicotinato), a 2D CP formed by pairs of $Cu^{I/II}$ ions bridged by two IN ligands and a bromide anion and a conductivity of $1.2 \cdot 10^{-5}$ $S \cdot cm^{-1}$.[109]

Entering the MOF category, we find Fe^{II}-Fe^{III} and Ru^{II}-Ru^{III} Prussian blue analogues (PBAs) prepared by Long and collaborators in 2009.[110] PBAs are monoclinic, cubic, or rhombohedral frameworks of cyano-bridged transition metal ions with or withouth alkali counterions.[111] In the case of highly symmetrical cubic networks $Fe_4[Ru(CN)_6]_3{\cdot}18H_2O$ and $K_{1.2}Ru_{3.6}[Ru(CN)_6]_3{\cdot}16H_2O$,[110] hopping between Ru or Fe sites is quite favourable for an overall electric conductivity ranging from $5.7{\cdot}10^{-3}$ $S{\cdot}cm^{-1}$ (Ru) to $5.6{\cdot}10^{-5}$ $S{\cdot}cm^{-1}$ (Fe). Furthermore, they showed to be microporous with BET surface areas of 325 (Ru) and 550 (Fe) $m^2{\cdot}g^{-1}$. The mixed valence conductivity also opened the door up for modulable conductivity in systems with metal ions susceptible to easy oxidation such as iron triazolate, tetrazolate and pyrazolate MOFs. Four-probe measurements of a pressed pellet of polycrystalline $Fe^{II}(C_2N_3H_2)_2$ yielded a conductivity value of $0.77{\cdot}10^{-4}$ $S{\cdot}cm^{-1}$.[112] After exposure to I_2, the conductivity value slightly increased to $1{\cdot}10^{-3}$ $S{\cdot}cm^{-1}$ due to Fe^{II} being oxidized to Fe^{III} for overall mixed valence conductivity. The effect was much pronounced in $[Fe(tri)_2(BF_4)_x]$ (tri = 1,2,3-triazolate) that increased 8 orders of magnitude in conductivity after exposure to O_2 (**Figure 4**).[113] Dincă and collaborators observed a similar change for $Fe_2(BDT)_3$ [H_2BDT = 5,5'-(1,4-phenylene)bis(1H-tetrazole)] with air exposure over 5 orders of magnitude and exceeding 1 $S{\cdot}cm^{-1}$, the highest conductivity so far for a 3D MOF.[114] Moreover, depending on the exposure time the Fe^{II} to Fe^{III} oxidation could be modulated along with conductivity to reach a maximum after 30 days. Long and collaborators achieved a similar redox modulated conductivity by controlling the chemical reduction of $Fe_2(BDP)_3$ (BDP = 1,4-benzenedipyrazolate) and reached a maximum conductivity of $2.5{\cdot}10^{-2}$ $S{\cdot}cm^{-1}$.[115] Hupp and co-workers also turned the insulating undoped NU-1000 MOF conductive via electrochemical oxidation of part of the tetra-phenylpyrene linkers. Then the redox hoping charge transport was analysed for two different crystal orientations, parallel and perpendicular to the pore channels, revealing a highly anisotropic conduction in this MOF.[116]

The hopping charge transport mechanism between redox metal centers is also present in metal tetracarboxylate porphyrin MOFs and CPs.[117] Morris and collaborators prepared micrometric thin films of CoPIZA onto fluorine-doped tin oxide (FTO) via solvothermal synthesis containing [5,10,15,20-(4-carboxyphenyl) porphyrin]Co(III) (CoTCPP) struts bound by linear trinuclear Co^{II}-carboxylate clusters to form a porous network with large channels.[118] The bonds in the cobalt clusters are carboxylate in nature which are known to be insulating. Therefore, it is unlikely that sufficient HOMO–LUMO overlap exists between the two molecular components to justify a band structure. Hence, CoPIZA is proposed to be a 3D network of individual redox centers. The measured conductivity, determined by the reciprocal of the area and thickness corrected low frequency intercept of the Nyquist plot, was $3.62{\cdot}10^{-8}$ $S{\cdot}cm^{-1}$, this places the system in the range of wide band gap semiconductors. Given the almost insulating behaviour of CoPIZA/FTO, charge transfer is likely to occur via a redox hopping mechanism as proven by electrochemical and spectroelectrochemical analysis.

Regarding the role played by the ligands, as in the case of the metal nodes, CPs with mixed valent aromatic ligands usually record high conductivities like the anilate-based MOFs $(NBu_4)_2Fe_2(dhbq)_3$ (dhbq = 2,5-dioxidobenzoquinone; $\sigma = 1{\cdot}10^{-2}$ $S{\cdot}cm^{-1}$)[119] and $(Me_2NH_2)_2[Fe_2(Cl_2An)_3]{\cdot}2H_2O{\cdot}6DMF$ (An = anilate; $\sigma = 1.4{\cdot}10^{-2}$ $S{\cdot}cm^{-1}$),[120] which are much more conductive that their non-redox active oxalate analogues.[121] Furthermore, even when the intervalence charge transfer (IVCT) occurs between metal centers instead, like in $[(H_3O)(H_2O)(phenazine)_3][Fe^{II}Fe^{III}(Cl_2An)_3]$[122] and [tris(amino)-guanidinium]$[Fe^{II}Fe^{III}(ClCNAn)_3]$,[123] anilate ligands yield MOFs with higher conductivities due to the much lower electron hopping barrier in the anilate complexes with respect to oxalates.[123] These materials also highlight the interplay between the mixed valency required for high conductivity and the presence of unpaired electrons that favours high temperature magnetic ordering. This conflincting relationship has been shown in these semiquinoid frameworks with post-synthetic redox reactions. Systems with mixed valent ligands such as $(NBu_4)_2Fe_2(dhbq)_3$ and $(Me_2NH_2)_2[Fe_2(ClAn)_3]$ have relatively high conductivities, but low magnetic ordering temperatures.[119,120] However, post-synthetic chemical reduction of a part or all the ligands in these frameworks to their fully reduced radical forms ($dhbq^{3-\bullet}$ and $Cl_2An^{3-\bullet}$), yields compounds with higher magnetic ordering temperatures and lower conductivities. Curiously, the 2D Mn^{II} benzoquinoid framework $(Me_4N)_2[Mn_2(Cl_2An)_3]{\cdot}3.2Et_2O$ shows the opposite behaviour with regards to electrical conductivity. Chemical reduction to its radical form $Na_3(Me_4N)_2[Mn_2(Cl_2An^{3-\bullet})_3]{\cdot}3.9THF$, provokes a magnetic transition from paramagnet to permanent magnet with a characteristic temperature of $T_c = 41$ K, but at the same time the room temperature conductivity increases by more than 5 orders of mangnitude.[124] As mentioned in section 2.1.2, redox modulation of the electrical conductivity has also been reported for TTF-based MOFs. Zuo and collaborators prepared $\{[Fe(dca)_2][TTF(py)_4]0.5{\cdot}0.5CH_2Cl_2]\}_n$ and $\{[Fe(dca)][TTF\text{-}(py)_4]{\cdot}ClO_4{\cdot}CH_2Cl_2{\cdot}2CH_3OH]\}_n$ (dca = dicyanamide; TTF-$(py)_4$ = 4-pyridyl)tetrathiafulvalene). The fist is an interpenetrated 3D network, whilst the second is a MOF formed by $\{Fe[TTF(py)_4]\}_n$ undulating layers joined by dca ligands (**Figure 11a**).[73] Oxidation of the TTF-$(py)_4$ linkers using I_2 increased the conductivity in both compounds by 2-3 orders of magnitude, probably thanks

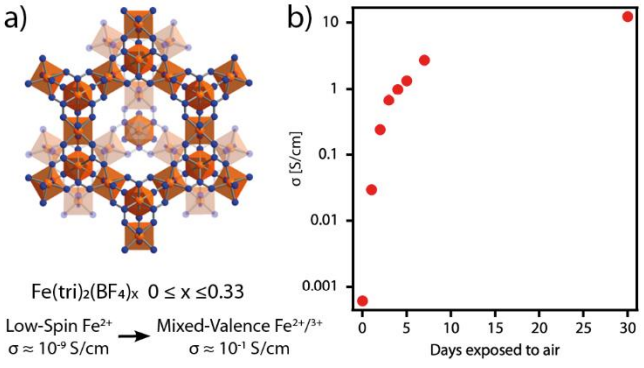

Figure 4. Modulable conductivity in a $Fe(tri)_2(BF_4)_x$ MOF (a) that increases conductivity with Fe^{II} oxidation to Fe^{III} in atmospheric conditions (b). Reproduced from ref. 113 with permission from American Chemical Society, copyright 2018.

to IVCT between the oxidized $TTF^{\cdot+}$ radical units. Interestingly, the second compound maintained SCO bistability after oxidation (**Figure 11b**, see section 3.2.).[73] Furthermore, IVCT is not unique to the through-bond mechanism, as it has also been observed to occur through-space between cofacial thiazolo-[5,4-d]thiazole units in Zn^{II} MOFs.[104] Additionally, the use of aromatic ligands and transition metal ions can result in a strong hybridization of the π-d orbitals which facilitates charge transport and favours high conductivity. For example, this was the case for the layered CP $CrCl_2(pz)_2$ (pz: pyrazine), which showed a conductivity of $3.2 \cdot 10^{-2}$ $S \cdot cm^{-1}$ through thermally activated hopping mechanism involving both pz π and Cr^{III} 3d orbitals.[125]

The interplay between conductivity (i.e. electronic structure) and structure (i.e. geometry) makes difficult to extrapolate conductivity relationships among CP series. The most important factors governing conductivity are the number of charge carriers and its mobility. In a naive manner, more polarizable atoms (lower electronegativity, better orbital overlap) should render higher conductivities. The polarizability advantage has been observed for CPs and MOFs alike, with ligands that coordinate metal centers through S-donor atoms usually reaching higher conductivity values than their O and N equivalents. Good examples of this are 2D CPs like Cu-HT (HT: 4-hydroxythiophenol), with one of the highest conductivity values for a CP (σ = 120 $S \cdot cm^{-1}$),[126] and the metal-organic graphene analogue (MOG) family (see below). The relative importance of linkers with polarizable bridging atoms and loosely bound charge carriers was analyzed by Dincă and collaborators with a series of MOF-74 type materials.[127] Replacement of Mn^{II} by Fe^{II} in Fe_2(DSBDC) (MOF-74, $DOBDC^{4-}$ = 2,5-dihydroxybenzene-1,4-dicarboxylate) yielded a million-fold conductivity enhancement. Whilst varying the bridging atom of the DEBDC ligand (E = O or S) only changed the bulk electrical conductivity by around one order of magnitude, $3.9 \cdot 10^{-6}$ $S \cdot cm^{-1}$ for Fe_2(DSBDC) versus and $3.2 \cdot 10^{-7}$ $S \cdot cm^{-1}$ for Fe_2(DOBDC). Moreover, these values are still ~6 orders of magnitude higher than those of the Mn^{2+} analogues, Mn_2(DEBDC). Because the metals are of the same formal oxidation state, the increase in conductivity was attributed to the loosely bound Fe^{2+} β-spin electron. The addition of a single electron per metal ion (i.e., substitution of d^5 Mn^{2+} for d^6 Fe^{2+}) had a much more pronounced positive effect on conductivity than changing the bridging atom from O to S, indicating that the polarizability and electronic configuration of the metal ions plays the most important role in charge conduction in this class of materials.2.2.3. Metal-organic graphene analogues: highly conjugated 2D MOFs and CPs

Amongst the conductive MOFs available, the most prolific class in terms of the number of reports, conductivity and charge carrier mobility values to date are MOGs, also referred to with the more generic term 2D π-conjugated MOFs.[128] Thus far, they are the most promising candidates for integration into electronic devices. These materials are formed by neutral 2D planar layers composed by divalent metal ions linked to benzene or triphenylene ligands with S, N, or O as bridging atoms. The layered structure results strong in-plane charge delocalization and extended π-conjugation along the metal-organic sheets. The term MOG was originally coined by Dincă and collaborators in the communication that reported the synthesis of $Ni_3(HITP)_2$ (HITP: 2,3,6,7,10,11-hexaiminotriphenylene) due to its low bandgap and good electrical conductivity enabled by full charge delocalization in the 2D plane.[129] Depending on the choice of aromatic backbone (benzene, coronene, triphenylene or truxene) and ortho-substituted hetero atoms (O, N, S or Se) of the ligand, and divalent metal ion (Fe^{II}, Co^{II}, Ni^{II}, Cu^{II}, Pd^{II} or Pt^{II}), the final MOG can have hexagonal honeycomb or Kagome in-plane lattices. Likewise, the stacking of the 2D layers can be eclipsed (AA), slipped-parallel (AB) or staggered (AA^{-1}). In general, the crystallinity of MOGs is somewhat poor due to the fast assembly kinetics caused by strong interlinker π-π interactions. Therefore, it has been extremely difficult to obtain single crystals that are large enough for single crystal X-ray diffraction (SCXRD), except for one case.[130] Thus, most of the reported structures are based on powder X-ray diffraction (PXRD) analysis of microcrystalline powders coupled with structural simulations, density functional theory (DFT) calculations, high resolution transmission electron microscopy (HRTEM) or/and X-ray absorption fine structure (EXAFS) analysis. From a structural point of view, this has made it difficult to obtain a definitive structural arrangement in some reports, especially to distinguish between out-of-plane dispositions which can be very close energetically. **Figure 5** shows the variety of structural arrangements of this family of materials.

Regarding benzene linkers (**Figure 5a-b**), the honeycomb assembly with hexagonal pores is the most common in-plane framework disposition for ligands benzenehexathiol (BHT), hexaiminobenzene (HIB), hexahydroxybenzene (HHB) and finally 1,3,5-triaminobenzene-2,4,6-trithiol, referred to as bis(iminothiolato) (IT) or bis-(aminothiolato) (AT) depending on the oxidation state of the bridging N group. However, there are a few notable exceptions, one is the $[Cu_3(C_6S_6)]_n$ or Cu-BHT Kagome network originally reported by Xu, Zhu and collaborators.[131] Its fully filled honeycomb structure does not generate pore openings so Cu-BHT is non-porous and therefore a CP. We encounter the same situation with its selenium derivate, Cu-BHS (BHS = benzenehexaselenolate) which presents the same in-plane arrangement.[132] Another exception is the recently reported $[Ag_5(C_6S_6)]_n$ or Ag-BHT, a lamellar CP with fully filled topology.[133] The reported structure has alternatively stacked 2D Ag-S networks and layers composed of 1D metal-dithiolene polymer with octahedral and square planar Ag^{I} ions. Vaid and co-workers also published a CP semiconductor with Pb^{II} and BHT. In this case, there is a 3D connectivity in between consecutive layers of Pb^{II} ions and BHT ligands, in a similar structure to that of PbS.[134] The rest of compounds known to date with benzene linkers have a hexagonal honeycomb lattices and include Ni-BHT,[135] Co-BHT,[136] Pd-BHT,[137] Pt-BHT,[138] Ni-IT,[139] Ni-AT,[140] Ni-HIB,[141,142] Cu-HIB,[141,142] Co-HIB[141,143] and Co-HHB,[144] all with a general formula of $[M_3(C_6X_6)_2]_n$ where M = Ni, Co, Cu, Pd or Pt and X = Se, S, NH, NH_2 or O.

As mentioned above, it is difficult to distinguish between interlayer stackings in MOGs. For the Cu-BHT Kagome network, the stacking configuration was initially reported as an undistinguishable mixture of AA and AB patterns,[131] but another PRXD analysis of a sample with improved crystallinity showed that the eclipsed packing is a better fit to the data.[145] Interestingly, of the benzene hexagonal honeycomb MOGs, only Co-HIB[143] shows an eclipsed packing stacking. Ni-BHT[135] and NiAT[140] stack in a staggered (AA^{-1}) disposition, whilst Pt-BHT,[138] Ni-HIB,[142] Cu-HIB[142] and Co-HHB[144] have slipped-parallel interlayer arrangement and Co-BHT disposition has not been reported. The other benzene-based MOG with a Kagome lattice, Cu-BHS, was better fitted to a slipping AA' configuration.[132]

The structural variety of benzene MOGs is also present in their triphenylene extended equivalents (**Figure 5c**). These ligands with four aromatic rings are 2,3,6,7,10,11-hexahydroxytriphenylene (HHTP), HITP, 2,3,6,7,10,11-hexathiotriphenylene (HTTP) and 2,3,6,7,10,11-triphenylenehexaselenol (TPHS). All of them yield in-plane hexagonal honeycomb lattices with Fe^{II}, Co^{II}, Ni^{II}, Cu^{II} and Pt^{II} as metal centres. Concerning their out-of-plane stacking, the first 2D frameworks published as MOGs were Dincă's $Ni_3(HITP)_2$[129] and $Cu_3(HITP)_2$,[146] which were both originally reported as having slipped-parallel disposition, as well as the THTA-Co MOG built with mixed HITP and HTTP ligands.[147] On the other hand, $Co_3(TPHS)_2$,[148] $Co_3(HTTP)_2$,[149] $Ni_3(HTTP)_2$[150] and $Cu_3(HTTP)_2$[151] layers are eclipsed and in the case of $Pt_3(HTTP)_2$ they are staggered.[152] Additionally, $Ni_3(HITP)_2$ was latter clarified as having a eclipsed or near-eclipsed staking as well thanks to a single crystal study.[153] Sticking with materials formed by the HTTP ligand, we can find a rare example of a 3D MOFs prepared with Pb^{II} metal ions: Pb-HTTP.[154] This 3D gyroidal net features a formula $[Pb_3OH_{0.5}(HTT)]^{1.5-}$ in which trigonal $Pb_3(\mu_3\text{-}O)$ cores are bonded to tritopic HTTP linkers, generating a three-connected network of the gyroid topology (srs net) as

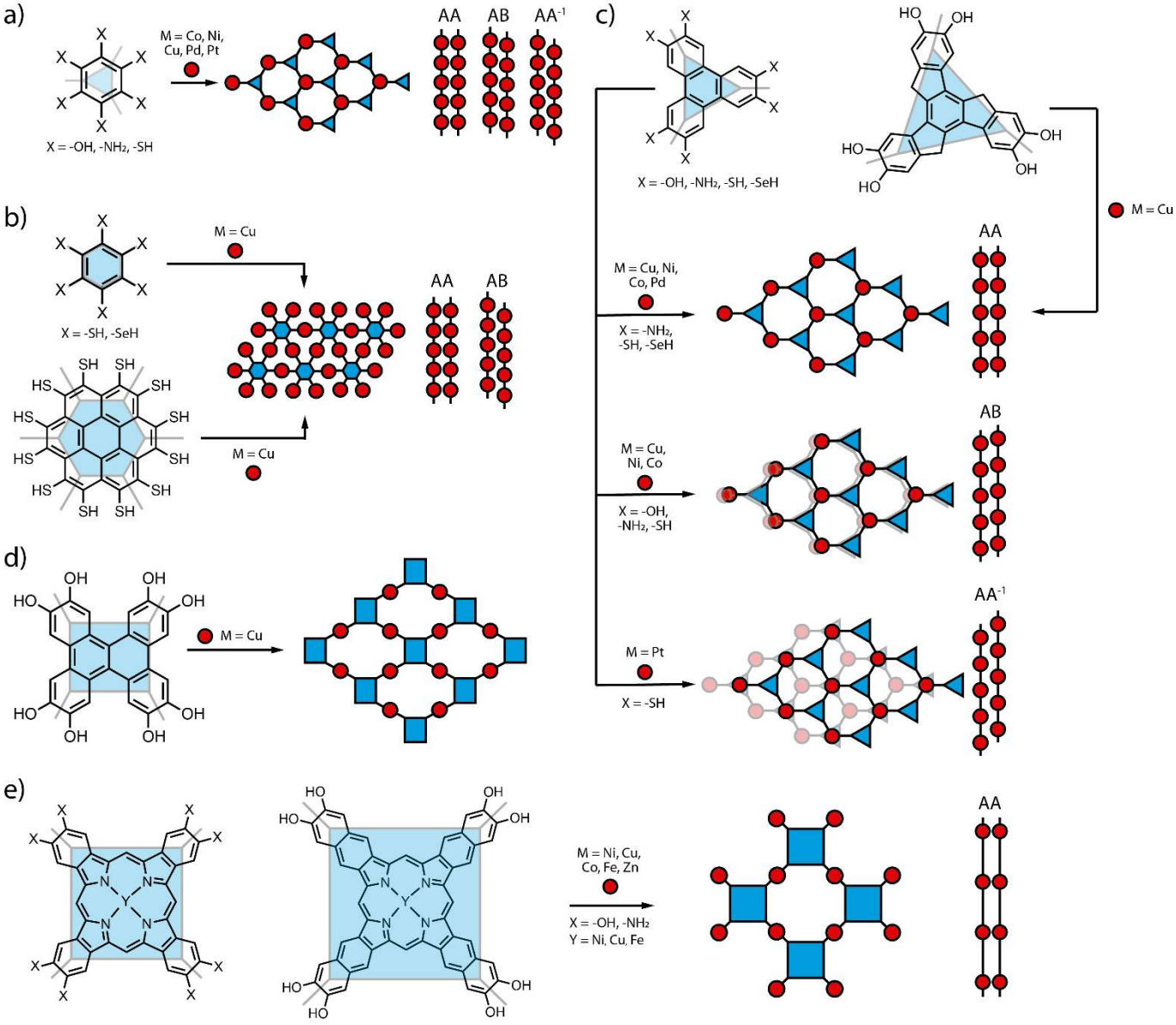

Figure 5. Different in-plane lattices and packing of 2D π-conjugated MOFs based on core of a) benzene, b) benzene and coronene, c) triphenylene and truxene, d) D_2 symmetric catechol and e) phthalocyanine and naphtalocyanine ligands with hydroxi, amine, thiol or selenol binding groups.

determined by SCXRD. Even though this material is semiconducting (σ = 1.1·10^{-6} S·cm^{-1}), it cannot be considered a MOG owing to its 3D topology and large bandgap (1.7 eV).

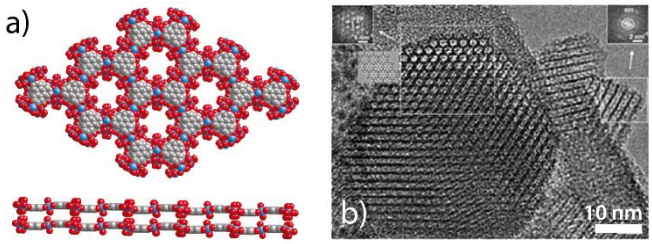

Figure 6. a) Crystal structure of Co-CAT-1 along the *c* axis. b) HR-TEM image of nanocrystals of the isostructural Ni-CAT-1. Reproduced from ref. 130 with permission from American Chemical Society, copyright 2012.

Thus far, all the above mentioned MOGs are composed by divalent metal ions 4-coordinated in a square planar geometry. Yet, there are a few cases where metal centers have octahedral geometries with triphenylene linkers occupying the equatorial positions and axial monodentate ligands occupying the axial ones. Focusing on MOGs prepared with the HHTP ligand, the first 2D π-conjugated MOFs ever reported are the M-CAT-1 series.[130] A 2012 paper by Yaghi and collaborators featured three MOFs Co-CAT-1, Ni-CAT-1 and Cu-CAT-1. Co-CAT-1 and Ni-CAT-1 have the same structure which consists of octahedral Co^{II} and Ni^{II} ions coordinated to HHTP ligands and H_2O molecules to form two different kinds of layers, one formed by an extended $Co_3(HHTP)_2(H_2O)_6$ network with hexagonal pores and the other by discrete $Co_3(HHTP)(H_2O)_{12}$ units (**Figure 6**). The two types of layers are alternatively stacked in the out-of-plane directions in an eclipsed fashion with the HHTP molecules in each layer rotated 60° with respect to each other. Also, the two axial water ligands of these discrete complexes are hydrogen bonded to oxygen atoms of the HHTP in the neighbouring layers, which causes the hexagonal layers to be slightly corrugated. All this structural information was obtained thanks to synchrotron SCXRD that allowed to solve the crystal structure of Co-CAT-1. Unfortunately, the crystal structure of Cu-CAT-1 could not be solved, but PXRD data pointed to a different structure to that of Co-CAT-1 and Ni-CAT-1. Following reports have shone light on the issue through PXRD, DFT calculations, HRTEM and structural modelling. Like other MOGs with HITP and HTTP ligands, Cu-CAT-1 or $Cu_3(HHTP)_2$ has only one type of hexagonal honeycomb layer in which Cu^{II} centers are square planar without the presence of axial H_2O molecules. Initially, there are minor discrepancies in the literature over the interlayer stacking of these layers, according to Xu's[155] and Martí-Gastaldo's[156] models they present a slipped-parallel AB disposition with similar interlayer distances (3.33 Å and 3.36 Å respectively), whilst a recent report by Behrens and collaborators describes an eclipsed stacking favoured by attractive metal–metal interactions and with a slightly lower interlayer separation (3.16 Å).[157] Nonetheless, experimental conductivity data together with DFT calculations of the electronic structure pointed towards an AB stacking as the most likely disposition.[158] Afterwards, a HRTEM study of exfoliated single crystals by Dincă's group clarified the controversy, hence consecutive Cu-CAT-1 layers are displaced in an undulating fashion which creates a kind of zig-zag pore channel.[153]

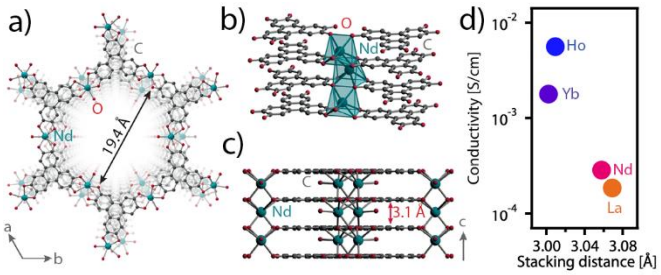

Figure 7. The 3D connected LnHHTP MOFs. a) View along the c axis of the crystal structure of NdHHTP. Side views showing the interlayer distance (b) and the heptacoordination of the Nd^{III} ions (c). d) Electrical conductivity of the LnHHTP plotted as a function of their interlayer distances. Adapted from ref. 159 with permission from Springer Nature, copyright 2020.

Another special type of MOF built with HHTP was just reported by Dincă and collaborators using lanthanide ions.[159] Hence, LnHHTP (Ln = La^{III}, Nd^{III}, Ho^{III}, Yb^{III}) have a general formula of $Ln_{1+x}HHTP(H_2O)_n$ (x = 0-0.2) and crystallize in the same hexagonal honeycomb in-plane arrangement as triphenylene based MOGs (**Figure 7a**). However, in this case there is out-of-plane connectivity through the Ln ions that lie in-between the HHTP layers and are coordinated to six O atoms of the ligands and one additional water or hydroxide molecule (**Figure 7b-c**). Therefore, making LnHHTP MOFs 3D systems. Concerning their properties, they present similar porosity to triphenylene based MOGs with BET values between 200 and 510 m^2·g^{-1}. However, their charge transport characteristics are somewhat unique. DFT calculations indicate that a strongly anisotropic metal-like transport perpendicular to the Ln-HHTP layers and a semiconductive behaviour along them. Although the conductivity measurements were performed using pellets made form polycrystalline materials, the authors related the conductivity values of the different LnHHTP MOFs to their interlayer distances. Conductivity values up to two orders of magnitude higher were obtained for the materials with a shorter interlayer HHTP-to-HHTP distance (**Figure 7d**). Thus, in this case the charge carriers would travel perpendicular to the layers in a through space regime. In contrast with 2D MOG systems, for which charge transport occurs more favourably in-plane as indicated through comparison of horizontal and vertical devices of Cu-CAT-1 oriented films.[160]

Finally, there are a few special MOG systems with mixed or chemically modified ligands. Kitagawa, Otake and co-workers published a dual-ligand MOG, $Cu_3(HHTP)(THQ)$ (THQ = tetrahydroxy-1,4-quinone) that combines triphenylene and benzene based linkers with X = O.[161] Here, a Cu^{II} ion is coordinated to one HHTP and one THQ. In order to balance the different affinities of both ligands and obtain the dual-ligand MOG, a $Cu(en)_2$ (en = ethylenediamine) complex was used as precursor instead of a Cu^{II} salt like in the rest of Cu-based MOGs. $Cu_3(HHTP)(THQ)$ crystallizes in the same hexagonal in-plane arrangement as its triphenylene-based counterparts and the layers stack in an AB slipped-parallel disposition according to PXRD and HRTEM analysis. In the other case, Ruoff, Yoo and

collaborators prepared a macrocycle derivative of $Ni_3(HITP)_2$. NiTAA (TTA = tetraaza[14]annulene) was prepared via an in situ polycondensation reaction of HITP with 1,1,3,3-tetramethoxypropane and a Ni^{II} salt to form a 2D hexagonal honeycomb network with imine bonds in the coordination sphere of Ni^{II}. The out-of-plane disposition of layer fits better with a slipped-parallel stacking mode.[162]

The structural differences commented above, give rise to acute differences in the porosity of MOGs. They are all in the microporous range (pore apertures from 0.2 to 20 nm), but the smaller pores of MOGs with benzene linkers logically yield lower values. For instance, Ni-HIB, Cu-HIB and Co-HHB have all AB interlayer stackings and show BET values up to 4-5 times lower (152, 114 and 143 $m^2 \cdot g^{-1}$ respectively)[140,144] than the equivalent triphenylene MOGs. Meanwhile, Co-HIB with an eclipsed (AA) stacking gives out a slightly higher value (BET = 240 $m^2 \cdot g^{-1}$).[143] Generally, triphenylene MOGs have larger pore apertures and naturally larger BET values. However, they do not clearly correlate well with the interlayer stackings. For instance, $Co_3(HTTP)_2$ and $Pt_3(HTTP)$ have similar BET values (370 and 329 $m^2 \cdot g^{-1}$ respectively),[149,152] but the first one has an eclipsed disposition whilst the second one is staggered. Meanwhile, dual-ligand MOG $Cu_3(HHTP)(THQ)$ has a BET surface area of 441 $m^2 \cdot g^{-1}$ with a slipped-parallel disposition.[161] It is important to highlight the disparity in the reported BET values, even for the same material, probably due to small experimental differences in synthesis and solvent removal (activation) protocols or the difficulties on controlling the crystallinity of this family of materials. For example, BET surface areas of 284,[163] 348,[158] 512[157] and 540[155] $m^2 \cdot g^{-1}$ have been calculated just for Cu-CAT-1 in different reports. In any case, the record BET surface area for a MOG is 630 $m^2 \cdot g^{-1}$ of $Ni_3(HITP)_2$[164] There are also some minor discrepancies in the pore size thorough the literature (see Table 1).

Regarding the electronic properties of the MOG family, in general conductivity values are comparable to those of typical organic conductors ($\sigma > 1 \cdot 10^{-6}$ $S \cdot cm^{-1}$). As previously mentioned, MOGs are a family of very interesting conductive materials due to their high conductivity and low modulable bandgaps. Their extended π-conjugation along the sheets and the strong p-d orbital coupling[165] results in large in-plane charge delocalization. Furthermore, both metallic nodes and organic linkers can serve as the source of charge carriers thanks to their redox active characters and unpaired electrons. The redox active character of their benzene and triphenylene ligands is well known (**Figure 8**), as well as the possibility to form stable radicals. In fact, in most MOGs the ligand gets oxidized to a

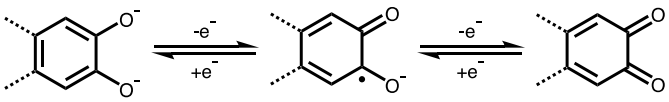

Figure 8. HHTP is a redox-active linker that can undergo reversible interconversions between catecholate, semiquinonate and quinone forms.

monoradical with a total charge of 3^- in order to achieve charge balance with the divalent metal ion. For Co-CAT-1 this was demonstrated via EPR data, which displays a near-symmetric signal at g = 2.105 characteristic of a ligand-centered monoradical. Thus, on the basis of the charge balance, the oxidation state of the deprotonated HHTP suggests that each of the three dioxolene fragments is in the semiquinone oxidation state and the Co ions are all divalent. Interestingly, for Cu-based MOGs X-ray photoelectron spectroscopy (XPS) data shows presence of Cu^I in Cu-BHT whilst for Cu-CAT-1 or $Cu_3(HHTP)_2$ the oxidation state is +2, and for $Cu_3(HITP)_2$ there is a mixture of Cu^I and Cu^{II} ions.

The specific mechanism of charge transport through 2D porous MOF networks is not yet well-understood, with some examples exhibiting band-like transport while the behaviour of others fits better with a Mott variable range hopping. Disagreements regarding their electronic structure are also present in the literature. This is likely due to the different methods used for measuring electrical conductivity and the polycrystalline nature of the samples for variable density of grain boundaries and interparticle resistance. For instance, experimentally $Ni_3(HITP)_2$ behaves as a semiconductor when a polycrystalline film in measured by the van der Pauw method.[129] But, DFT calculations predict a metallic behaviour for the bulk and a narrow bandgap semiconductive one for a single layer.[166] Further calculations by Foster *et al.* attributed the discrepancy to the influence of internal interface defects which introduce transport barriers by breaking the π-conjugation and disturbing the band structure.[167] These defects consisting on grain boundaries, strike-slip faults between grains and interlayer displacements, are behind the hopping mechanism that governs charge transport in most MOGs samples. Finally, four probe measurements of single crystals revealed a bulk metallic behaviour, whilst equivalent pellet measurements of a polycrystalline sample still yielded a semiconductive response.[153] This is a problem as most MOGs can only be prepared as polycrystalline samples for which intergrain charge hopping is a critical step hindering charge transport. Furthermore, different studies of the same MOG have reported acutely different values depending on the samples' crystallinity, crystallite morphology and the measurement conditions. For example, the conductivity of Cu-CAT-1 varies from 1.5 $S \cdot cm^{-1}$ for a single crystal four probe measurement,[153] to 10^{-4} $S \cdot cm^{-1}$ for a 10 nm thick film on interdigitated electrodes.[156] Whilst another study found a conductive 1 order of magnitude inferior (1.5 $S \cdot cm^{-1}$) for a single crystal four probe measurement.[130] This highlights another issue in conductive MOFs and CPs: how sample morphology and the technique used for measuring electrical conductivity can have an important influence on the recorded values.[168]

Generally, MOGs with benzene-backbone ligands achieve higher conductivity values than their triphenylene counterparts (see Table 1). Thus, the most conducive MOG is Cu-BHT (σ = 2500 $S \cdot cm^{-1}$), which also holds the record for the most conductive CP ever reported.[145] Meanwhile, its selenium equivalent Cu-BHS has a lower conductivity of 110 $S \cdot cm^{-1}$.[132] However, we can consider them special cases of MOG due to their Kagome lattices. The rest of benzene MOGs have slightly

lower values, the remaining systems built with the BHT linker are just one of order of magnitude less conductive like Ni-BHT (σ = 160 S·cm^{-1})[169] and Ag-BHT (σ = 250 S·cm^{-1}).[133] The HIB MOGs are a slightly less conductive, but still report high conductivity values for Cu-HIB (σ = 13 S·cm^{-1}),[142] Ni-HIB (σ = 8 S·cm^{-1})[142] and Co-HIB (σ = 1.57 S·cm^{-1}).[143] Finally, Cu-HHB shows a moderate conductivity (σ = 2.7·10^{-6} S·cm^{-1}), this highlights the effect of the orbital interaction between the Cu^{II} ions and the linkers which is weaker for HHB, likely due to the lower energy of its HOMO in comparison with that of its nitrogen derivative.[144] Despite having less data available, it is safe to say that triphenylene MOGs present a similar tendency in conductivity values with $Ni_3(HITP)_2$ and $Cu_3(HITP)_2$ being slightly more conductive than Cu-CAT-1, Co-CAT-1 and Ni-CAT-1. Another factor that influences charge transport in MOGs is interlayer separation. Thus, theoretical studies have pointed that increasing interlayer distances by inserting axial ligands coordinated to the metal ions can lead to changes in the electronic behaviour of these systems.[170] So far, there is only one example of a MOG with axially coordinated molecules and a single type of layer. $Fe_3(HTTP)_2(NH_4)_3$ presents a unique AA inclined stacking with a similar porosity to other triphenylene MOGs (BET = 526 m^2·g^{-1}). The conductivity of the system was extensively studied with time-resolved terahertz spectroscopy, and temperature-dependent 4-probe and Hall effect measurements. The Fe^{III} MOG was presented as a semiconductor (E_g = 0.2 eV) with the highest charge carrier mobility reported so far for a MOG (μ = 230 cm^2·V^{-1}·s^{-1}).[171,172]

Finally, other MOGs have been obtained using ligands with different connectivity or conjugated core than those with benzene or triphenylene based linkers. Feng and co-workers recently succeeded in the preparation of a conductive CPs using the linker 1,2,3,4,5,6,7,8,9,10,11,12-perthiolated coronene (PTC), a polycyclic aromatic hydrocarbon with six fused rings and twelve peripheral thiol groups.[173] In combination with square planar Fe^{III} ions, PTC yielded a 2D CP closely related system to the MOG family (**Figure 5b**). Fe-PTC is constructed by negatively charged planar layers that are vertically stacked in the AB disposition and have intercalated ammonium cations. The system presents a semiconductive behaviour (σ = 10 S·cm^{-1}) and ferromagnetic ordering at low temperature.[174] Besides, Zhang, Zhao and co-workers used a C3-symmetric ligand core of truxene, a popular molecule in organic electronics, functionalized with hydroxy groups. 2,3,7,8,12,13-hexahydroxyl truxene (HHTX) was combined with Cu^{II} ions to yield the same hexagonal honeycomb 2D network of MOGs with an eclipsed stacking mode between layers (**Figure 5c**). The system presented a semiconductive behaviour as well (σ = 8.4·10^{-4} S·cm^{-1}) and a relatively low porosity (BET = 120 m^2·g^{-1}) considering the pore diameter (2.2 nm).[175] Chen, Ma and collaborators used a D_2-symmetric redox-active ligand with Cu^{II} to prepare Cu-DBC (DBC = dibenzo-[g,p]chrysene-2,3,6,7,10,11,14,15-octaol). This layered MOF is not like other 2D MOFs described here, as it crystallizes into a 4-fold interpenetration of distorted diamond (dia) networks (**Figure 5d**). Nevertheless, it displays high electrical conductivity (σ = 1·10^{-2} S·cm^{-1}) and moderate porosity (BET = 271 m^2·g^{-1}).[176]

2.2.4. Other conductive 2D MOFs

Recently, a new family of conductive 2D phthalocyanine (Pc) based 2D MOFs has appeared in the literature with three different Pc ligands so far (**Figure 5e**): 2,3,9,10,16,17,23,24-octa-amino-phthalocyaninato (Pc-NH),[177] 2,3,9,10,16,17,23,24-octahydroxy-phthalocyaninato (Pc-OH)[178–182] and 3, 4, 12, 13, 21, 22, 30, 31-octahydroxy-naphthalocyaninato (NPc-OH,).[180] Various examples have been reported so far with different metals coordinated to the central cavity and to the terminal groups. All of them are composed of planar layers with square pores that stack in the eclipsed AA-stacking mode. Ni-NiPc-NH has a high conductivity (σ = 0.2 S·cm^{-1}) so far for this type of 2D materials, whist the rest are typically one or more orders of magnitude lower. It also shows the highest BET value (593 m^2·g^{-1}),[177] probably due to the neutral nature of the layers unlike the rest of systems.

Additionally, we can find other conductive 2D frameworks that contain metal ions but are constructed through organic reactions that form strong covalent bonds. Hence, they are considered a subclass of covalent organic frameworks (COFs), known as metal-covalent organic frameworks (MCOFs).[183] Most conductive MCOFs are based on metallophthalocyanines,[184,185] but one example Ni-COF is composed of Ni^{II}-Salphen units and has a structure reminiscent of MOGs with similar conductivity (σ = 1.3·10^{-2} S·cm^{-1}) and BET (362 m^2·g^{-1}) values.[186]

Table 1. Summary of conductivity and porosity data for the MOGs reported to date.

MATERIAL	CONDUCTIVITY [$S \cdot cm^{-1}$]	MEASUREMENT METHOD	ACTIVATION ENERGY [eV]	MOBILITY [$cm^2 \cdot V^{-1} \cdot s^{-1}$]	CARRIER DENSITY [cm^3]	BET [$m^2 \cdot g^{-1}$]	REF.
Co-HHB	$7.3 \cdot 10^{-8}$	Pellet, van der Pauw	0.46	-	-	143	144
Ni-HIB	8	Pellet, van der Pauw	-	-	-	152	142
Cu-HIB	13	Pellet, van der Pauw	-	-	-	114	142
Co-HIB	1.67	Pellet, 4-probe	-	-	-	240	143
Ni-IT	0.1	Pellet, van der Pauw	0.041	-	-	-	139
Ni-AT	$3 \cdot 10^{-6}$	Pellet, van der Pauw	0.113	-	-	-	140
Ni-BHT	0.15	Pellet, 2-probe	-	-	-	-	135
	160	Flake, van der Pauw	0.026	-	-	-	169
Cu-BHT	1580	Film, 4-probe	0.00206	116 (e)/99 (h)	-	-	131
	2500	Film, 4-probe	-	-	-	-	145
Pd-BHT	$2.8 \cdot 10^{-2}$	Pellet, 4-probe	-	-	-	-	137
Ag-BHT	250	Film, 4-probe	0.4	-	-	-	133
Pt-BHT/I_2	0.39	Pellet, 4-probe	-	-	-	-	138
Cu-HSB	110	Pellet, 4-probe	-	-	-	-	132
Co-CAT-1	$2.7 \cdot 10^{-6}$	Pellet, 4-probe	-	-	-	571	163
						490	130
	$3.3 \cdot 10^{-3}$	Film, van der Pauw	-	-	-	-	187
Ni-CAT-1	0.1	Pellet, 4-probe	-	-	-	473	163
						425	130
	$1.1 \cdot 10^{-3}$	Film, van der Pauw	-	-	-	-	187
Cu-CAT-1	0.2	Single crystal, 4-probe	-	-	-	-	163
	$2 \cdot 10^{-2}$	Pellet, 4-probe	-	-	-	284	130
	$2 \cdot 10^{-2}$	Film, 2-probe	0.16	-	-	540	155
	$1 \cdot 10^{-4}$	Film, 2-probe	0.24	-	-	348	156
	$4.5 \cdot 10^{-2}$	Pellet, van der Pauw	0.15	-	-	512	157
	1.5	Rod, 4-probe	-	-	-	-	153
	0.5	Flake, 2-probe	-	-	-	-	153
	0.29	Film, 4-probe	0.13				160
	0.21	Rod, 2-probe	-	-	-	475	188
$Fe_3(HHTP)_2$	$3 \cdot 10^{-3}$	Pellet, 4-probe	-	-	-	69	163
$Cu_3(HHTP)(THQ)$	$2.5 \cdot 10^{-5}$	Pellet, 2-probe	0.3			441.2	161
$Ni_3(HITP)_2$	40	Film, van der Pauw	-	-	-	630	129,164
	58.5	Pellet, van der Pauw	-	-	-	-	189
	150	Single crystal, 4-probe	-	-	-	690	153
$Cu_3(HITP)_2$	0.2	Pellet, 2-probe	-	-	-	-	146
$Co_3(HTTP)_2$	$1.4 \cdot 10^{-3}$	Pellet, van der Pauw	0.173	-	-	370	147
	$3.2 \cdot 10^{-2}$	Film, van der Pauw	0.118	-	-		
	$2.4 \cdot 10^{-9}$	Pellet, 4-probe	-	-	-	266	151
$Ni_3(HTTP)_2$	$3.6 \cdot 10^{-4}$	Pellet, 4-probe	-	-	-	166	151
$Cu_3(HTTP)_2$	$2.4 \cdot 10^{-8}$	Pellet, 4-probe	-	-	-	171	151
$Pt_3(HTTP)_2$	$2.47 \cdot 10^{-4}$	Pellet, 2-probe	-	-	-	329	152
$Co_3(TPHS)_2$	10^{-6}	Pellet, 2-probe	0.294	-	-	246	148
$Fe_3(THT)_2(NH_4)_3$	$3.4 \cdot 10^{-2}$	Film, 4-probe	0.125	220	$6.2 \cdot 10^{14}$	526	171
Fe-PTC	10	Pellet, 4-probe	0.2	-	-	-	174
Cu-HHTX	$8.4 \cdot 10^{-4}$	Pellet, 2-probe	0.21	-	-	120	175
Cu-DBC	$1 \cdot 10^{-2}$	Pellet, 2-probe	0.3	-	-	271	176

3. Magnetic bistability in MOFs and CPs

Magnetism is another fundamental electronic property of MOFs and CPs that contain open-shell metal centres with unpaired electrons. Naturally, it has received significant scientific attention over recent years,[190–199] specially cooperative magnetic phenomena such as magnetic long-range ordering and spin state switching. Spin crossover (SCO) in particular, is the property with a more extended application in electronic devices[25,29,200–205] and hence it is the main focus of this review. This phenomenon refers to the transition between high spin (HS) and low spin (LS) electronic configurations that occurs in d^4-^{7} first row transition metal ions coordinated in an octahedral geometry. The spin state is determined by the relative magnitude of the ligand field splitting (the electrostatic field acting at the central metal ion) compared to the mean spin-pairing energy. If the first is greater, electrons will pair up and completely fill the lower energy t_{2g} orbitals before populating the higher energy e_g orbitals. Hence, the metal ion adopts a diamagnetic LS configuration. If the opposite is true, the unpaired electrons yield a paramagnetic HS state (**Figure 9**). Each of the two spin states endows the material with different magnetic, optical, mechanical, electronic and structural properties.[206,207] The SCO transition between HS and LS can be induced by a variety of external inputs like temperature, light, pressure, guests and magnetic or electric fields.[208–212] Furthermore, this transition has extremely fast dynamics and can occur cooperatively across the material, thus yielding bulk hysteretic behaviours.[213] Fe^{II} is the most common metal ion to present SCO behaviour followed by Co^{II} and Fe^{III},[214–217] whilst SCO in d^4 systems, like Cr^{II}, Mn^{II} and Mn^{III}, is much less frequent.[218]

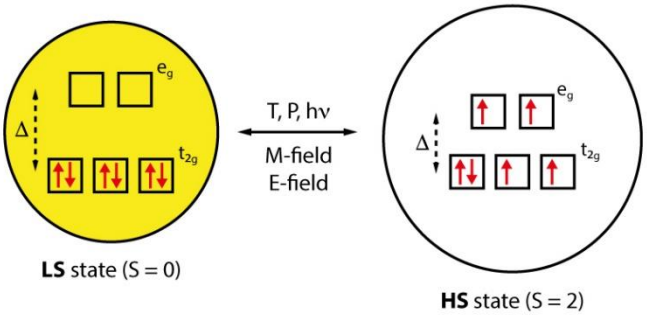

Figure 9. Scheme depicting the SCO transition between HS and LS configurations for a d^6 transition metal ion.

3.1. Fe^{II} Hofmann-type coordination polymers

The perspective of combining the physical properties of metal-ligand coordination networks (chemical tunability, porosity, processability, etc.) with SCO materials' bi-stable nature is very attractive from a device point of view. Within the wide variety of 2D and 3D SCO MOFs and CPs that have been reported, Fe^{II} Hofmann-type[219] coordination polymers (Fe^{II}-HCPs) are by far the most popular.[220] Their structure is composed by planar grid-like metal-cyanide layers interconnected by nitrogen-containing ligands (**Figure 10**). These sheets alternate octahedral Fe^{II} metal ions, responsible for the SCO behaviour, and divalent group 10 metal centres that adopt a square planar geometry. The Fe^{II} atoms are coordinated to the N of four cyanide groups and to two additional pillaring ligands. If these are bis-monodentate, the resulting structure is generally 3D, with a general formula of $[Fe^{II}(L)\{M^{II}(CN)_4\}]$ (L = Ligand, M^{II} = Ni^{II}, Pd^{II} or Pt^{II}), as a single pillaring ligand covalently bonds two adjacent layers (**Figure 10b**). On the other hand, when monodentate ligands (usually py derivatives) are used a 2D network is obtained with a general formula of $[Fe^{II}(L)_2\{M^{II}(CN)_4\}]$, although neighbouring sheets are still interconnected via π-π interactions (**Figure 10c**). 3D Fe^{II}-HCPs networks usually have permanent porosity, which can be used to influence the SCO transition through the incorporation of guests that affect the ligand field splitting of Fe^{II}.[221,222] Real, Bousseksou, Kitagawa and collaborators have extensively investigated this possibility. Thus using either invasive guests to induce redox changes in the network,[223] or softer guests that more subtly modify the coordination environment through electronic interactions with the pillaring linkers[224–235] or by blocking the rotation of their aromatic rings.[236–238] Sometimes, this can trigger the appearance of multi-step spin transitions by breaking the symmetry of the Fe^{II}-HCP network.[228,231–235] The stabilization of either the HS or the LS state can occur depending on the chemical nature, which determines the type and strength of electronic interactions, and size of the guest molecules, which delimits the expansion/contraction of the network characteristic of the SCO transition.[237,239,240] Conversely, in 2D Fe^{II}-HCPs the interdigitated arrangement of the consecutive layers does not leave any pore space for regular permanent guest sorption. Moreover, they usually present

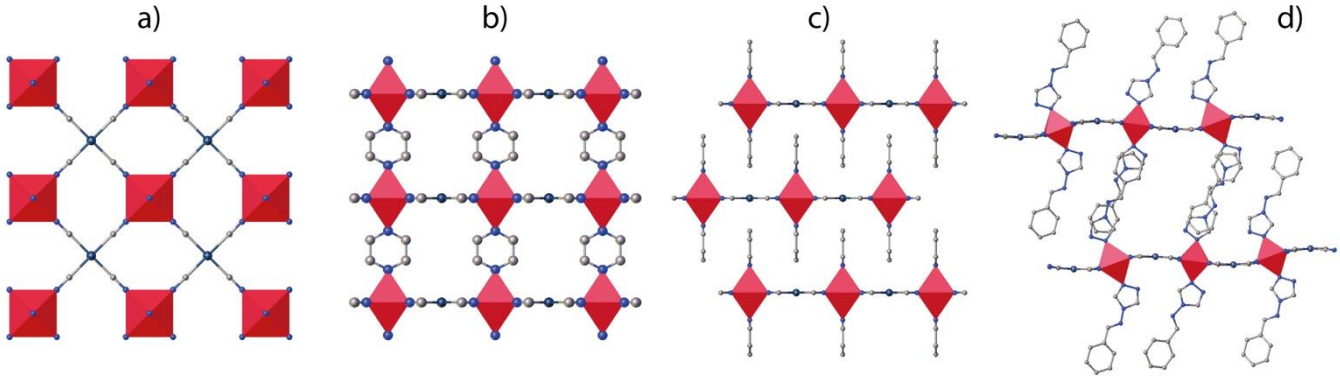

Figure 10. Structure of representative 2D and 3D SCO Fe^{II}-HCPs. a) Grid-like structure of the constituting layers of 2D and 3D Fe^{II}-HCs. Perspective showing the b) interlinking of neighbouring layers by axial linkers in 3D Fe^{II}-HCPs and the c) interdigitated structure of layered 2D Fe^{II}-HCPs. d) 3D structure of Fe^{II}-HCPs built from functionalised 1,2,4-triazoles.

lower SCO transition temperatures and narrower hysteresis loops due to a lower degree of cooperativity in-between the non-covalently bonded layers. However, a few examples prepared by Neville, Kepert and collaborators escape this tendency by using functionalised 1,2,4-triazoles as axial Fe^{II} ligands (**Figure 10d**). Hence, they report near ambient room temperatures and guest dependent SCO properties, as guest solvents interact with the free N of the triazole ring.[241–243] Additionally, some other 2D Fe^{II}-HCPs with py derivatives as pillaring linkers also present guest sorption capabilities when the number of layers is reduced below a critical number. In this sense, $[Fe^{II}(L')_2\{Pt(CN)_4\}]$ (L' = py, pyrimidine and isoquinoline) ultrathin films (<30 layers) have been proven capable to accommodate solvents in-between their layers, through an axial lattice expansion observed via synchrotron XRD.[244–246]

3.2. Electrical conductivity and SCO

The combination of SCO and electrical conductivity in a single material has been a long-desired goal for material scientists. Particularly, in the context of the use of electrical stimuli to control the SCO transition or vice versa, as electrical current would constitute a more feasible way of managing input/output signals in a SCO device setting rather than temperature or pressure.[203] Unfortunately, most SCO compounds known to date are insulating, particularly SCO CPs and MOFs. This is still a major obstacle for their integration in electronic devices.

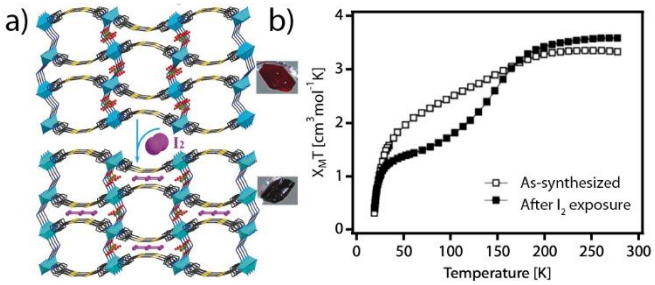

Figure 11. a) View along the c axis of as-synthesized $\{[Fe(dca)][TTF\text{-}(py)_4]\cdot ClO_4\cdot CH_2Cl_2\cdot 2CH_3OH]\}_n$ and $\{[Fe(dca)][TTF(py)_4]\cdot 0.5\ I_3\cdot ClO_4\cdot CH_2Cl_2\cdot CH_3OH\cdot C_6H_{12}\}_n$ after of I_2 exposure. Next to the structures photographs of the corresponding crystals are shown. b) Temperature dependence of the molar magnetic susceptibilities before and after of I_2 exposure. Reproduced from ref. 73 with permission from Wiley, copyright 2017.

Looking at the present state of the area, the main goal of most researchers in the SCO field has exclusively centred around the transition phenomena itself. In the meantime, the challenge of producing highly conductive SCO materials has been largely overlooked. Some efforts have been dedicated to produce materials that display SCO together with high electrical conductivity values. However, only one of the previously described strategies for infusing electrical conductivity in non-magnetic MOFs and CPs has been really explored. Following the path of molecular conductors, the strategy of including electroactive TTF moieties in the organic linkers has been attempted to induce electrical conductivity into Fe^{II}-HCPs and other SCO CPs. For Fe^{II}-HCPs, the axial organic ligand that connects the metal-cyanide layers can be chemically modified to incorporate an electroactive group. Real and collaborators used this strategy to prepare $\{Fe(ttf\text{–}adpy)_2[M(CN)_4]\}\cdot nH_2O$ (ttf–adpy = 4-tetrathiofulvalenylcarboxamidopyridine; M = Ni, Pd, Pt), a series of 2D Fe^{II}-HCPs.[247] Here, Fe^{II} centres are axially coordinated to ttf–adpy ligand, which consist of a pyridine unit bonded to a TTF core via a secondary amide. Electrochemical studies indicated that free ttf–adpy has low oxidation potential to form the radical. As result, the ttf–adpy units were neutral for all cases and the 2D Fe^{II}-HCPs displayed low cooperative SCO transitions strongly dependent on their water content.[247] As commented in section 2, Wang *et al.* prepared $\{[Fe(dca)][TTF\text{-}(py)_4]\cdot ClO_4\cdot CH_2Cl_2\cdot 2CH_3OH]\}_n$, a non-interpenetrated CP with open pore channels and octahedrally N-coordinated Fe^{II} ions that undergoes gradual and incomplete SCO in its as-synthesized form.[73] When a single crystal was exposed to a I_2 solution, $\{[Fe(dca)][TTF(py)_4]\cdot 0.5\ I_3\cdot ClO_4\cdot CH_2Cl_2\cdot CH_3OH\cdot C_6H_{12}\}_n$ was obtained, which has I_3^- anions inbetween oxidized $TTF^{\cdot+}$ radical ligands (**Figure 11a**). Surprisingly, this compound did maintain SCO transition, although it was significantly more incomplete and more gradual (**Figure 11b**).[73] These being the only published attempts at making a highly conductive SCO framework material, reinforces the idea that a lot more effort needs to be dedicated to this challenging task. Nevertheless, we can find one additional in the 1D chain CP $[Co(MQ)_2]$ (MQ = 8-mercaptoquinoline), a semiconductor ($\sigma = 1.7\cdot10^{-7}$ S·cm^{-1}) with a gradual SCO transition of the Co^{II} ions in an unusual coordination environment of N and S atoms.[248] Also, in a somewhat unique strategy, Martin and Lemaire, prepared a SCO conducting metallopolymer based on qsal type ligand covalently linked to a thiophene polymer. The electropolymerized film showed a gradual SCO transition with no thermal hysteresis but it did show hysteretic conductivity with temperature. Although the conductivity values are the highest so far for a SCO material (approximately 10-100 S·cm^{-1}), the relationship between SCO and conductivity was not clearly demonstrated.[249]

The rest of the studies of charge transport properties of SCO materials have dealt with compounds that were not specifically designed with conductivity in mind and are therefore poor conductors. Again, there is not a very extensive amount of work done concerning this type of materials, particularly SCO CPs and MOFs, as it is extremely challenging to measure current values below the detection limit, especially at low temperatures. In a recent publication, Martí-Gastaldo, Tatay and co-workers fabricated ultrathin films (thickness < 15 nm) to analyse the conductivity of 2D Fe^{II}-HCPs: $[Fe(L)_2\{Pt(CN)_4\}]$ (L = pyridine, pyrimidine, and isoquinoline).[246] Out-of-plane charge transport was then measured using liquid Eutectic Gallium Indium alloy (EGaIn) as top electrode (**Figure 12**). Analysis of thickness dependent current density measurements at room temperature (HS) yielded a low decay coefficients (β = 0.03-0.08 Å^{-1}), characteristic of a hopping regime (<0.1 Å^{-1}) and in line with other SCO ultrathin films measured in the same conditions.[250,251] Thus, in this through space hopping conduction, the axial linker L heavily influences the vertical charge transport by altering the interlayer distance, and also governs the electronic interaction with the EGaIn top contact.[246]

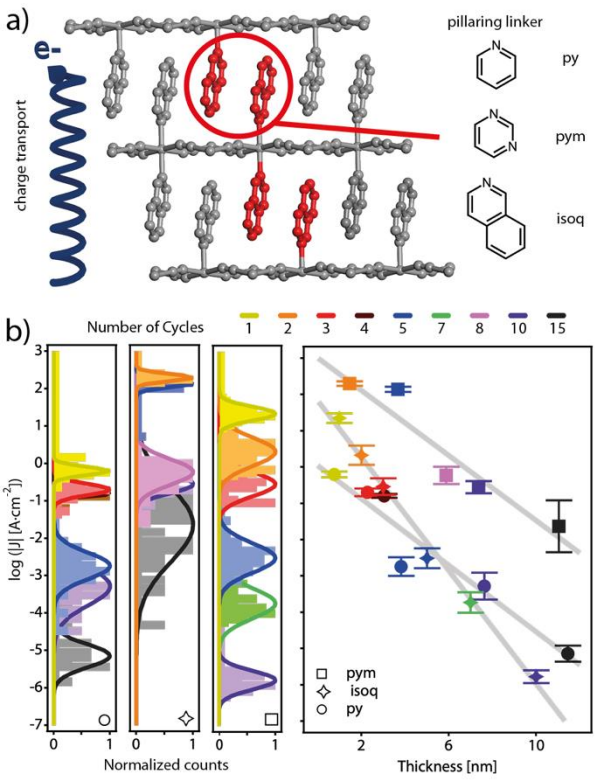

Figure 12. a) Schematic crystallographic structure of the $[Fe(L)_2\{Pt(CN)_4\}]$ (L = pillaring linker) 2D Fe^{II}-HCPs used in by Martí-Gastaldo and co-workers. b) Dependence of the logarithm of the absolute value of the current-density (log|J|) measured at 0.1 V as a function of film thickness films. Maximum number of counts for each histogram has been normalized to 1. Solid lines are Gaussian fits to the data. Error bars correspond to the Gaussian width. Straight dashed lines are a linear fit to the data. In all cases, colours indicate the number of growth cycles. Reproduced from ref. 246 with permission from American Chemical Society, copyright 2019.

Finally, the only other SCO CP whose charge transport properties have been broadly extended is $[Fe(Htrz)_2(trz)](BF_4)$ (Htrz = 1,2,4-1H-triazole), an ionic 1D CP formed by chains of Fe^{II} centres linked by triazoles[252,253] that has a hysteretic SCO transition at around room temperature.[254] Bousseksou, Salmon and co-workers performed most of the work with this material (**Figure 13**).[255–260] These different studies were performed with different set-ups (two probe contacts or interdigitated electrodes,[259,260] DC[258] or AC conductivities[255,261,257]) and using samples with slightly different crystallite sizes (0.7-5 µm x 200-300 nm high aspect ratio needles[258–260] or ~200 nm nearly spherical particles[255,261,257,258]) and large electrode gaps of several micrometres. Nonetheless, most of them yielded comparable results and pointed to the same conclusion: the HS form is less conductive than the LS state (**Figure 13b**). However, there was one sample of spherical NPs that showed the opposite trend, a more conductive HS phase. The authors ascribed this exception to small changes in the defect structure or in the particle morphology (grain boundary effects).[258] Surprisingly, the magnetic measurements on this particular sample showed similar SCO properties to the others. Precise conductivity values were only given in one publication for DC measurements on pellets of needle-like micrometric crystallites (σ_{HS} = 5·10^{-1} S·cm^{-1}; σ_{LS} = 6·10^{-4} S·cm^{-1}) and spherical nanoparticles (σ_{HS} = 9·10^{-7} S·cm^{-1}; σ_{LS} = 6·10^{-7} S·cm^{-1}).[258] Again, the difference between samples is quite remarkable, especially considering that they both displayed similar SCO properties. Increased grain boundaries are probably to blame for this disparity.

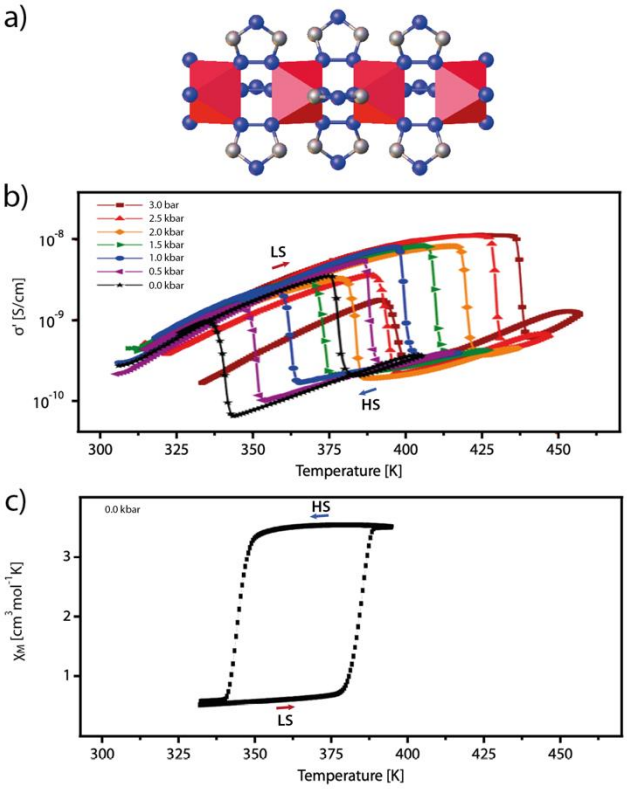

Figure 13. a) Schematic crystallographic structure of $[Fe(Htrz)_2(trz)](BF_4)$, anions have been omitted for clarity. b) Temperature dependence of the real part of the AC conductivity recorded at 10 kHz at various applied pressures. b) Temperature dependence of the molar magnetic susceptibility. Adapted from ref. 261 with permission from American Chemical Society, copyright 2017.

A different work by Dugay, Coronado and co-workers reported similar results for high aspect ratio nanorods (10 x 25 and 6 x 44 nm in size) deposited onto interdigitated electrodes with a gap of 50 nm.[262] The LS state was found to be the high-conduction state by up to 2 orders of magnitude difference and a hysteresis loop 45 K in the electrical current versus temperature plot. But, as the reproducibility of the measurements was analysed, they were found not to be reversible after only one heating/cooling cycle. Current values progressively decreased below the detection limit, presumably as more Fe^{II} centres get trapped in the HS configuration. Later, they managed to conduct a more reproducible study of 110x50 nm core-shell NPs of $[Fe(Htrz)_2(trz)](BF_4)$ with a 11 nm SiO_2 shell, which were contacted by graphene single layer electrodes with a gap of 300 nm. Results showed again a more conductive LS state.[263] Bousseksou, Salmon, Rotary and co-workers also argued that the charge transport in big particles of $[Fe(Htrz)_2(trz)](BF_4)$ occurs via polaron hopping. Hence, they associate the higher conductivity in the LS state to its higher stiffness (i.e., higher phonon frequencies), which results in higher hopping rates.[257] However, in a separate study, Dugay, Coronado and co-workers used time-resolved microwave conductivity to show that there is actually two different transport regimes in the LS state:

tunnelling through shallow traps which transits into a trap free hopping regime with increasing temperature.[264]

All the above studies of $[Fe(Htrz)_2(trz)](BF_4)$ show an opposite trend to the results reported by Prins et *al.*, which showed that the HS state has a larger conductivity than its counterpart. Nanoparticles of 11 ± 5 nm were placed between gold electrodes with a gap of either 100 nm or 1 µm, thus operating in the tunnelling regime.[265] The authors suggested that the increase in Fe-N bond lengths (0.2 Å) upon the LS to HS spin transition could lower the tunnel barrier, thus leading to an increase of the conductance. This reinforces the premise that different charge transport regimes (tunnelling versus hopping) yield a different predominant spin state in terms of electrical conductivity. Interestingly, a hysteresis loop of similar width to the magnetic curve was obtained in the conductance as a function of temperature plot. However, concerning reproducibility: out of ten samples, the conductance switch occurred in 50% of them, while just 30% displayed hysteresis and in the remaining 20% the change in conductance was (partially) irreversible.[265]

However, there is one conflicting study to this idea concerning $[Fe(Htrz)_2(trz)](BF_4)$. Torres-Cavanillas *et al.* prepared core@shell spherical NPs with a Au core (ca. 12 nm) and a $[Fe(Htrz)_2(trz)](BF_4)$ shell (4 nm).[266] Charge transport measurements were then performed in a device fabricated by depositing the NPs onto interdigitated electrodes. The device showed a sharp hysteretic transition in thermal variation of the electrical current with an on/off ratio of 1500 between a high conductance LS and a low conductance HS state. This conductance transition was explained via a percolation model. $[Fe(Htrz)_2(trz)](BF_4)$ NPs of 16 nm without the Au core were also prepared, but they were too insulating for transport measurements.[266] Again, previous measurements of small NPs (11 ± 5 nm) showed opposite results for the HS/LS conductivity change.[265]

3.3. Electrical properties of individual spin states

Regardless of achieving materials that show both SCO transition and high conductivity, gathering information on the electrical properties of each of the individual spin states is also of vital importance for device integration. However, the amount of work done in this sense is still scarce with very few studies of bulk materials, nanometric particles or films of extended CPs. The vast majority of them being materials composed of discrete molecular complexes and not framework systems that are the main scope of this review. At the present time, there is not even clear evidence to draw definitive general conclusions about which spin state is more conductive (HS or LS), due to contradicting experimental results. This is a difficult problem to tackle as most SCO materials have already low charge carrier mobilities at room temperature, so cooling them down yields negligible current values. Hence, it is extremely challenging to obtain reliable measurements in bulk samples or to fabricate viable nanometric devices. Thus far, the options have been restricted to either working with SCO systems with HS-to-LS transitions that occur at high temperatures, reducing the electrode separation or downsizing particles or film-based devices in order to operate in the tunnelling regime. But of course, modifying the charge transport mechanism from hopping to tunnelling can also influence the device resistance variation with the spin state, and so can the SCO/electrode interface. All this along with the already challenging fabrication and characterization of devices as well as reproducibility issues, add to the difficulty in elucidating the relationship between spin state and conductivity.[203,204] Most reports that observe a more conductive HS configuration are of single molecule, monolayer or few-layer junctions (tunnelling regime), while most of the papers pointing in the opposite direction are of large contact are devices or nanocrystalline samples (hopping regime). Nonetheless, there are a few exceptions to this clasification.[267–269,266,270] So far there is only one record of a single crystal measurement with the two-probe method.[271] Undoubtedly, the synthetic difficulties in producing large crystals are also an important obstacle for SCO materials along with their low charge carrier mobilities.

3.4. Electrical conductivity and valence tautomerism in PBAs

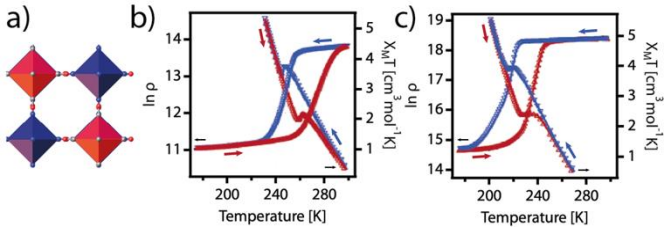

Figure 14. a) Schematic crystallographic structure of FeCo Prussian blue analogue. The vacancies at the $[Fe(CN)_6]$ site and the Na^+ atoms have been omitted for clarity. Temperature dependence of resistivity and magnetization for b) $Na_{0.5}Co^{II}_{1.25}[Fe^{III}(CN)_6]\cdot 4.8\ H_2O$ and c) $Na_{0.38}Co^{II}_{1.31}[Fe^{III}(CN)_6]\cdot 5.4\ H_2O$. Adapted from ref. 272 with permission from American Chemical Society, copyright 2004.

Valence tautomerism (VT) can be considered another type of cooperative magnetic by-stability, as it consists on the reversible interconversion between redox states of different metal ions in polynuclear coordination compounds. We find a similar case to the conductivity and SCO relationship in the conductivity dependence with VT switching that can be observed in some PBAs. As previously mentioned in section 2.2.2., PBAs are analogues of $Fe^{III}_4[Fe^{II}(CN)_6]_3\cdot nH_2O$ with a general formula of $A_xM_y[M(CN)_6]_z\cdot nH_2O$, in which A is an alkali metal ion and M are transition metal ions.[111] The octahedral coordination of the transition metal ions with cyanide anions results in cubic (**Figure 14a**), monoclinic or rhombohedral 3D networks depending on the distortion of the coordination sphere. If the metal-cyanide network is not neutral, the pores are occupied by the alkali counterions. Usually, the M coordinated with the N of the cyanide ligand presents a trivalent oxidation state in the HS configuration and the one coordinated with C presents a LS divalent oxidation state. The process in which an electron can travel in-between these metal centers can be classified as VT. FeCo PBAs are widely known to present VT, also referred to as charge-transfer-induced spin transition (CTIST),[273,274] due to the reversible transition between diamagnetic $Fe^{II\text{-}LS}$-CN-$Co^{III\text{-}LS}$ and paramagnetic $Fe^{III\text{-}LS}$-CN-$Co^{II\text{-}HS}$

configurations. [275] Similarly to SCO, the CTIST transition can be triggered by temperature or light irradiation and provokes changes in the compounds' bond lengths, magnetic, photochromic and electric properties.[276]

The first report on the dependence between electrical conductivity and VT was published by Sato *et al.* for the Fe Co PBAs $Na_{0.5}Co_{1.25}[Fe(CN)_6]\cdot 4.8H_2O$ and $Na_{0.38}Co_{1.31}[Fe(CN)_6]\cdot 5.4H_2O$.[272] These compounds show an abrupt change in conductivity at the same temperature of the magnetic phase transition between $Fe^{II\text{-}LS}$-CN-$Co^{III\text{-}LS}$ and $Fe^{III\text{-}LS}$-CN-$Co^{II\text{-}HS}$ with a similar hysteresis loop in both of them (**Figure 14**). Moreover, the conductivity phase can also be altered by applying an electric field. This behaviour has also been observed for MnFe PBAs. Thus, Molnár *et al.* observed a similar effect in a series of $Rb_xMn[Fe(CN)_6]y\cdot zH_2O$ PBAs.[277,278] Additionally electrical conductivity modulation with VT has been observed in cyanide-bridged CPs of lower dimensionality than 3D PBAs. For instance, the 1D chain $\{(Tp)Fe(CN)_3Co((R)\text{-pabn})(BF_4)\}\cdot H_2O$ (Tp = hydrotris(pyrazol-1-yl)borate; (R)-pabn = (R)-N(2),N(2')-bis(pyridine-2-ylmethyl)-1,1'-binaphtyl-2,2'-diamine) shows and evolution from insulator to semiconductor with the CTIST transition.[279]

4. Nanostructuration strategies for device fabrication

All the strategies reviewed above highlight the wide range of possibilities to produce electrically active and magnetically bi-stable CPs and MOFs. This potential for tailor-made materials has pushed industrial and academic researchers to initiate the path to integrate them in electronic devices, resulting in several reviews and roadmaps that indicate the current challenges and technological barriers.[23–25,57,58] Nevertheless, before truly considering them as components of an electronic device compatible with CMOS technology, it is necessary to understand how these materials function within the device and how they interface with it. On this order of ideas, it is first necessary to deposit and study these materials on surfaces as thin films. Materials have to be carefully processed with exquisite control over several factors that play an important role in the device performance. Ideally, film thickness, substrate coverage, homogeneity, roughness, crystallinity and crystalline orientation with respect to the substrate have to be carefully controlled to achieve a viable device. Controlling the above parameters is necessary so that the designer properties of the original bulk material are equivalent in its nanostructured form. The quality of the film can be changed drastically depending on the deposition method drastically affecting material performance. Besides, this structuration also presents a challenge for chemical and physical characterization.[27] In the following sections, we will review some of the techniques used for the deposition of CPs and MOFs as thin films.

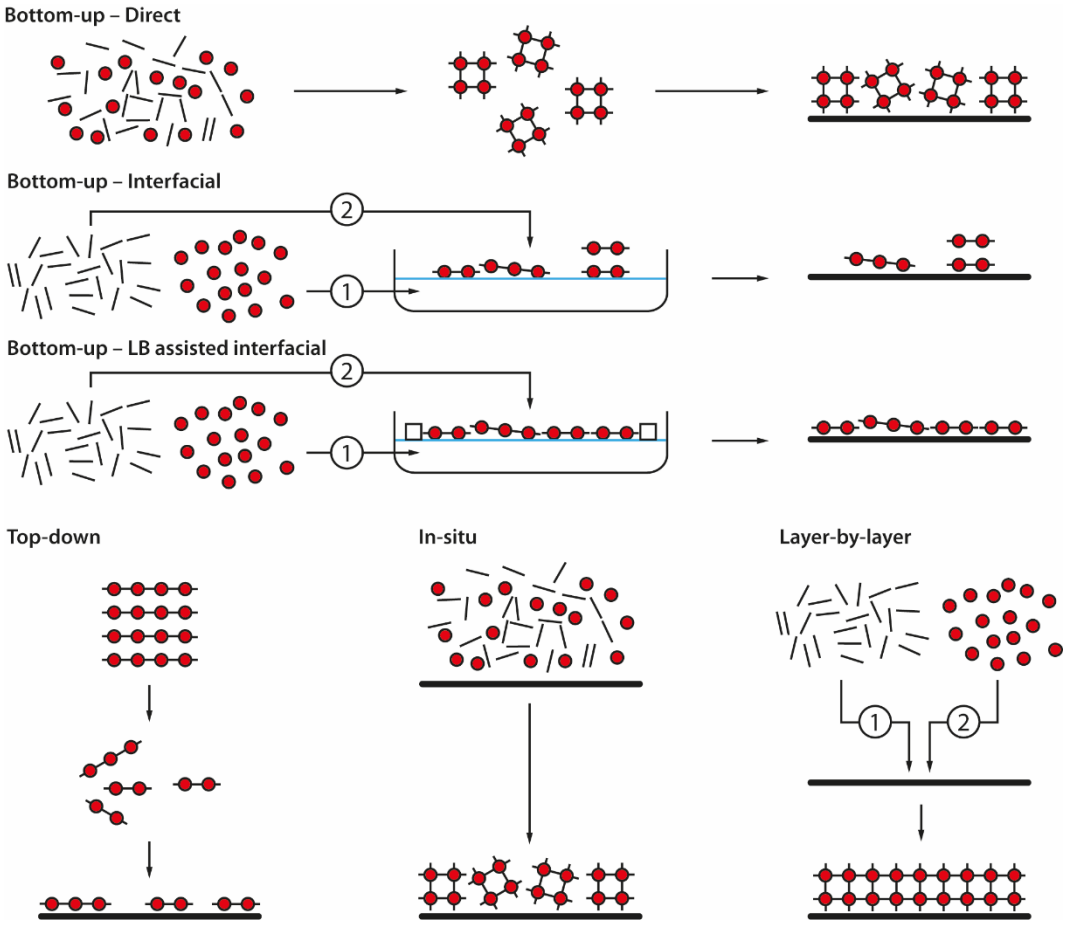

Figure 15. Schematic illustrations exemplifying the most common protocols used for the synthesis and/or transfer of MOFs and CP to solid substrates.

As shown in **Figure 15**, we will divide deposition methods depending on how the final material is formed: (i) deposition from crystals or colloids/colloidal dispersions, where materials are previously synthesized and then deposited on the surface, (ii) direct synthesis of micrometer-thick films that are generally grown by seeding methods and (iii) Layer-by-Layer (LbL) films grown by sequential deposition methods. As we will see later, some of those methods can be improved by functionalizing substrates to promote and direct the nucleation, orientation, and structure of the resulting film.

4.1 Deposition of pre-formed materials.

This type of procedure is composed of two steps. The first one involves the synthesis of the desired material in solution (bottom-up approach) or as bulk material that in turn can be physically or liquid phase delaminated (top-down approach). In the second step, the pre-formed material is deposited on the surface.

4.1.1. Bottom-up deposition

Fabrication of MOF films by this method has been used, among others, by Sanchez, Serre, and co-workers. It consists on preparing MOF particles with well-defined size and transferring them onto silicon substrates by dip-coating. They demonstrated this concept experimentally with three different MOF structures: MIL-89 $[Fe_6O_2Cl_2(BDC)_6]$,[280] MIL-101 $[Cr_3OF(BDC)_2(H_2O)_2]$[281] and ZIF-8 $[Zn(Cu_4H_5N_2)_2]$ (**Figure 16**).[282] Depending on the concentration of the particles in solution, 2-3 layers of particles were deposited at the same time. Repetition of the dip-coating process led to thicker films for good control of the thickness. However, the mechanical resistance of such films is moderate due to their poor adhesion to the substrate. The advantage of this method is that the size and crystallinity of the particles is controlled in a first step and is not limited by the preparation of the films. On the other hand, it relies on the preparation of stable colloidal dispersions and does not permit producing oriented films. These films can broadly be described as bulk crystalline powders resting on a substrate due to the high roughness of the films and their irregular micrometric thickness.

Better control on film thickness and orientation can be achieved when the formation of the material to deposit takes place at the air-liquid (AL) or liquid-liquid (LL). In this case, metal ions and organic linkers present in different phases coordinate at the interface to yield coordination crystalline nanosheets.[283] Multilayer, few or single layer nanofilms can form at the liquid–liquid or air-liquid interfaces This approach has been extensively developed specially for 2D CPs and MOFs,[27] also known as coordination nanosheets (CONASHs),[284,285] metal-organic layers (MOLs),[286]metal-organic framework nanosheets (MONs)[287] or just low dimensional MOFs (LD MOFs).[288] When films are pre-assembled at the LL interface, the procedure typically consists of carefully layering a solution of ligand in an organic solvent or a mixture of solvents onto a water solution of the metal salt, if the ligand solution is denser than water, then the metal solution is layered on top instead (**Figure 15**). For instance, Sakamoto *et al.* prepared bis(dipyrrinato)zinc(II) complex micro and nanosheets containing zinc(II) porphyrin that could be layered quantitatively onto a flat substrate (Figure 17).[289] More sophisticated versions of this method include using a pure solvent as a diffusion barrier in between the two immiscible solvents that contain the metal-organic building blocks[139,140] or spraying the top solution instead of layering it with a syringe.[290,291]

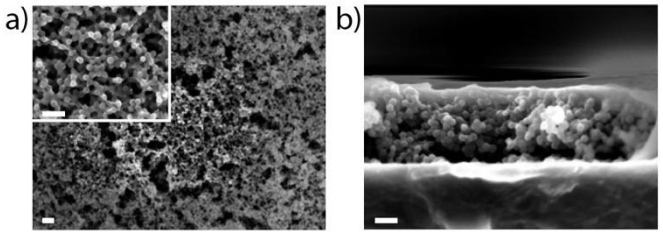

Figure 16. Field Emission SEM images of thin films prepared by dip-coating a silicon substrate on a colloidal solution of ZIF-8 NPs. a) top view and b) side view. Scale bar length is 100 nm. Reproduced from ref. 282 with permission from the Royal Society of Chemistry.

The AL interfacial synthesis is similar to the LL version, a controlled amount of a diluted solution of a volatile organic solvent containing the ligand is carefully dispersed onto the surface of an aqueous solution of a metal salt. The organic solvent quickly evaporates leaving the ligand to react with the metal ions at the AL interface forming a floating layer of the CP or MOF in question. In any case, the final step involves the transfer of the films from the liquid-liquid interface to a solid substrate. This can be done by piercing the interfacial film with a substrate going either from the organic to the water solution or vice versa, by repeating the assembly-deposition process several times, the final film thickness can be controlled. Sometimes, the organic layer can be left to evaporate or syringed out, so the final transfer occurs through the air-liquid interface. For this method to produce single or few-layers films the synthetic conditions (solvents, concentrations, reaction time, temperature, etc.) have to be carefully selected. In spite of this, it is not always possible to obtain them if interlayer interactions are strong. The thickness and lateral size of the nanosheets produced with this methodology can usually vary between micro and nanometres. However, some works by Nishihara and collaborators have reported centimetre-sized and defect-free sheets by LL interfacial synthesis although additional crystallographic evidence is still desirable in order to support these claims.[285] Regarding conductive MOG systems, several of them have been prepared as nanosheets using LL interfacial synthesis, mainly by Nishihara and co-workers. Thus, the first system was Ni-BHT in 2013[135] followed by Pd-BHT,[137] Cu-BHT,[131,145] Co-BHT,[136] Ag-BHT,[133] Ni-IT,[139] Ni-AT,[140] Ni-HIB, Cu-HIB, Co-HIB,[141] THTA-Co,[147] Co-HTTP[149] and Cu-CAT-1.[156]

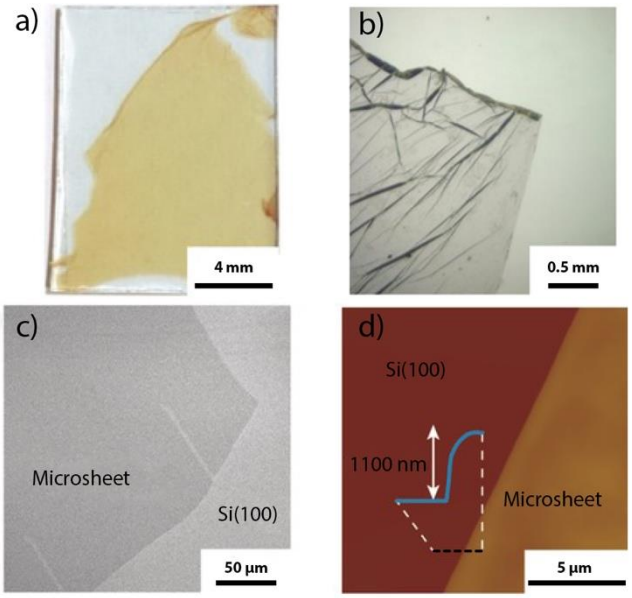

Figure 17. a) Representative photograph of a bis(dipyrrinato)zinc(II) microsheet transferred to a quartz substrate. b) Optical microscopic image of the microsheet on a silicon(100) substrate. c) SEM image of the microsheet on a silicon(100) substrate. d) AFM image of the microsheet on a silicon(100) substrate with a cross-section profile (blue line) taken along the black line. Reproduced from ref. 289 with permission from Wiley, copyright 2017.

The obvious limitation of the interface synthesis is imposed by the size of the reaction vessel and the low control over the substrate coverage. There are no means to repair cracks or empty space that appear between individual sheets (**Figure 17**). The use of organic solvents and the need to have a steady LL or AL interfaces to minimize defects also make this method hardly compatible with high-temperature synthesis. In 2010, Makiura *et al*. introduced the Langmuir-Blodgett (LB) technique[292] as an elegant method to overcome some of these limitations and gain control of the interfacial area coverage.[293] The LB technique is an elegant method for the fabrication of well-defined layered structures with precision at a molecular level. A picture of a standard LB through is depicted in **Figure 18a**. Once a floating CP or MOF has been formed at the AL interface two barriers are used to reduce available interface area bringing individual sheets together (**Figure 18b**). Using a Wilhelmy plate the changes in surface pressure (π), defined as the difference in surface tension (σ) measured between a clean subphase and a surfactant-covered subphase, can be measured. The plot of π as a function of mean molecular area (MMA) at the interface, calculated from the known number of molecules dispersed in the area left available by the barriers, is known as a compression isotherm (**Figure 18c**). The study of these isotherms renders very useful information about the behaviour of the floating layer. As shown in **Figure 18c**, at the initial point of a π-MMA compression isotherm, π is almost 0 as there is plenty of empty space between the sheets of the dispersed layer. Then, as the sheets are brought closer together by barrier compression, π increases as the available area and MMM decreases. Initially this raise is minimal as molecules still have plenty of space available (distance between adjacent sheets is large and their interactions are weak), there is little effect on the surface tension of the subphase. Then as MMA is further reduced and sheets start to adopt more compact packing (sheets begin exerting a repulsive effect on each other), the slope of the π-MMA isotherm becomes very steep. Finally, if the barriers keep advancing until the layer cannot be further compressed, it collapses forming either thicker crystalline aggregates or they submerge in the subphase by dissolution or micelle formation. This collapse produces an inflexion point in the isotherm, and if the molecule is coloured the collapse can also be observed by the naked eye.

The LB set-up also includes a dipping mechanism or dipper, which allows the transfer of the compressed floating film to the substrate, either with its surface parallel or perpendicular to the interface. This whole process can be repeated several times for two-dimensional CP or MOF ultrathin film of the desired thickness. There are two main transfer modes: vertical and horizontal. In the vertical transfer the substrate is firstly immersed through the floating film and then emerged or vice versa. In the first scenario, floating film can be transferred to the substrate in the downwards and upwards motion. In the horizontal transfer mode or Langmuir-Schaefer (LS) deposition,[294] the substrate surface and the floating monolayer make contact horizontally, either by stamping the surface from above or by pulling the substrate from inside the subphase.

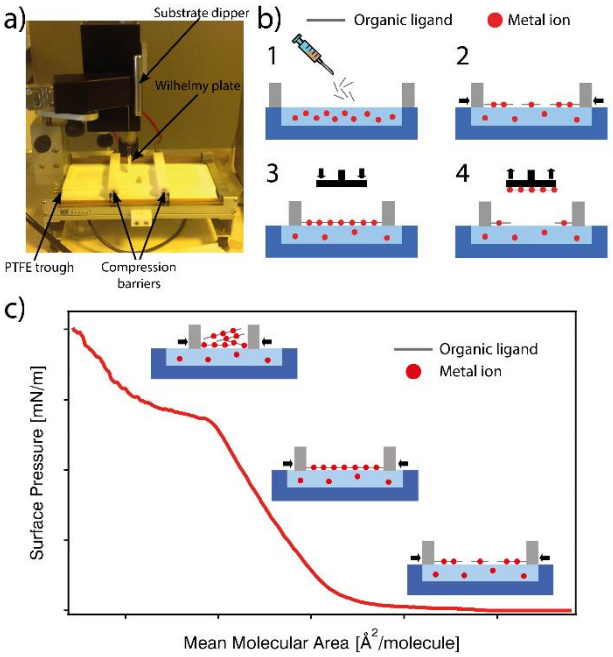

Figure 18. a) Photograph of a Langmuir mini-trough. b) Schematic illustration for MOF/CP nanosheet formation, compression and transfer to a substrate in a LB trough. c) π-MMA compression isotherm with schemes illustrating the different stages of film growth with decreasing MMA, from the initially isolated nanosheets that are compressed to a continuous layer, to the final collapse state.

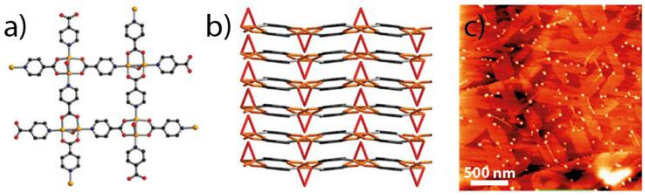

Figure 19. a) Detail view of the copper environment in a $[Cu_2Br(IN)_2]_n$ single layer, b) Superposition of layers along the a axis, c) AFM topography image of $[Cu_2Br(IN)_2]_n$ after liquid phase exfoliation and deposition on HOPG. Reproduced from ref. 109 with permission from the Royal Society of Chemistry.

Early reports by Makiura *et al.* reported the formation and transfer to a substrate of the layered CP $[Cu_2(py)_4(CoTCPP)]$ (py = pyridine; TCPP = 5,10,15,20-tetrakis(4-carboxyphenyl)porphyrinato),[293,295,296] which curiously does not exist in the bulk form. Later, the same authors prepared a series of related porphyrin MOFs, including $[Cu_2(H_2O)_2(H_2TCPP)]$ or NAFS-2,[297] NAFS-21[298] with 5,10,15,20-tetra(4-pyridyl)-porphinato zinc(II), NAFS-13 or $[Cu_2(H_2O)_2(PdTCPP)]$,[299] and NAFS-31 and 41,[300] which are equivalent to NAFS-2 but with trans-ditopic and expanded tetratopic porphyrins respectively. After NAFS-1, the LB technique has been used to fabricate ultrathin films of other MOFs. Feng and co-workers prepared single-layer sheets of the MOGs $Ni_3(HTTP)_2$[150] and THTA-Co[147] but unfortunately the substrate coverage was not continuous. Nishihara and co-workers had done something analogous with Ni-BHT.[301] Similar films of a different 2D Cu^{II} MOF were prepared by Ruoff and collaborators.[302] Later Moradi *et al.* also prepared monolayers of 2D Cu^{II} CP with a complex 3D calix[4]arene amphiphile. The carboxylate and alkyl chains in the ligand are located in opposing sides, thus guarantying a particular orientation on the water surface.[303] In all these cases, the floating films were transferred to bare hydrophilic substrates (i.e. Si/SiO_2, Au, quartz, etc). Rubio-Giménez *et al.* later proved how the hydrophobicity of the substrates plays a key role in the transfer process by using NAFS-1 as a model system.[304] Brewster angle microscopy (BAM) images of the floating film showed that it was continuous, but the final film once transferred to a bare hydrophilic substrate was rather discontinuous for the case of Si/SiO_2 whilst in the case of clean metallic substrates there was barely any transfer at all. By functionalizing these substrates with the appropriate alkyl self-assembled monolayers (SAMs), they turned highly hydrophobic and the transferred films were then continuous with full coverage for all surfaces. This hydrophobicity effect in LB transfer was latter replicated with Cu-CAT-1 films.[156] The LB method is not exclusively limited to the bottom-up assembly of ultrathin nanosheets and can be also used to produce MOF thin films by sequential transfer of dispersions of NPs.[305,306]

4.1.2. Top-down deposition

Although extensively developed mainly for graphene,[307–309] and inorganic 2D materials like transition metal dichalcogenides (TMDs),[310,311] layered double hydroxides (LDH),[312] and many others,[313,314] liquid phase exfoliation has also been used to prepare dispersions of layered CPs and MOFs that are then transferred to the surface. Exfoliation in a liquid phase usually requires the assistance of ultrasonication to achieve delamination into a suspension that is easily processable. As a result, liquid exfoliation has been widely used to produce nanosheets of a variety of 2D CPs and MOFs,[286,287,315] including a couple of MOGs[153] and other conductive 2D frameworks.[316] For instance, Amo-Ochoa *et al.* used sonication to delaminate mixed-valence a copper CP $[Cu_2Br(IN)_2]_n$ (IN = isonicotinato) crystal into 5 nm sheets and deposited them as films on graphite surfaces (**Figure 19**).[109] Moreover, liquid exfoliation has also been used to prepare monolayer flakes of a 2D SCO materials. Thus, Lei and Zheng exfoliated single layers of $[Fe(4\text{-}PyP)(H_2O)][Pt(CN)_4]\cdot H_2O\cdot CH_3OH$ (4-PyP = diethyl 4-pyridylphosphonate), a 2D Fe^{II}-HCP by ultrasonication in water.[317] Ruiz-Molina and collaborators did the same with a different 2D CP. Despite thicknesses being rather polydisperse, they were still able to find few single layer flakes.[318]

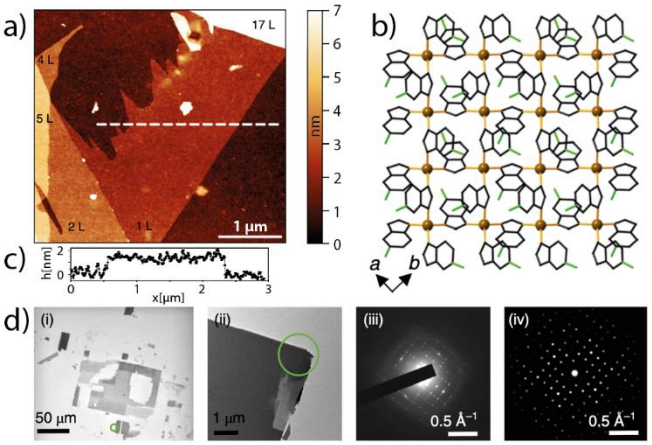

Figure 20. Mechanical exfoliation of a layered CP into atomically thin sheets. a) AFM image and height profile of a flake of MuV-1-Cl b) Structure of a single layer of MUV-1-Cl viewed along the c axis. c) TEM images and SAED patterns for MUV-1-Cl flakes. Reproduced from ref. 319 with permission from Springer Nature, copyright 2018.

However, indiscriminate sonication normally reduces the lateral size of the sheets from micro to few hundred nanometres and hinders their crystalline quality in comparison to those obtained by micromechanical exfoliation. As a result, a few examples of wet exfoliation that do not require ultrasonication have recently appeared. Sonication can be avoided by solvent-induced delamination[320,321] or chemical exfoliation.[322] From the chemical point of view, a particularly elegant example is the chemical exfoliation of $[Zn_2(Pd\text{-}TCPP)]$ recently reported by Zhou and co-workers.[323] First, the 2D CP was intercalated with a bidentate 4,4'-dipyridyl disulphide ligand that coordinated to Zn^{II} of adjacent layers, then the disulphide bond was broken by chemical reduction with trimethylphosphine, thus generating nanosheets in high yields.[323]

Liquid phase exfoliation does not require large single crystals as starting materials and is commonly considered as an efficient method to produce a big quantity of nanosheets in solution. Oppositely, solvent-free micromechanical exfoliation is the preferred method to produce highly crystalline nano and microsheets of a layered material. Physical exfoliation is done without chemical disturbance by applying simple mechanical

force to a bulk crystal. The sheets deposited onto a substrate using this method are thus only formed by single crystalline domains. However, there are clear practical limitations to this method, from the difficulty in controlling the thickness and lateral size distribution of the exfoliated sheets; especially in the case of soft materials like CP and MOFs, to the low substrate coverages and exfoliation yields that can be achieved. Moreover, relatively large single crystals are needed for this method to work, specially using the scotch tape technique, this can is specially challenging when dealing with CPs. Still, there are a couple of interesting examples in the literature. Coronado and co-workers reported the first example of a mechanically exfoliated CP with $[Fe(acac_2\text{-trien})][MnCr(Br_2An)_3]\cdot(CH_3CN)_2$ which is formed by neutral honeycomb layers. Very recently, this team also achieved atomically thin microsheets of MUV-1, a family of Fe^{II} benzimidazole 2D CPs, via mechanical exfoliation (**Figure 20**).[319]

4.2 *In situ* film growth in presence of the substrate

In this strategy substrate and CP or MOF precursors share the same reactor space during material synthesis. In the simplest case, reaction conditions similar to those for bulk material synthesis are used, but in the presence of a substrate that can be chemically modified to assist and/or orient the film growth. When the reaction has finished, a film is formed on the substrate, most often along with a powder precipitated at the bottom of the reactor container.[324,325] For example, Kung *et al.* used the solvothermal method to grow MOF-525 films on conducting glass substrates from its components (meso-Tetra(4-carboxyphenyl)porphyrin (H_4TCPP) linkers and hexa-zirconium nodes).[326] As visible in **Figure 21**, cubic crystals ranging from 500 nm to 1000 nm embed into each other all over the substrate.

Zacher *et al.* showed that the nature of the surface and especially its acid/base properties, influence whether a film can grow or not. The authors suggested that binding between the surface and the film is mediated by the organic linker, and therefore a MOF that contains acid linkers like HKUST-1 cannot grow on acidic surfaces such silica.[325] However, a MOF that contains both acidic and basic linkers such as $[Zn_2(BDC\text{-}Br)_2(DABCO)$; (DABCO = 1,4-diazabicyclo[2.2.2]octane)] can growth on both silica an alumina. Arnold *et al.* reached similar conclusions by studying the anisotropic growth of $Mn(HCO_2)_2$ on alumina and graphite.[324] As a result, the use of organic molecules has been proposed to improve heterogeneous nucleation and growth. Huang *et al.* treated a porous Titania support with 3-aminopropyltriethoxysilane (APTES). This molecule can bind to the surface by the silane group and to ZIF-22 $[Zn(ABLM)_2$; (ABLM = 5-azabenzimidazole) crystals through the terminal amino group.[327] As a result, thick (40 µm) and well-intergrown films of higher quality than the ones obtained without the linker were obtained. The same phenomenon has been observed for ZIF-90 $[Zn(C_4H_3N_2O)_2]$.[328]

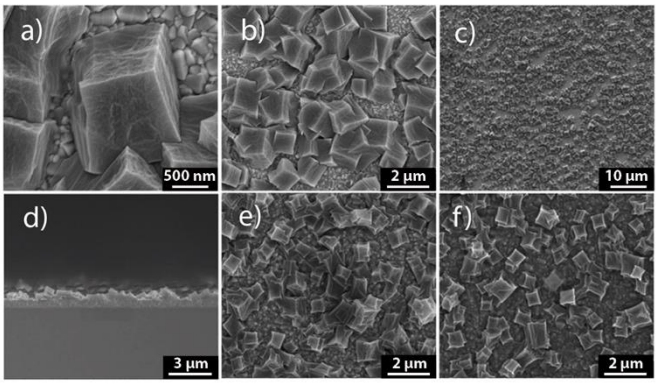

Figure 21. SEM images of MOF-525 polycrystalline thick films prepared via solvothermally growth. Reproduced from ref. 326 with permission from the Royal Society of Chemistry.

Usually, MOF synthesis takes place in solvothermal conditions. However, microwave-heating approaches have been developed for bulk materials synthesis and have been extended to films.[329] The advantage of this method over conventional heating is the increased nucleation rate. Indeed, a few hours is enough to archive full crystallization. This method was introduced by Yoo *et al.* using a substrate (porous alumina) coated with a conducting layer, such as graphite or gold, and immersed in a MOF-5 $[Zn_4O(BDC)]$ precursors solution. Upon microwave irradiation, the temperature of the conductive layer increased rapidly and introduced fast heterogeneous nucleation for MOF-5 crystals.[330] Later, Bux *et al.* used this microwave-assisted deposition to prepare a 40 µm thick ZIF-8 film on porous Titania that exhibits molecular sieving properties.[331]

A variation of the above ideas consists on modifying reaction/nucleation rates controlling the concentration/diffusion of one of the reagents involved. For instance, gel-layer synthesis to better control nucleation over the surface. This method was originally applied to MOFs by Yaghi and co-workers to grow Zn(HBTC) (HBTC = 5-carboxy-benzene-1,dicarboxylate dianion).[332] Later, Schoedel *et al.* employed this method to grow HKUST-1 and Fe-MIL-88B-NH_2 films on a -COOH or -OH terminal alkanethiolate SAM functionalized Au-substrates. They immersed the substrates in poly (ethylene oxide) gel loaded with metal-ion precursor (Cu^{2+} or Fe^{3+}) and then carefully added the linker solution (H_3BTC or $H_2(NH_2\text{-BDC})$ on the top of the gel layer. The morphology and thickness of the resulting MOF film could be controlled by the length of the poly(ethylene oxide) and the concentration of the metal ions in the gel. The thickness of Fe-MIL-88B-NH_2 film was estimated to be 40 nm.[333]

An electrochemical method to control the reaction rate was originally developed by researchers at BASF.[334] The principle was based on supplying the metal-ion, by anodic dissolution to a solution that contained the organic ligand and a conducting salt. Careful modification of the conditions used to electrochemically produce bulk MOF material enabled the preparation of thin films. This process was demonstrated with HKUST-1, by applying an anodic voltage to the copper electrode in the presence of a solution containing BTC and

methyltributylammnium methyl sulfate (MTBS) as conduction salt. Films of well packed HKUST-1 crystals with thicknesses in the range 2 to 50 µm were obtained bycontrolling the synthesis conditions.[335]

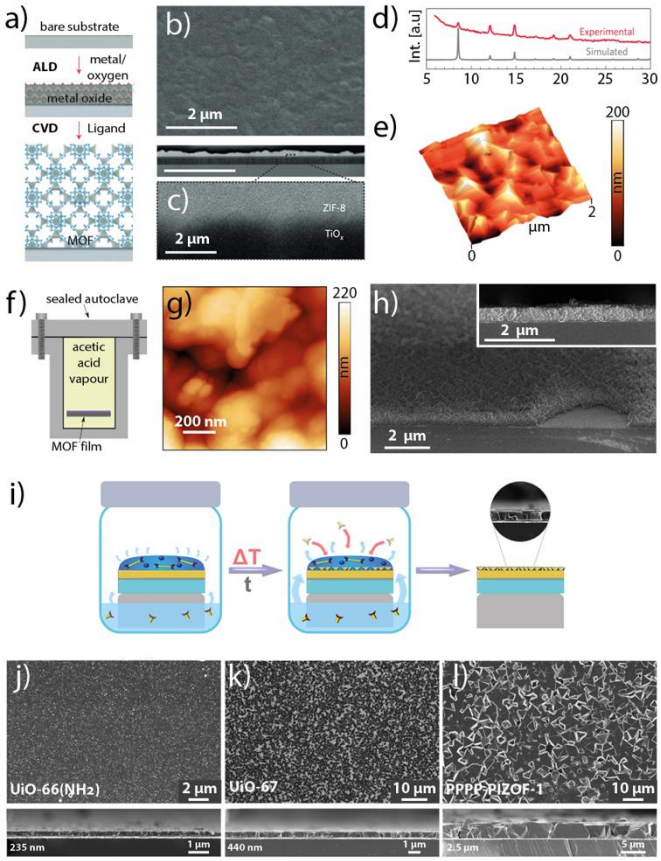

Figure 22. a) Chemical vapour deposition of ZIF-8 thin films. The procedure consists of a metal oxide vapour deposition and a consecutive vapour–solid reaction, b) Scanning electron microscopy top view, c) Focused-ion beam TEM cross section. Inset: high-resolution magnification of the interface between ZIF-8 and the substrate., d) X-ray diffraction pattern of a ZIF-8 CVD film and simulated pattern for ZIF-8, e) 3D rendered AFM topography. f) Experimental setup for heat post-deposition crystallization treatment of the films in acetic acid vapour, g) AFM image of the Zr-1,4-BDC film after treatment in acetic acid vapour, h) Cross-section SEM images of the same surface viewed at 45°and 90° angles. i) Schematic representation of the VAC process for the fabrication of oriented MOF films. Top and cross-section SEM views of j) UiO-66(NH_2), k) UiO-67 and l) PPPP–PIZOF-1 films. a-e) Adapted from ref. 336 with permission from Springer Nature, copyright 2016. f-h) Adapted from ref. 337, licensed under CC BY 4.0, published by the Springer Nature. i-l) Reproduced from ref. 338 with permission from American Chemical Society, copyright 2018.

In-situ growth can also be achieved by confining the reaction to the gas-solid interface, thus avoiding the use of solvents. Ameloot and collaborators used this approach to fabricate homogeneous pinhole-free 50 nm films of ZIF-8 with high-aspect-ratio features in a highly controlled manner (**Figure 22a-e**). An atomic layer deposited (ALD) nanometric ZnO film was reacted with the chemical vapour deposited (CVD) ligand to yield the final MOF film.[336] Afterwards, this strategy has been optimized for ZIF-8[337–339] and successfully applied to many other MOFs.[188,340–342] In the case of Nilsen of co-workers, they successfully produced UiO-66 and UiO-66(NH_2) films over silicon substrates by exposing to acetic acid vapours Zr^{4+}-BDC mixtures generated by the sequential Atomic/Molecular Layer Deposition (ALD/MLD) of $ZrCl_4$ and BDC precursors over silicon substrates (**Figure 22f-h**).[343,344] Lastly, vapour-assisted conversion (VAC) is another thin film fabrication methodology at the edge of vapour and liquid synthesis that was first developed for covalent organic frameworks (COFs) by Medina and co-workers.[345] In the MOF version, substrates coated with a drop of the transition metal/ligand precursor solutions are exposed to modulator/solvent vapour mixtures. They used VAC to successfully fabricate various not only 3D Zr-based MOFs (**Figure 22i-l**)[346] but 2D triphenylene MOGs (Co-CAT-1, Ni-CAT-1 and Cu-CAT-1).[187] This VAC technique is highly versatile in terms of the dimensionality and nature of the MOFs that can be prepared and is not limited to sublimable building blocks that is currently one of the main limitations of the CVD and ALD/MLD approaches.

4.3 Sequential growth by Layer-by-Layer/Liquid phase epitaxy

A third strategy, the so-called LbL approach involves the sequential growth of the ultrathin film by consecutive exposure of the substrate to the building blocks of the CP or MOF in question (**Figure 15**). In this strategy, metal and ligand building-blocks do not share the reaction space at the same time. The LbL procedure was pioneered by Mallouk and co-workers to fabricate thin films of various CPs,[347–349] although it had been previously used for other materials.[350] Years later, it was extensively employed by Fischer, Wöll and collaborators to fabricate MOF ultrathin films, also referred as SURMOFs.[351–354,] They also rebranded the technique as liquid phase epitaxy (LPE).[355,356]

In the simplest case, a LbL growth cycle consists of consecutive immersion of the substrate into a solution of the metal ion or the organic linker with intermediate washing steps using pure solvent.[357,358] This gives each of the components the opportunity to saturate all deposition sites without the formation of new nuclei at the surface or in solution. Between each step, the sample is rinsed with solvent to remove uncoordinated precursors. Under ideal conditions, every cycle should imply the deposition of a single unit cell. This linear growth mode allows to adjust the final thickness of the film to the number of cycles. The previous functionalization of substrates with SAMs that have the appropriate head group to modify surface properties or coordinate to the metal ions and thus direct film growth for the following growth cycles is a common practice.[359] The resulting films are in general highly crystalline, smooth, homogeneous and cover the whole area of the substrates that was functionalized with the appropriate head groups,[351,353–355,360–362] and is thus compatible with the deposition of patterned features.[360] The head group and the packing of the SAM also controls orientation of the resulting MOF or CP.[363] However, most studies have only focused on the out-of-plane orientation. Hence, heteroepitaxial methods that use oriented hydroxide precursors matching the MOF's lattice parameters have been developed to control both in-plane and out-of-plane orientations.[364,365]

Concerning LbL techniques, a simple manual dipping method was reported by Mallouk *et al.* for the sequential deposition of

[Ni(bpy)Pt(CN)$_4$] (bpy = 2,2'-bipyridine).[349] Wöll, Ocal and co-workers used the dipping process to selectively graft HKUST-1 over COOH regions of a gold mercaptohexadecanoic acid (MHDA)/hexadecane thiol (HDC) patterned substrate.[366,367] The substrate was successively was sequentially immersed in $Cu(OAc)_2$ and H_3BTC ethanolic solutions, between each immersion the sample was rinsed with ethanol and dried with N_2 stream. This same dipping process was later automatized by Gu *et al.* using an automatic robot dipper. Moreover, they found that the MOF films that were prepared under ultrasonication had cleaner and more homogenous surfaces and reduced their root mean square roughness from 38 to 10 nm (**Figure 23**).[368]

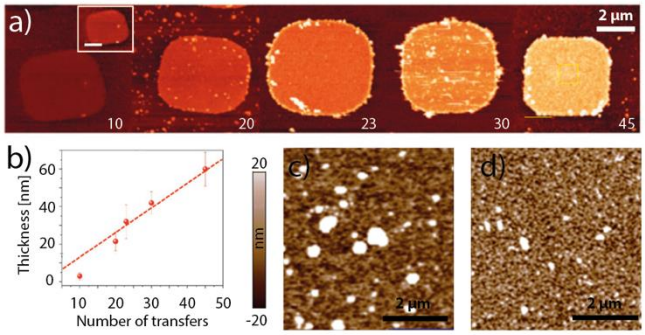

Figure 23. a) Series of topographic AFM images for different HKUST-1 samples deposited on a MHDA/ HDC patterned substrate corresponding to 10, 20, 23, 30 and 45 immersion cycles. The total color scale (total height range) is 110 nm for all the images. Because of the low topography of the 10 cycles sample, the inset shows the same image with the scale magnified by a factor of two, inset scale bar is 2 µm. b) Film thickness as a function of the number of immersion cycles. AFM images of HKUST-1 SURMOFs prepared without ultrasonication c) and with ultrasonication d). The surface roughnesses are 35 nm (c) and 6 nm (d). a-b) Adapted from ref. 367 with permission from the PCCP Owner Societies. c-d) Adapted from ref. 368 with permission from Elsevier, copyright 2015.

A continuous flow method was used by Wöll and co-workers to synthesize Cu and Zn-MOF-2 [M(BDC); M = Cu or Zn] ultrathin films.[369] In this report, four pumps were connected to a sealed chamber. Two pumps were used for controlling the reaction time with the precursor [$M_2(CH_3COO)_2{\cdot}H_2O$] (M= Cu or Zn) and H_2BDC to 30 and 60 minutes respectively. Another one, controlled the rinsing time, and the fourth one was responsible for pumping out the solution from the reactor. As shown in **Figure 24a**, this method has also been used to epitaxilly grow other 2D SURMOFs such as Zn-TCPP, in which consequtive layers are connected by van der Waals forces.[370] In addition, Quartz Crystal Microbalance (QCM) and Surface Plasmon Resonance (SPR) have been widely reported as complementary methods to monitor the amount of material deposited during the process. For example, Shekhah has recorded the sequential injection of $Cu(Ac)_2$ (Ac = Acetyl group) and H_3BTC and then rinsed with ethanol on a functionalized QCM electrode.[371] Moreover, these techniques can be used to obtain information about film porosity after the growth is finished.[306,335,372–379]

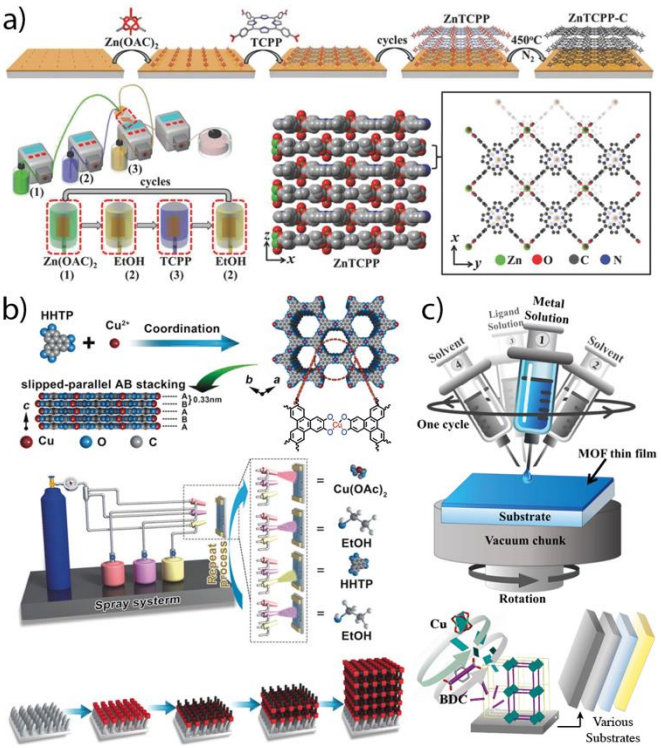

Figure 24. Examples of LbL fabrication methods by a) continuous flow, b) controlled spraying and c) sequential spin-coating of Zn-TCPP, Cu-CAT-1 $Cu_2(bdc)_2{\cdot}xH_2O$ thin films respectively. a) Reproduced from ref. 370 with permission from Wiley, copyright 2018. b) Reproduced from ref. 380 with permission from Wiley, copyright 2017. c) Reproduced from ref. 381 with permission from American Chemical Society, copyright 2016.

The spray method is related to the dipping method.[382] In this case, a spray system is adapted to dispense the reagents (**Figure 24b**). This approach has been used to grow MOFs ultrathin film with fast speed and keeping a high degree of crystallinity and orientation. In this method, there are three nozzles for spraying the solutions including metal salts, organic ligands, and rising solvent, respectively. As a proof of concept, HKUST-1 was again selected to demonstrate the efficiency of this method by Wöll's group.[382] Carboxylic acid terminated SAM-modified substrates were alternately exposed to aerosol mixtures containing $Cu(OAc)_2$ or H_3BTC produced by spray nozzles. Like the other methods, the removal of residual reactants (metal source, organic linkers) was achieved by exposing the substrate to an aerosol produced from the pure solvent. As depicted in **Figure 24b**, controlled spraying LbL can also be used to produce films of 2D systems such as Cu-CAT-1.[380] Also, the spin-coating method is an effective way to prepare thin and homogeneous films out of solutions on flat substrates. In 2009, Vozar *et al.* reported an automated spin-assisted layer-by-layer assembly.[383] In this system, a substrate is rotated rapidly, and precursors and cleaning solution are deposit onto the substrate, typically using a nozzle impinging upon the center of the substrate. The rapid spinning of the sample produces a thin layer over the full substrate area. This setup was originally used to fabricate polymer-clay nanocomposites and was recently adapted by Chernikova *et al.* to grow $Cu_2(BDC)_2{\cdot}xH_2O$ (**Figure 24c**), ZIF-8 and HKUST-1 ultrathin films.[381]

The LbL method has also been extensively applied to SCO films, of Fe^{II}-HCPs. After the first HCP films of $[Ni(bypy)Pt(CN)_4]$ were grown by Mallouk and co-workers,[349] a series of 3D Fe^{II}-HCPs films were grown by Bousseksou, Real and collaborators. These include $[Fe(pz)Pt(CN)_4]$,[384,385] $[Fe(azpy)M(CN)_4]$ (M = Ni, Pd or Pt),[386] $[Fe(bpac)Pt(CN)_4]$,[226,387] Afterwards, Kitagawa and co-workers structurally validated the growth of $[Fe(py)_2M(CN)_4]$, proving via synchrotron XRD that the films were crystalline and preferentially oriented with the metal-cyanide layers parallel to the substrate.[388,389] They also reported the oriented growth of a new accordion-like 3D Fe^{II}-HCP: $[Fe(H_2O)_2(bpy)][Pt(CN)_4]\cdot H_2O$.[390] Unfortunately, due to the fast exchange dynamics for Fe^{2+}, the LbL procedure for all these 3D Fe^{II}-HCPs, requires very low temperatures (-60ºC) in order to achieve a regular epitaxial growth and avoid Fe^{2+} desorption in the washing steps. Kitagawa and co-workers later extended this LbL method to ultrathin films (16 nm thick) of 2D Fe^{II}-HCPs: $[Fe(py)_2Pt(CN)_4]$[244,391] and $[Fe(py)_2Ni(CN)_4]$,[392] which could be grown at room temperature unlike their 3D counterparts. Moreover, $[Fe(py)_2Pt(CN)_4]$ films below a certain thickness limit (<22 nm) displayed a gate-opening behaviour that allowed solvent uptake in-between the layers of this non intrinsically porous framework.[244] Kitagawa's group procedure for $[Fe(py)_2Pt(CN)_4]$ films was latter improved by Rubio-Giménez *et al.* by adapting the LbL set-up into a N_2-filled glovebox, thus avoiding Fe^{2+} oxidation and improving the quality of the films in the ultrathin film range (~1-22 nm).[393] The same research team also extended this procedure to two other 2D Fe^{II}-HCPs $[Fe(pym)_2Pt(CN)_4]$ and $[Fe(isoq)_2Pt(CN)_4]$ in a study of the influence of the axial ligand onto the gate-opening solvent uptake.[246]

The ALD/MLD technique can also be used in a LbL fashion to build CPs and MOFs in a more aligned way to current CMOS technologies.[394,25] Karppinen and co-workers have been working extensively on this procedure, which involves consecutive self-terminating reactions. Thus, in it the framework is sequentially built via independent gas pulses of the organic ligand and a reactive metal precursor. This procedure has been moderately successful, as most of the prepared films are either amorphous,[395–398] require a separate recrystallization under a solvent atmosphere[399–401] or their diffractograms do not clearly match a known structure.[402–404]

4.4 Nanostructuration effects on the spin crossover transition

The integration of Fe^{II} SCO materials in functional nanodevices has attracted substantial attention in recent years.[29,201–204,405] However, there is still a long way to go and additional efforts need to be made in the study of the relationship between physical properties and the spin state. Processing SCO materials at the nanometric scale has proven to have very significant effects on all aspects of the SCO phenomena.[29,406–410] These include: i) the stabilization of one of the spin states, which affects the transition temperature; ii) the cooperativity between the SCO centers, which affects the abruptness of the transition and the width of its hysteresis and iii) the presence of defects, which affects the completeness of the transition. These properties can be altered by changes in the film thickness, sizes and shapes of crystallites; film orientation; substrate coverage and interactions with other SCO particles or non-SCO substrates or matrixes. Understanding the relationship between the characteristics of the film and the SCO properties is a key requirement to fabricate viable devices.

Regarding SCO CPs and MOFs, again most studies has been done with the 1D CP $[Fe(Htrz)_2(trz)]^+$ and Fe^{II}-HCPs, for which there is an extensive amount of reports about nanostructuration effects on NPs, which have been already covered by various reviews.[406,29,407–410] Nonetheless, the study of NPs adds other variables to the problem that are difficult to control such as size polydispersity, chemical composition changes or surface defects. The main consequence of nanostructuration is the size reduction effect. These can be divided into surface and confinements effects. In general, the first ones dominate for particles larger than 5-10 nm, whilst confinements effects only acquire importance in smaller particles.[29]

Largely, experimental observations in NPs relate the decrease in particle sizes (increase of surface-to-volume ratio) with a decrease in cooperativity (increasingly gradual SCO transitions and narrower hysteresis, lower transition temperatures (stabilization of the HS state) and less complete transitions (increase of the residual HS fraction). This has been consistently observed for both 2D and 3D Fe^{II}-HCPs. For instance, in NPs of $[Fe(pz)Pt(CN)_4]\cdot nH_2O$ studied both by the groups of Real and Mallah. The former prepared surfactant-free particles of

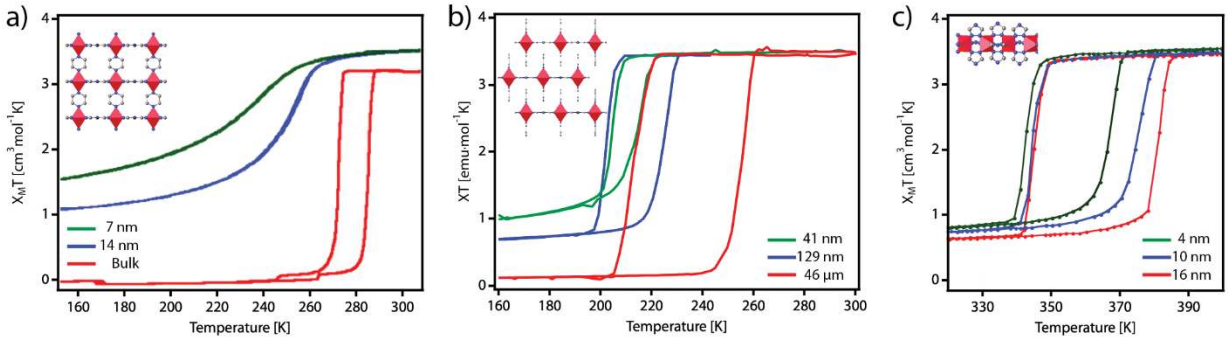

Figure 25. Evolution of the temperature dependence of the molar magnetic susceptibility for SCO NPs of different sizes of $[Fe(pz)Pt(CN)_4]$, a 3D Fe^{II}-HCP (a); $[Fe(py)_2Pt(CN)_4]$, a 2D Fe^{II}-HCP (b); and $[Fe(Htrz)_2(trz)](BF_4)$, a 1D CP (c). Insets show the crystal structures of the different materials. a) Adapted from ref. 412 with permission from American Chemical Society, copyright 2008 b) Adapted from ref. 393, licensed under CC BY 3.0, published by the Royal Society of Chemistry. c) Adapted from ref. 417 with permission from the Royal Society of Chemistry.

230x230x55 nm and 61x61x21 nm,[411] whilst the latter studied much smaller particles (7 and 14 nm, **Figure 25a**).[412] Regardless, both observed a decrease in cooperativity, lower transition temperatures and an increase in the residual HS fraction, went along with the decrease in particle size. Similar results were obtained by Real, Gaspar and collaborators with a series 2D Fe^{II}-HCP: $[Fe(3\text{-}Fpy)_2M(CN)_4]$ (3-Fpy = 3-fluoropyridine; M = Ni, Pd, Pt). The SCO properties of surfactant-free nanocrystals of 400x400x30 nm, were compared with NPs in the range 200-70 nm prepared using the coating polymer poly(vinylpyrrolidone) (PVP).[413] Rubio Giménez *et al.* also observed the same effect with nanocrystals of $[Fe(py)_2Pt(CN)_4]$ (**Figure 25b**).[393] On the other hand, confinement effects manifested in ultrasmall particles of $[Fe(pz)Ni(CN)_4]$ prepared by Bousseksou, Salmon and co-workers. They observed a higher transition temperature in 2-4 nm NPs and even the reappearance of a hysteresis loop.[414,415] However, it must be noted that the chemical composition of the NPs and the surfactant were not constant in these cases. Per contra, although their SCO properties follow the same trend with downsizing, NPs of $[Fe(Htrz)_2(trz)]^+$ compounds seem to be much less sensitive to size reductions effects.[254,416] For example a hysteresis of 24 K was detected for 4 nm NPs (**Figure 25c**).[417] This can be rationalized in terms of the relative number of Fe^{II} centres potentially exposed to surface effects. This is logically higher for 2D and 3D Fe^{II}-HCPs than for a 1D chain CP. Strangely, a recent report by Galán-Mascarós and co-workers showed that particle size reduction and defect generation in $[Fe(trz)(Htrz)_2][BF_4]$ nanocrystals via ball milling, caused a wider hysteresis loop without affecting the completeness of the SCO transition.[418] The physical environment around the particles has also got a significant influence on the SCO transition. Several reports have examined these matrix effects,[414,419] the magnitude of which depends on the chemical and physical properties of the matrix, which helps or hinders the propagation interactions of the SCO transition. A matrix can be viscous liquid media, an organic polymer or a shell attached to the NP itself. Moreover, the matrix can govern interparticle interactions promoting cooperativity by transmitting the elastic vibrations of the spin switching.[420]

In addition to NPs there has been extensive work in the literature on ultrathin films of discrete Fe^{II} complexes prepared by vacuum sublimation. Thus, few-layer to sub-monolayer films have been prepared onto different substrates and their SCO properties examined using STM and XAS. Thermal evaporation of these complexes allows a precise control over film thickness. However, it requires complex equipment and is limited to a relatively small collection of sublimable compounds. Furthermore, the resulting films are typically amorphous, unless they are recrystallized afterwards,[421,422] which in combination with interactions with the substrate can strongly affect their SCO properties. These studies are out of the scope of this work and been recently reviewed by Ruben and Kumar.[423]

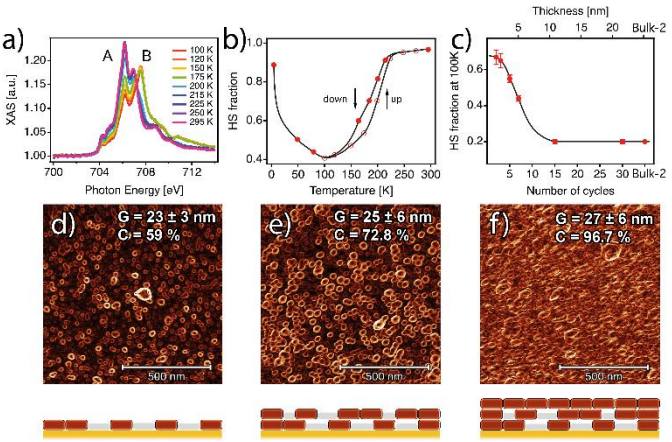

Figure 26. SCO behaviour of $[Fe(py)_2Pt(CN)_4]$ ultrathin films analysed with XAS data and correlation with film microstructure. a) XAS spectra as a function of temperature for a 7-cycles $[Fe(py)_2\{Pt(CN)_4\}]$ thin film. b) HS fraction as function of the temperature for the 7-cycles film. c) HS fraction at 100 K as a function of the number of cycles (1 cycle ≈ 0.72 nm). 1 x 1 μm^2 AFM topography images of 2 (d), 5 (e) and 10 (f) cycles after being processed with a Prewitt operator to highlight particle edges. The changes in the microstructure of the films with the number of cycles were monitored by analysing mean lateral grain size (G) and film coalescence (C) on 1 x 1 μm^2 AFM images. Schematic illustrations of the microstructure of each film are shown below each AFM image, showing the evolution from a film composed by isolated nanocrystals to a fully-coalesced one. Adapted from ref. 393, licensed under CC BY 3.0, published by the Royal Society of Chemistry.

In contrast with NPs and discrete complexes, the nanostructuration effects in crystalline thin films of SCO MOFs and CPs have been largely overlooked. As discussed in the previous sections, in the category of SCO MOFs and CPs, mainly Fe^{II}-HCPs have been grown onto solid substrates using the LbL method. As with thermal evaporation, LbL also allows for a precise control of film thickness by defining the number of growth cycles. Furthermore, LbL yields highly crystalline films with preferential orientation with respect to the substrate. The study of the magnetic properties of this Fe^{II}-HCPs thin films at the nanometric limit can be considered a challenging task, as conventional techniques such as SQUID magnetometry or Raman spectroscopy are not sensitive enough. Both of them require relatively thick films to get a good signal-to-noise ratio. Thus, films of a minimum thickness close to 100 nm are often required to observe the SCO transition, far from the threshold for which nanostructuration effects are expected to appear. This is the case for the series of 3D Fe^{II}-HCP thin films reported by Real, Bousseksou and collaboratorswhich were studied in that thickness range. Consecuently, authors barely noticed any difference in the SCO properties between bulk references and thin films of $[Fe(pz)Pt(CN)_4]$,[384] $[Fe(azpy)M(CN)_4]$ (M = Ni, Pd or Pt),[386] $[Fe(bpac)Pt(CN)_4]$,[226,387] except for a slight change in the transition temperatures. The $[Fe(bpac)Pt(CN)_4]$ publication features the thinnest film measured via Raman spectroscopy (16 nm, 10 growth cycles), which also does not show any significant difference with the SCO behaviour of the corresponding bulk reference sample.[387]

In the only study to date of a $[Fe(py)_2Pt(CN)_4]$ in the ultrathin film range (<20 nm), Martí-Gastaldo and collaborators studied the dependence of the SCO properties with the film thickness (**Figure 26**). Variable temperature XAS was used to characterize

the spin state in the ~1-22 nm thickness range (1-30 LbL growth cycles). Thus, the authors analysed the XAS spectra together with the AFM characterization of the films and observed a dependence of the film morphologies with their SCO properties. From below 15 growth cycles (<12 nm), there is a dramatic decrease in the cooperativity and the completeness of the transition, which coincides with a microstructural change in the films. The LbL growth process generates partially segregated crystallites surrounded by a matrix of Fe^{II} centres blocked in the HS state. Around the referred thickness threshold, these crystallites coalesce into a homogeneous film. Curiously, as the thickness gradually increases (one unit cell per growth cycle) the crystallite lateral size does not significantly change with the successive growth cycles. Thus, the thickness influence on the SCO properties cannot be attributed to a size effect, but to interparticle interactions, which enhances cooperativity and reduces the residual HS fraction.

We believe that these works represent an initial step on the necessary understanding of the SCO phenomenon at the ultrathin film limit, concomitant to the use of these materials on functional nanodevices. However, further joint work by the SCO and the MOF/CP research communities should follow in order to achieve this goal.

5. Integration of conductive MOFs and SCO CPs in functional devices

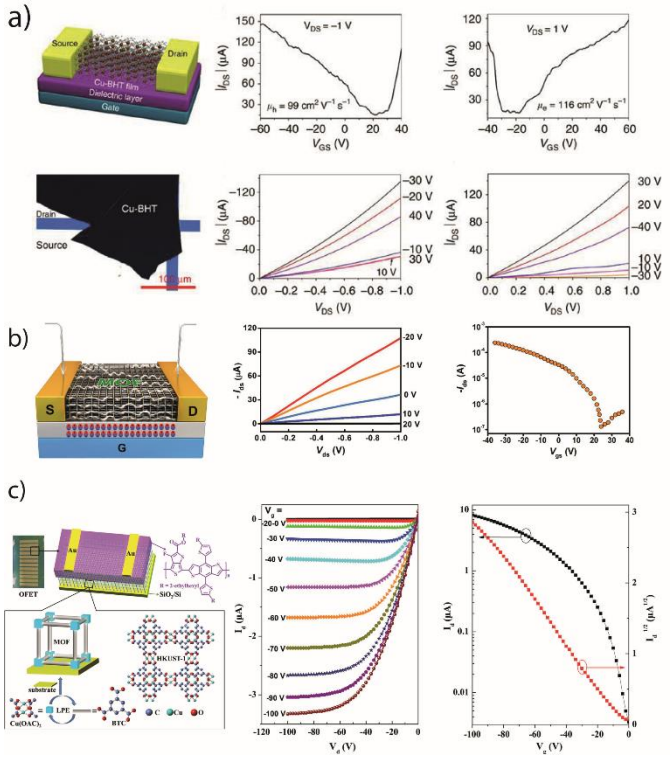

Figure 27. Selected examples of MOF-FETs. Schematic diagrams of device architectures for MOF-FET devices composed of Cu-BHT (a) or $Ni_3(HITP)_2$ (b) as active channels and HKUST-1 as bottom dielectric (c) along with output and transfer characteristics. a) Reproduced from ref. 131, licensed under CC BY 4.0, published by the Springer Nature.. b) Reproduced from ref. 425 with permission from American Chemical Society, copyright 2016. c) Reproduced from ref. 424 with permission from American Chemical Society, copyright 2017.

As previously mentioned, the path to integrate these molecular materials in functional devices is already being paved.[24,25,57,58] Two of the devices that have centered applications of conductive frameworks are FETs and chemical sensors whereas SCO has been almost exclusively used to transduce magnetic bistability into rectified mechanical, optical or electrical responses.

5.1 Field-effect transistors

FETs are three-terminal circuit elements that use electric fields to modulate the electrical behaviour of the device. A FET consists of a semiconductor or active channel, a dielectric and three conducting electrodes (gate, source and drain). Source and drain electrodes are connected to the semiconductor through ohmic contacts. The conductivity of the channel is a function of the potential applied across the gate and source terminals. In practical digital circuits they operate as logic gates. In electronics research, FETs are also a useful to characterize the electronic properties of semiconductors, as key parameters such as charge carrier mobilities and threshold voltages can be extracted from them. There are few examples of working FET devices where a CP or a MOF is the semiconductor (**Figure 27a-b**), and only one example of a MOF being used as a dielectric (**Figure 27c**).[424] For the first case, the first FET-MOF device ever reported was based on the In(III)-isophthalate MOF reported by Panda *et al.*[101] This MOFs showed conductivity through space with high charge carrier mobility (μ = 4.6·10^{-3} cm^2·V^{-1}·s^{-1} at V_G = -40 V). Long and co-workers prepared single crystal MOF-FETs of chemically reduced $K_xFe_2(BDP)_3$ (x = 0-2) and studied the hole and electron mobilities as a function of x. The mobilities increased with the progressive reduction until hitting a saturation for x = 1.[115] The remaining MOF-FETs are based on members of the highly conductive MOG family: Cu-BHT and $Ni_3(HITP)_2$. Both showed high charge carrier mobility values: 116 (electrons) and 99 (holes) cm^2·V^{-1}·s^{-1} for Cu-BHT[131] and 38-45.4 (hole) cm^2·V^{-1}·s^{-1} for $Ni_3(HITP)_2$.[425,426] Unfortunately, not all MOG-FET devices have performed well. Louie and co-workers prepared FET-type devices of Ni-HBA flakes with both top and bottom contacts that shows a slight current modulation with back gate voltage.[141] The same small modulation was also observed by Rubio-Giménez *et al.* in bottom-gated FET devices based on Cu-CAT-1 ultrathin films.[156]

5.2 Chemical sensors

Chemical sensors are electronic devices that transduce changes in analyte concentration into electrical signals. MOFs in general have very attractive features that have motivated researchers to use them as active materials in chemical sensors. As it has been described above, they are easily processable as ultrathin films with high surface-to-volume ratios, have intrinsic porosities to host possible analytes and their electronic and structural characteristics are easily tuneable through chemical modification. Hence, the topic of MOFs as sensors has been extensively reviewed in the literature during the past few years.[427–431] There are various types of MOF-sensors depending on the electronic property that is altered with analyte

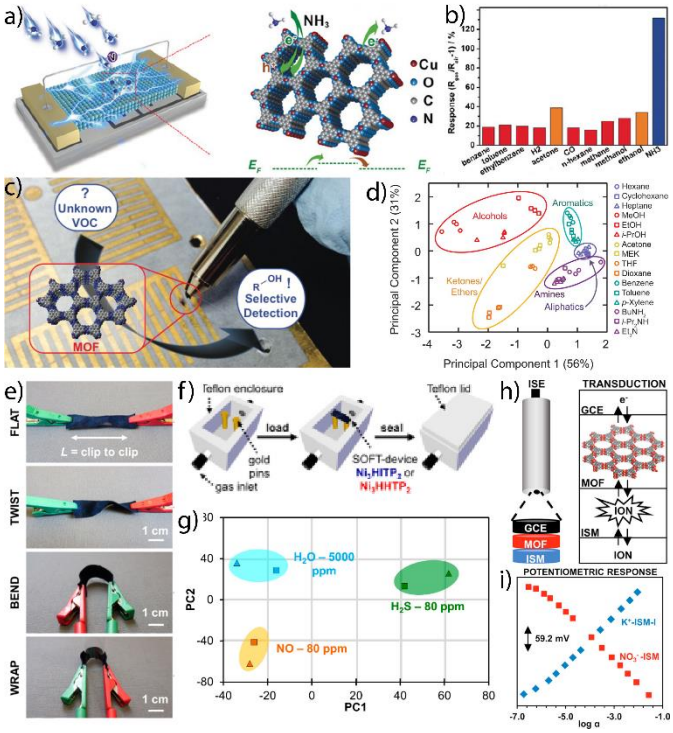

Figure 28. Examples of MOG chemical sensors. a) Scheme of a Cu-CAT-1 chemiresistive device and its possible mechanism for the detection of NH_3. b) Column chart showing the selective response of the Cu-CAT-1 device to NH_3. c) Scheme showing the fabrication of a chemiresistive sensor array solvent-free by mechanical "drawing" of MOG powders onto gold electrodes. d) Principal component analysis of the MOG sensor array responses to various VOCs. e) Photographs of flexible MOG textile sensing devices. f) Custom enclosure for dosing MOG textile sensing devices with analytes. g) Principle component analysis for MOG textile sensing devices showing capability for differentiating NO, H_2S, and H_2O. h) Scheme of the potentiometric ion sensing devices fabricated with the M-CAT-1 MOG family. i) Potentiometric response of the device to K^+ and NO_3^- ions. a-b) Reproduced from ref. 380 with permission from Wiley, copyright 2017. c-d) Reproduced from ref. 434 with permission from American Chemical Society, copyright 2015. e-g) Reproduced from ref. 437 with permission from American Chemical Society, copyright 2017. h-i) Reproduced from ref. 438 with permission from American Chemical Society, copyright 2018.

interaction: impedance, chemicapacitive, chemiresistive, Kelvin probe and FET sensors.[432] The simplest type of sensors are chemiresistors that react to the presence of analytes with changes in their electrical response. Thus, their response can be analysed by monitoring the direct current that flows through the active element at a constant biasing voltage. If the MOF is to act as the active element, chemiresistors require the use of conductive systems. MOGs are thus good candidates for chemiresistive sensors because of their high electrical conductivities comparable to conductive organic polymers and other 2D materials.[433] The first MOG to be integrated in a chemiresistive device was $Cu_3(HITP)_2$.[146] Dincă and co-workers fabricated a very simple device by drop casting an acetone suspension of $Cu_3(HITP)_2$ onto interdigitated gold electrodes and used it for the reversible chemiresistive sensing of ammonia vapour. Other MOGs chemiresistors soon followed (see **Figure 28**), further demonstrating their capability to detect selectively detect small concentrations of various volatile organic compounds (VOCs),[434] NH_3, [380,435] NO, H_2S and H_2O,[436,437] methanol[157] and even anions and cations (potentiometric detection).[438] However, most research efforts concentrated on sensing performance parameters such as sensitivity, stability and selectivity, whilst the mechanism behind the change in electrical response remained not well understood and host-guest interaction between MOFs and analytes have not been well characterized.[128] Recently, Rubio-Giménez *et al.* proposed a possible origin of this chemiresistive phenomenon in Cu-CAT-1, which lays in the bandgap modification due to the interaction of the Cu^{II} ions with gas analytes.[158]

There have also been significant advances to fabricate gas sensor using SCO MOFs. As reviewed beforehand, in porous Fe^{II}-HCPs the SCO phenomenon is very sensitive to the presence of guest molecules.[221,222] Therefore, a lot of these frameworks have shown potential as active elements in sensing devices. However only Bousseksou, Salmon and collaborators have fabricated an actual sensing device for VOC in which the sensing principle are changes in the SCO transition.[439] In order to do so, they deposited a patterned thin film of $Fe(bpac)[Pt(CN)_4]$ [bpac = bis(4-pyridyl)acetylene] using the previously described LbL technique and photolithography. Changes in the SCO due to the presence of the analytes were then optically detected via changes in the refractive index. The device could detect different aromatic VOC with a moderate sensitivity (few hundreds of ppm). We believe that advances in SCO sensors should progress towards current-based sensing devices. Detection of spin changes via electrical signals has faster dynamics and easier integration with current technology.

5.3 Switchable devices

Hitherto, there has been moderate success in developing functional nanodevices based on SCO MOFs and CPs. Apart from the nanostructuration issue discussed above, the SCO properties can be somewhat fragile in a device setting as they might be sensitive to the ambient conditions (e.g. humidity) or to successive switching cycles which might affect reproducibility. Nevertheless, SCO CPs have shown potential in temperature or pressure sensors, memory devices or mechanical actuators.

As detailed in the previous sections SCO materials show temperature and pressure dependence of their spin state, which translates in detectable through measurable physical such as their absorbance spectra or their refractive index. This has been used to fabricate temperature sensors based on photonic displays. For instance, Real, Gaspar, Levchenko and co-workers developed an optical pressure sensor based on the 3D Fe^{II}-HCP $[Fe(pz)Pt(CN)_4]$, in which small changes in the applied pressure could be correlated to the spin state ratio via an optical absorption band (**Figure 29a**).[440] As visible in **Figure 29b**, Lapresta-Fernández *et al.* used composites of $[Fe(NH_2\text{-}trz)_3](BF_4)$ and various organic polymers to fabricate thermochromic sensor arrays that macroscopically changed colours between white (HS state), pink, light pink and purple (LS state).[419,441] As discussed in section 3.2, SCO CPs have showed potential as electrical memory devices as well. However, a stable readable device has yet to be released, unlike in the case of discrete SCO complexes.[442,443]

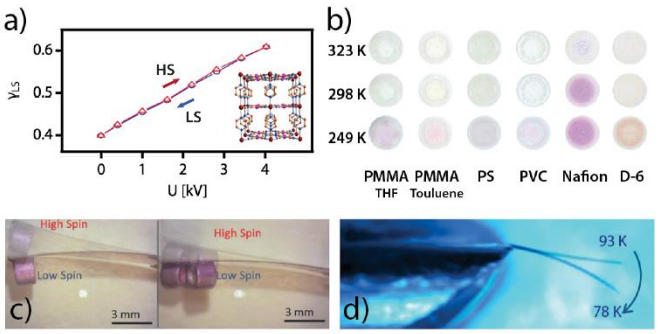

Figure 29. Examples of SCO switchable devices. a) Depende of the LS fraction of $[Fe(pz)Pt(CN)_4]$ with the potential applied to a piezoelement which translates it into pressure, measured at 293 K. b) Display of various $[Fe(NH_2\text{-}trz)_3](BF_4)$/polymer composites that change colour as a function of temperature. c) A cantilever of $[Fe(Htrz)_2(trz)](BF_4)$/polymer composite lifting some weight with the SCO-induced actuation. d) Comparison of the cantilever at 93 and 78 K, highlighting the SCO-induced actuation of $\{Fe(3\text{-}CNpy)[Au(CN)_2]_2\}\cdot 2/3H_2O$. a) Adapted from ref. 440 with permission from American Chemical Society, copyright 2019. b) Adapted from ref. 419 with permission from the Royal Society of Chemistry. c) Reproduced from ref. 445 with permission from Wiley, copyright 2018. d) Reproduced from ref. 444 with permission from Springer Nature, copyright 2013.

SCO CPs have also shown potential as mechanical actuators, as the spin transition also provokes a structural strain that can be translated into mechanical work. Bousseksou and co-workers have pioneered this application with various examples of organic polymer composites with embedded compounds of the 1D CP Fe^{II}-trz family (**Figure 29c**).[444–447] They also demonstrated this effect on single crystals of a 3D Fe^{II}-HCP (**Figure 29d**).[444] Interestingly, other authors have also showed the powerful effect of the SCO strain of $[Fe(Htrz)_2(trz)](BF_4)$[448] and $[Fe(pz)Pt(CN)_4]$[449] in the electrical conductivity of organic polymer composites.

6. Conclusions and future outlook

The combination in the toolbox provided by coordination chemistry and crystal engineering together with the versatility of molecular frameworks is a fruitful playground for the chemical design of materials that combine properties such as porosity, electrical conductivity and magnetic bistability, all relevant to the development of functional devices.

The works highlighted above confirm how the design principles required for endowing porous frameworks with electrical conductivity have boosted the development of multiple materials with fine control over charge transport. However, we are still missing a deeper physical understanding of mechanisms that control charge transport. This limitation is likely imposed by the synthetic difficulties in producing single crystals and the heterogeneity of polycrystalline solids and different methods of measurement, that are typically used. We are confident the next years will witness an increasing number of publications covering the physical mechanisms that control this phenomenon for a clearer understanding of anisotropic transport, charge mobility and carrier density, still required to bridge the gap of this field with organic electronics. Regarding the development of conductive SCO CPs, the field is still underdeveloped and holds great potential for further development. Current examples are limited to a handful of systems and the through-space and through-bond strategies that have deemed successful for producing conductive MOFs, are not so easy to implement without altering the electrostatic field of the magnetic centres and the SCO properties of the solid. We believe this challenge will be more easily attained by exploring other alternatives that do not involve changes in the metal-organic connectivity and ligand field splitting. Here, combination with conductive polymers or infiltration with redox-active guests might be helpful. Also, the use of mixed-valence systems exemplified by the family of Prussian Blue Analogues, constitutes a feasible way to implement higher electrical conductivities compatible with magnetic bistability.

Concerning the processing of these materials, the works above highlight the broad number of synthetic methods currently available to produce thin films with fine control over their thickness, coverage, roughness, orientation and crystallinity. These are an excellent starting point for their integration into solid-state devices but the effect of nanostructuration over their physical properties relevant to device function is often overlooked even though conductivity and SCO might be extremely sensitive to particle size reduction effects, pore surface coverage or heterogeneity at the nanoscale. This has not been a major problem for the development of a high number of FETs, sensors, actuators or switching devices that make use exclusively of electrical conductivity or spin transitions. However, the development of applications that exploit the combination of both properties at the atomic level as molecular junctions or spintronic devices are still limited by our poor understanding of the effects of nanostructuration or interface effects. We are confident this area holds great technological potential and we expect an increasing number of fundamental studies deepening into these physical aspects necessary for the integration of these materials into more sophisticated electronic devices.

Conflicts of interest

There are no conflicts to declare.

Acknowledgements

This work has been supported by the European Union (ERC Starting Grant Chem-fs-MOF 714122) and the Spanish Ministerio de Ciencia, Innovación y Universidades MICINN (Unit of Excellence María de Maeztu MDM-2015-0538, CTQ2017-83486-P and RTI2018-098568-A-I00). We thank Dr. Garin Escorcia-Ariza, Prof. Rob Ameloot, Prof. José Antonio Real and Prof. Eugenio Coronado for helpful discussions. S. T. thanks the Spanish MINECO for a Ramón y Cajal fellowship (RYC-2016-19817). V. R.-G. acknowledges the Research Foundation Flanders (FWO) for a Marie Skłodowska-Curie Actions – Seal of Excellence Postdoctoral Fellowship (196025/12Z6520N).

Notes and references

1 *Emerging Research Materials, International Roadmap for Devices and Systems*, Institute of Electrical and Electronics Engineers, Piscataway, New Jersey, USA, 2017.
2 *More Moore, International Roadmap for Devices and Systems*, Institute of Electrical and Electronics Engineers, Piscataway, New Jersey, USA, 2017.
3 H. Furukawa, K. E. Cordova, M. O'Keeffe and O. M. Yaghi, *Science*, 2013, **341**, 1230444.
4 W. Lu, Z. Wei, Z.-Y. Gu, T.-F. Liu, J. Park, J. Park, J. Tian, M. Zhang, Q. Zhang, T. Gentle III, M. Bosch and H.-C. Zhou, *Chem Soc Rev*, 2014, **43**, 5561–5593.
5 A. Schneemann, V. Bon, I. Schwedler, I. Senkovska, S. Kaskel and R. A. Fischer, *Chem Soc Rev*, 2014, **43**, 6062–6096.
6 N. C. Burtch, J. Heinen, T. D. Bennett, D. Dubbeldam and M. D. Allendorf, *Adv. Mater.*, 2018, **30**, 1704124.
7 B. F. Hoskins and R. Robson, *J Am Chem Soc*, 1990, **112**, 1546–1554.
8 H. Li, M. Eddaoudi, M. O'Keeffe and O. M. Yaghi, *Nature*, 1999, **402**, 276–279.
9 S. R. Batten, N. R. Champness, X.-M. Chen, J. Garcia-Martinez, S. Kitagawa, L. Öhrström, M. O'Keeffe, M. P. Suh and J. Reedijk, *Pure Appl Chem*, 2013, **85**, 1715–1724.
10 S. Kitagawa, R. Kitaura and S. Noro, *Angew Chem Int Ed*, 2004, **43**, 2334–2375.
11 M. D. Allendorf, M. E. Foster, F. Léonard, V. Stavila, P. L. Feng, F. P. Doty, K. Leong, E. Y. Ma, S. R. Johnston and A. A. Talin, *J Phys Chem Lett*, 2015, **6**, 1182–1195.
12 J. Liu, P. K. Thallapally, B. P. McGrail, D. R. Brown and J. Liu, *Chem Soc Rev*, 2012, **41**, 2308–2322.
13 M. P. Suh, H. J. Park, T. K. Prasad and D.-W. Lim, *Chem Rev*, 2012, **112**, 782–835.
14 K. Sumida, D. L. Rogow, J. A. Mason, T. M. McDonald, E. D. Bloch, Z. R. Herm, T.-H. Bae and J. R. Long, *Chem. Rev.*, 2012, **112**, 724–781.
15 H. Wu, Q. Gong, D. H. Olson and J. Li, *Chem Rev*, 2012, **112**, 836–868.
16 J. A. Mason, M. Veenstra and J. R. Long, *Chem Sci*, 2014, **5**, 32–51.
17 Y. He, W. Zhou, G. Qian and B. Chen, *Chem Soc Rev*, 2014, **43**, 5657–5678.
18 J.-R. Li, J. Sculley and H.-C. Zhou, *Chem Rev*, 2012, **112**, 869–932.
19 X. Zhao, Y. Wang, D.-S. Li, X. Bu and P. Feng, *Adv. Mater.*, 2018, **30**, 1705189.
20 J. Lee, O. K. Farha, J. Roberts, K. A. Scheidt, S. T. Nguyen and J. T. Hupp, *Chem Soc Rev*, 2009, **38**, 1450–1459.
21 A. Corma, H. García and F. X. Llabrés i Xamena, *Chem. Rev.*, 2010, **110**, 4606–4655.
22 M. Yoon, R. Srirambalaji and K. Kim, *Chem. Rev.*, 2012, **112**, 1196–1231.
23 P. Falcaro, R. Ricco, C. M. Doherty, K. Liang, A. J. Hill and M. J. Styles, *Chem Soc Rev*, 2014, **43**, 5513–5560.
24 V. Stavila, A. A. Talin and M. D. Allendorf, *Chem Soc Rev*, 2014, **43**, 5994–6010.
25 I. Stassen, N. Burtch, A. Talin, P. Falcaro, M. Allendorf and R. Ameloot, *Chem Soc Rev*, 2017, **46**, 3185–3241.
26 S. K. Bhardwaj, N. Bhardwaj, R. Kaur, J. Mehta, A. L. Sharma, K.-H. Kim and A. Deep, *J Mater Chem A*, 2018, **6**, 14992–15009.
27 M. Tran, K. Kline, Y. Qin, Y. Shen, M. D. Green and S. Tongay, *Appl. Phys. Rev.*, 2019, **6**, 041311.
28 J. Wu, J. Chen, C. Wang, Y. Zhou, K. Ba, H. Xu, W. Bao, X. Xu, A. Carlsson, S. Lazar, A. Meingast, Z. Sun and H. Deng, *Adv. Sci.*, 2020, **7**, 1903003.
29 G. Molnár, S. Rat, L. Salmon, W. Nicolazzi and A. Bousseksou, *Adv Mater*, 2018, **30**, 17003862.
30 J. W. Orton, *Semiconductors and the information revolution: magic crystals that made IT happen*, Academic Press, Amsterdam, The Netherlands, 2009.
31 G. Wegner, *Angew. Chem. Int. Ed. Engl.*, 1981, **20**, 361–381.
32 A. J. Heeger, *Angew. Chem. Int. Ed.*, 2001, **40**, 2591–2611.
33 A. G. MacDiarmid, *Angew. Chem. Int. Ed.*, 2001, **40**, 2581–2590.
34 V. Saxena and B. D. Malhotra, *Curr. Appl. Phys.*, 2003, **3**, 293–305.
35 A. K. Geim and K. S. Novoselov, *Nat. Mater.*, 2007, **6**, 183–191.
36 J. K. Wassei and R. B. Kaner, *Mater. Today*, 2010, **13**, 52–59.
37 X. Huang, Z. Yin, S. Wu, X. Qi, Q. He, Q. Zhang, Q. Yan, F. Boey and H. Zhang, *Small*, 2011, **7**, 1876–1902.
38 K. S. Novoselov, V. I. Fal'ko, L. Colombo, P. R. Gellert, M. G. Schwab and K. Kim, *Nature*, 2012, **490**, 192–200.
39 A. C. Ferrari, F. Bonaccorso, V. Fal'ko, K. S. Novoselov, S. Roche, P. Bøggild, S. Borini, F. H. L. Koppens, V. Palermo, N. Pugno, J. A. Garrido, R. Sordan, A. Bianco, L. Ballerini, M. Prato, E. Lidorikis, J. Kivioja, C. Marinelli, T. Ryhänen, A. Morpurgo, J. N. Coleman, V. Nicolosi, L. Colombo, A. Fert, M. Garcia-Hernandez, A. Bachtold, G. F. Schneider, F. Guinea, C. Dekker, M. Barbone, Z. Sun, C. Galiotis, A. N. Grigorenko, G. Konstantatos, A. Kis, M. Katsnelson, L. Vandersypen, A. Loiseau, V. Morandi, D. Neumaier, E. Treossi, V. Pellegrini, M. Polini, A. Tredicucci, G. M. Williams, B. Hee Hong, J.-H. Ahn, J. Min Kim, H. Zirath, B. J. van Wees, H. van der Zant, L. Occhipinti, A. Di Matteo, I. A. Kinloch, T. Seyller, E. Quesnel, X. Feng, K. Teo, N. Rupesinghe, P. Hakonen, S. R. T. Neil, Q. Tannock, T. Löfwander and J. Kinaret, *Nanoscale*, 2015, **7**, 4598–4810.
40 T. W. Ebbesen, H. J. Lezec, H. Hiura, J. W. Bennett, H. F. Ghaemi and T. Thio, *Nature*, 1996, **382**, 54–56.
41 Z. Wu, Z. Chen, X. Du, J. M. Logan, J. Sippel, M. Nikolou, K. Kamaras, J. R. Reynolds, D. B. Tanner, A. F. Hebard and A. G. Rinzler, *Science*, 2004, **305**, 1273–1276.
42 C. Biswas and Y. H. Lee, *Adv. Funct. Mater.*, 2011, **21**, 3806–3826.
43 S. Park, M. Vosguerichian and Z. Bao, *Nanoscale*, 2013, **5**, 1727–1752.
44 G. Givaja, P. Amo-Ochoa, C. J. Gomez-Garcia and F. Zamora, *Chem Soc Rev*, 2012, **41**, 115–147.
45 R. Murase, B. Ding, Q. Gu and D. M. D'Alessandro, *Philos. Trans. R. Soc. Math. Phys. Eng. Sci.*, 2019, **377**, 20180226.
46 W. Zhang, J. Chu and M. Hu, *Chem. – Asian J.*, 2020, **15**, 1202–1213.
47 L. Sun, M. G. Campbell and M. Dincă, *Angew Chem Int Ed*, 2016, **55**, 3566–3579.
48 C. F. Leong, P. M. Usov and D. M. D'Alessandro, *MRS Bull.*, 2016, **41**, 858–864.
49 D. D. Medina, A. Mähringer and T. Bein, *Isr. J. Chem.*, 2018, **58**, 1089–1101.
50 P. Li and B. Wang, *Isr. J. Chem.*, 2018, **58**, 1010–1018.
51 C.-W. Kung, P.-C. Han, C.-H. Chuang and K. C.-W. Wu, *APL Mater.*, 2019, **7**, 110902.
52 X. Deng, J.-Y. Hu, J. Luo, W.-M. Liao and J. He, *Top. Curr. Chem.*, 2020, **378**, 27.
53 W.-H. Li, W.-H. Deng, G.-E. Wang and G. Xu, *EnergyChem*, 2020, **2**, 100029.

54 L. S. Xie, G. Skorupskii and M. Dincă, *Chem. Rev.*, , DOI:10.1021/acs.chemrev.9b00766.
55 J. J. Calvo, S. M. Angel and M. C. So, *APL Mater.*, 2020, **8**, 050901.
56 J. Rocha, M. Souto, K. Strutyński and M. Melle-Franco, *Chem. – Eur. J.*, , DOI:10.1002/chem.202001211.
57 M. D. Allendorf, A. Schwartzberg, V. Stavila and A. A. Talin, *Chem Eur J*, 2011, **17**, 11372–11388.
58 M. Usman, S. Mendiratta and K.-L. Lu, *Adv Mater*, 2017, **29**, 1605071.
59 S. Han, S. C. Warren, S. M. Yoon, C. D. Malliakas, X. Hou, Y. Wei, M. G. Kanatzidis and B. A. Grzybowski, *J Am Chem Soc*, 2015, **137**, 8169–8175.
60 C.-W. Kung, A. E. Platero-Prats, R. J. Drout, J. Kang, T. C. Wang, C. O. Audu, M. C. Hersam, K. W. Chapman, O. K. Farha and J. T. Hupp, *ACS Appl Mater Interfaces*, 2018, **10**, 30532–30540.
61 C.-W. Kung, K. Otake, C. T. Buru, S. Goswami, Y. Cui, J. T. Hupp, A. M. Spokoyny and O. K. Farha, *J. Am. Chem. Soc.*, 2018, **140**, 3871–3875.
62 B. Dhara, S. S. Nagarkar, J. Kumar, V. Kumar, P. K. Jha, S. K. Ghosh, S. Nair and N. Ballav, *J Phys Chem Lett*, 2016, **7**, 2945–2950.
63 B. Le Ouay, M. Boudot, T. Kitao, T. Yanagida, S. Kitagawa and T. Uemura, *J Am Chem Soc*, 2016, **138**, 10088–10091.
64 T. C. Wang, I. Hod, C. O. Audu, N. A. Vermeulen, S. T. Nguyen, O. K. Farha and J. T. Hupp, *ACS Appl Mater Interfaces*, 2017, **9**, 12584–12591.
65 A. Nuñez-Lopez, M. Galbiati, N. M. Padial, C. R. Ganivet, S. Tatay, E. Pardo, D. Armentano and C. Martí-Gastaldo, *Angew Chem Int Ed*, 2019, **58**, 9179–9183.
66 A. Jadhav, K. Gupta, P. Ninawe and N. Ballav, *Angew. Chem. Int. Ed.*, 2020, **59**, 2215–2219.
67 M.-H. Zeng, Q.-X. Wang, Y.-X. Tan, S. Hu, H.-X. Zhao, L.-S. Long and M. Kurmoo, *J Am Chem Soc*, 2010, **132**, 2561–2563.
68 D. Y. Lee, D. V. Shinde, S. J. Yoon, K. N. Cho, W. Lee, N. K. Shrestha and S.-H. Han, *J Phys Chem C*, 2014, **118**, 16328–16334.
69 D. Y. Lee, E.-K. Kim, N. K. Shrestha, D. W. Boukhvalov, J. K. Lee and S.-H. Han, *ACS Appl Mater Interfaces*, 2015, **7**, 18501–18507.
70 D. Y. Lee, I. Lim, C. Y. Shin, S. A. Patil, W. Lee, N. K. Shrestha, J. K. Lee and S.-H. Han, *J Mater Chem A*, 2015, **3**, 22669–22676.
71 G.-P. Li, K. Zhang, H.-Y. Zhao, L. Hou and Y.-Y. Wang, *ChemPlusChem*, 2017, **82**, 716–720.
72 L. Pan, G. Liu, W. Shi, J. Shang, W. R. Leow, Y. Liu, Y. Jiang, S. Li, X. Chen and R.-W. Li, *Nat Commun*, 2018, **9**, 3813.
73 W. Hai-Ying, G. Jing-Yuan, H. Carol, J. Cheng-Qi, W. Yue, L. C. F, D. D. M, L. Tao and Z. Jing-Lin, *Angew Chem Int Ed*, 2017, **56**, 5465–5470.
74 C. F. Leong, C.-H. Wang, C. D. Ling and D. M. D'Alessandro, *Polyhedron*, 2018, **154**, 334–342.
75 J. Su, T.-H. Hu, R. Murase, H.-Y. Wang, D. M. D'Alessandro, M. Kurmoo and J.-L. Zuo, *Inorg. Chem.*, 2019, **58**, 3698–3706.
76 Z. Hao, G. Yang, X. Song, M. Zhu, X. Meng, S. Zhao, S. Song and H. Zhang, *J Mater Chem A*, 2014, **2**, 237–244.
77 Y.-Q. Hu, M.-Q. Li, Y. Wang, T. Zhang, P.-Q. Liao, Z. Zheng, X.-M. Chen and Y.-Z. Zheng, *Chem. – Eur. J.*, 2017, **23**, 8409–8413.
78 X. Zhang, I. da Silva, R. Fazzi, A. M. Sheveleva, X. Han, B. F. Spencer, S. A. Sapchenko, F. Tuna, E. J. L. McInnes, M. Li, S. Yang and M. Schröder, *Inorg. Chem.*, 2019, **58**, 14145–14150.
79 Z. Yin, Q.-X. Wang and M.-H. Zeng, *J Am Chem Soc*, 2012, **134**, 4857–4863.
80 A. A. Talin, A. Centrone, A. C. Ford, M. E. Foster, V. Stavila, P. Haney, R. A. Kinney, V. Szalai, F. El Gabaly, H. P. Yoon, F. Léonard and M. D. Allendorf, *Science*, 2014, **343**, 66.
81 T. Neumann, J. Liu, T. Wächter, P. Friederich, F. Symalla, A. Welle, V. Mugnaini, V. Meded, M. Zharnikov, C. Wöll and W. Wenzel, *ACS Nano*, 2016, **10**, 7085–7093.
82 A. Sengupta, S. Datta, C. Su, T. S. Herng, J. Ding, J. J. Vittal and K. P. Loh, *ACS Appl Mater Interfaces*, 2016, **8**, 16154–16159.
83 A. Dragasser, O. Shekhah, O. Zybaylo, C. Shen, M. Buck, C. Woll and D. Schlettwein, *Chem Commun*, 2012, **48**, 663–665.
84 J. Liu, T. Wächter, A. Irmler, P. G. Weidler, H. Gliemann, F. Pauly, V. Mugnaini, M. Zharnikov and C. Wöll, *ACS Appl. Mater. Interfaces*, 2015, **7**, 9824–9830.
85 Z. Guo, D. K. Panda, K. Maity, D. Lindsey, T. G. Parker, T. E. Albrecht-Schmitt, J. L. Barreda-Esparza, P. Xiong, W. Zhou and S. Saha, *J Mater Chem C*, 2016, **4**, 894–899.
86 S. Goswami, D. Ray, K. Otake, C.-W. Kung, S. J. Garibay, T. Islamoglu, A. Atilgan, Y. Cui, C. J. Cramer, O. K. Farha and J. T. Hupp, *Chem Sci*, 2018, **9**, 4477–4482.
87 M. Souto, J. Calbo, S. Mañas-Valero, A. Walsh and G. Mínguez Espallargas, *Beilstein J. Nanotechnol.*, 2019, **10**, 1883–1893.
88 S. Dalgleish and N. Robertson, *Dithiolenes Non-Innocent Redox-Act. Ligands*, 2010, **254**, 1549–1558.
89 C. Rovira, *Chem. Rev.*, 2004, **104**, 5289–5318.
90 M. Iyoda, M. Hasegawa and Y. Miyake, *Chem. Rev.*, 2004, **104**, 5085–5114.
91 P. Frère and P. J. Skabara, *Chem Soc Rev*, 2005, **34**, 69–98.
92 H.-Y. Wang, L. Cui, J.-Z. Xie, C. F. Leong, D. M. D'Alessandro and J.-L. Zuo, *Coord Chem Rev*, 2017, **345**, 342–361.
93 C. Jia, D. Zhang, C.-M. Liu, W. Xu, H. Hu and D. Zhu, *New J Chem*, 2002, **26**, 490–494.
94 Y. Ding, Q. Chen, J.-C. Zhong, M. Munakata, H. Konaka, G.-L. Ning and H.-Z. Wang, *Polyhedron*, 2008, **27**, 1393–1400.
95 T. L. A. Nguyen, R. Demir-Cakan, T. Devic, M. Morcrette, T. Ahnfeldt, P. Auban-Senzier, N. Stock, A.-M. Goncalves, Y. Filinchuk, J.-M. Tarascon and G. Férey, *Inorg Chem*, 2010, **49**, 7135–7143.
96 T. C. Narayan, T. Miyakai, S. Seki and M. Dincă, *J Am Chem Soc*, 2012, **134**, 12932–12935.
97 S. S. Park, E. R. Hontz, L. Sun, C. H. Hendon, A. Walsh, T. V. Voorhis and M. Dincă, *J Am Chem Soc*, 2015, **137**, 1774–1777.
98 L. S. Xie and M. Dincă, *Isr J Chem*, 2018, **58**, 1119–1122.
99 J. Su, S. Yuan, H.-Y. Wang, L. Huang, J.-Y. Ge, E. Joseph, J. Qin, T. Cagin, J.-L. Zuo and H.-C. Zhou, *Nat Commun*, 2017, **8**, 2008.
100 S. S. Park, C. H. Hendon, A. J. Fielding, A. Walsh, M. O'Keeffe and M. Dincă, *J. Am. Chem. Soc.*, 2017, **139**, 3619–3622.
101 T. Panda and R. Banerjee, *Proc. Natl. Acad. Sci. India Sect. Phys. Sci.*, 2014, **84**, 331–336.
102 D. Chen, H. Xing, Z. Su and C. Wang, *Chem Commun*, 2016, **52**, 2019–2022.
103 P. I. Scheurle, A. Mähringer, A. C. Jakowetz, P. Hosseini, A. F. Richter, G. Wittstock, D. D. Medina and T. Bein, *Nanoscale*, 2019, **11**, 20949–20955.
104 C. Hua, P. W. Doheny, B. Ding, B. Chan, M. Yu, C. J. Kepert and D. M. D'Alessandro, *J Am Chem Soc*, 2018, **140**, 6622–6630.
105 L. Qu, H. Iguchi, S. Takaishi, F. Habib, C. F. Leong, D. M. D'Alessandro, T. Yoshida, H. Abe, E. Nishibori and M. Yamashita, *J. Am. Chem. Soc.*, 2019, **141**, 6802–6806.
106 H. C. Wentz, G. Skorupskii, A. B. Bonfim, J. L. Mancuso, C. H. Hendon, E. H. Oriel, G. T. Sazama and M. G. Campbell, *Chem Sci*, 2020, **11**, 1342–1346.
107 R. Murase, C. F. Leong and D. M. D'Alessandro, *Inorg Chem*, 2017, **56**, 14373–14382.

108 Y. Takazaki, Z. Yang, M. Ebihara, K. Inoue and T. Kawamura, *Chem Lett*, 2003, **32**, 120–121.
109 P. Amo-Ochoa, L. Welte, R. González-Prieto, P. J. Sanz Miguel, C. J. Gómez-García, E. Mateo-Martí, S. Delgado, J. Gómez-Herrero and F. Zamora, *Chem Commun*, 2010, **46**, 3262–3264.
110 J. N. Behera, D. M. D'Alessandro, N. Soheilnia and J. R. Long, *Chem Mater*, 2009, **21**, 1922–1926.
111 W.-J. Li, C. Han, G. Cheng, S.-L. Chou, H.-K. Liu and S.-X. Dou, *Small*, 2019, **15**, 1900470.
112 F. Gándara, F. J. Uribe-Romo, D. K. Britt, H. Furukawa, L. Lei, R. Cheng, X. Duan, M. O'Keeffe and O. M. Yaghi, *Chem Eur J*, 2012, **18**, 10595–10601.
113 J. G. Park, M. L. Aubrey, J. Oktawiec, K. Chakarawet, L. E. Darago, F. Grandjean, G. J. Long and J. R. Long, *J Am Chem Soc*, 2018, **140**, 8526–8534.
114 L. S. Xie, L. Sun, R. Wan, S. S. Park, J. A. DeGayner, C. H. Hendon and M. Dincă, *J Am Chem Soc*, 2018, **140**, 7411–7414.
115 M. L. Aubrey, B. M. Wiers, S. C. Andrews, T. Sakurai, S. E. Reyes-Lillo, S. M. Hamed, C.-J. Yu, L. E. Darago, J. A. Mason, J.-O. Baeg, F. Grandjean, G. J. Long, S. Seki, J. B. Neaton, P. Yang and J. R. Long, *Nat Mater*, 2018, **17**, 625–632.
116 S. Goswami, I. Hod, J. D. Duan, C.-W. Kung, M. Rimoldi, C. D. Malliakas, R. H. Palmer, O. K. Farha and J. T. Hupp, *J. Am. Chem. Soc.*, 2019, **141**, 17696–17702.
117 S. Huh, S.-J. Kim and Y. Kim, *CrystEngComm*, 2016, **18**, 345–368.
118 S. R. Ahrenholtz, C. C. Epley and A. J. Morris, *J Am Chem Soc*, 2014, **136**, 2464–2472.
119 L. E. Darago, M. L. Aubrey, C. J. Yu, M. I. Gonzalez and J. R. Long, *J. Am. Chem. Soc.*, 2015, **137**, 15703–15711.
120 J. A. DeGayner, I.-R. Jeon, L. Sun, M. Dincă and T. D. Harris, *J Am Chem Soc*, 2017, **139**, 4175–4184.
121 A. Bhattacharjee, D. Bhakat, M. Roy and J. Kusz, *Phys. B Condens. Matter*, 2010, **405**, 1546–1550.
122 S. Benmansour, A. Abhervé, P. Gómez-Claramunt, C. Vallés-García and C. J. Gómez-García, *ACS Appl Mater Interfaces*, 2017, **9**, 26210–26218.
123 S. A. Sahadevan, A. Abhervé, N. Monni, C. Sáenz de Pipaón, J. R. Galán-Mascarós, J. C. Waerenborgh, B. J. C. Vieira, P. Auban-Senzier, S. Pillet, E.-E. Bendeif, P. Alemany, E. Canadell, M. L. Mercuri and N. Avarvari, *J Am Chem Soc*, 2018, **140**, 12611–12621.
124 L. Liu, J. A. DeGayner, L. Sun, D. Z. Zee and T. D. Harris, *Chem Sci*, 2019, **10**, 4652–4661.
125 K. S. Pedersen, P. Perlepe, M. L. Aubrey, D. N. Woodruff, S. E. Reyes-Lillo, A. Reinholdt, L. Voigt, Z. Li, K. Borup, M. Rouzières, D. Samohvalov, F. Wilhelm, A. Rogalev, J. B. Neaton, J. R. Long and R. Clérac, *Nat Chem*, 2018, **10**, 1056–1061.
126 K.-H. Low, V. A. L. Roy, S. S.-Y. Chui, S. L.-F. Chan and C.-M. Che, *Chem Commun*, 2010, **46**, 7328–7330.
127 L. Sun, C. H. Hendon, M. A. Minier, A. Walsh and M. Dincă, *J Am Chem Soc*, 2015, **137**, 6164–6167.
128 M. Ko, L. Mendecki and K. A. Mirica, *Chem Commun*, 2018, **54**, 7873–7891.
129 D. Sheberla, L. Sun, M. A. Blood-Forsythe, S. Er, C. R. Wade, C. K. Brozek, A. Aspuru-Guzik and M. Dincă, *J Am Chem Soc*, 2014, **136**, 8859–8862.
130 M. Hmadeh, Z. Lu, Z. Liu, F. Gándara, H. Furukawa, S. Wan, V. Augustyn, R. Chang, L. Liao, F. Zhou, E. Perre, V. Ozolins, K. Suenaga, X. Duan, B. Dunn, Y. Yamamto, O. Terasaki and O. M. Yaghi, *Chem Mater*, 2012, **24**, 3511–3513.
131 X. Huang, P. Sheng, Z. Tu, F. Zhang, J. Wang, H. Geng, Y. Zou, C. Di, Y. Yi, Y. Sun, W. Xu and D. Zhu, *Nat Commun*, 2015, **6**, 7408.
132 Y. Cui, J. Yan, Z. Chen, J. Zhang, Y. Zou, Y. Sun, W. Xu and D. Zhu, *Adv Sci*, 2019, **6**, 1802235.
133 X. Huang, H. Li, Z. Tu, L. Liu, X. Wu, J. Chen, Y. Liang, Y. Zou, Y. Yi, J. Sun, W. Xu and D. Zhu, *J Am Chem Soc*, 2018, **140**, 15153–15156.
134 D. L. Turner, T. P. Vaid, P. W. Stephens, K. H. Stone, A. G. DiPasquale and A. L. Rheingold, *J. Am. Chem. Soc.*, 2008, **130**, 14–15.
135 T. Kambe, R. Sakamoto, K. Hoshiko, K. Takada, M. Miyachi, J.-H. Ryu, S. Sasaki, J. Kim, K. Nakazato, M. Takata and H. Nishihara, *J Am Chem Soc*, 2013, **135**, 2462–2465.
136 A. J. Clough, J. W. Yoo, M. H. Mecklenburg and S. C. Marinescu, *J Am Chem Soc*, 2015, **137**, 118–121.
137 T. Pal, T. Kambe, T. Kusamoto, M. L. Foo, R. Matsuoka, R. Sakamoto and H. Nishihara, *ChemPlusChem*, 2015, **80**, 1255–1258.
138 T. Pal, S. Doi, H. Maeda, K. Wada, C. M. Tan, N. Fukui, R. Sakamoto, S. Tsuneyuki, S. Sasaki and H. Nishihara, *Chem Sci*, 2019, **10**, 5218–5225.
139 X. Sun, K.-H. Wu, R. Sakamoto, T. Kusamoto, H. Maeda and H. Nishihara, *Chem Lett*, 2017, **46**, 1072–1075.
140 X. Sun, K.-H. Wu, R. Sakamoto, T. Kusamoto, H. Maeda, X. Ni, W. Jiang, F. Liu, S. Sasaki, H. Masunaga and H. Nishihara, *Chem Sci*, 2017, **8**, 8078–8085.
141 N. Lahiri, N. Lotfizadeh, R. Tsuchikawa, V. V. Deshpande and J. Louie, *J Am Chem Soc*, 2017, **139**, 19–22.
142 J.-H. Dou, L. Sun, Y. Ge, W. Li, C. H. Hendon, J. Li, S. Gul, J. Yano, E. A. Stach and M. Dincă, *J Am Chem Soc*, 2017, **139**, 13608–13611.
143 J. Park, M. Lee, D. Feng, Z. Huang, A. C. Hinckley, A. Yakovenko, X. Zou, Y. Cui and Z. Bao, *J Am Chem Soc*, 2018, **140**, 10315–10323.
144 J. Park, A. C. Hinckley, Z. Huang, D. Feng, A. A. Yakovenko, M. Lee, S. Chen, X. Zou and Z. Bao, *J Am Chem Soc*, 2018, **140**, 14533–14537.
145 X. Huang, S. Zhang, L. Liu, L. Yu, G. Chen, W. Xu and D. Zhu, *Angew Chem Int Ed*, 2018, **57**, 146–150.
146 M. G. Campbell, D. Sheberla, S. F. Liu, T. M. Swager and M. Dincă, *Angew Chem Int Ed*, 2015, **54**, 4349–4352.
147 D. Renhao, Z. Zhikun, T. D. C, Z. Jian, C. Naisa, L. Shaohua, Z. Xiaodong, S. Gotthard and F. Xinliang, *Chem Eur J*, 2017, **23**, 2255–2260.
148 Y. Cui, J. Yan, Z. Chen, W. Xing, C. Ye, X. Li, Y. Zou, Y. Sun, C. Liu, W. Xu and D. Zhu, *iScience*, , DOI:10.1016/j.isci.2019.100812.
149 A. J. Clough, J. M. Skelton, C. A. Downes, A. A. de la Rosa, J. W. Yoo, A. Walsh, B. C. Melot and S. C. Marinescu, *J Am Chem Soc*, 2017, **139**, 10863–10867.
150 R. Dong, M. Pfeffermann, H. Liang, Z. Zheng, X. Zhu, J. Zhang and X. Feng, *Angew Chem Int Ed*, 2015, **54**, 12058–12063.
151 L. Mendecki, M. Ko, X. Zhang, Z. Meng and K. A. Mirica, *J Am Chem Soc*, 2017, **139**, 17229–17232.
152 J. Cui and Z. Xu, *Chem Commun*, 2014, **50**, 3986–3988.
153 R. W. Day, D. K. Bediako, M. Rezaee, L. R. Parent, G. Skorupskii, M. Q. Arguilla, C. H. Hendon, I. Stassen, N. C. Gianneschi, P. Kim and M. Dincă, *ACS Cent. Sci.*, 2019, **5**, 1959–1964.
154 J. Huang, Y. He, M.-S. Yao, J. He, G. Xu, M. Zeller and Z. Xu, *J Mater Chem A*, 2017, **5**, 16139–16143.
155 W.-H. Li, K. Ding, H.-R. Tian, M.-S. Yao, B. Nath, W.-H. Deng, Y. Wang and G. Xu, *Adv Funct Mater*, 2017, **27**, 1702067.
156 V. Rubio-Giménez, M. Galbiati, J. Castells-Gil, N. Almora-Barrios, J. Navarro-Sánchez, G. Escorcia-Ariza, M. Mattera, T. Arnold, J. Rawle, S. Tatay, E. Coronado and C. Martí-Gastaldo, *Adv. Mater.*, 2018, **30**, 1704291.

157 B. Hoppe, K. D. J. Hindricks, D. P. Warwas, H. A. Schulze, A. Mohmeyer, T. J. Pinkvos, S. Zailskas, M. R. Krey, C. Belke, S. König, M. Fröba, R. J. Haug and P. Behrens, *CrystEngComm*, 2018, **20**, 6458–6471.

158 V. Rubio-Giménez, N. Almora-Barrios, G. Escorcia-Ariza, M. Galbiati, M. Sessolo, S. Tatay and C. Martí-Gastaldo, *Angew Chem Int Ed*, 2018, **57**, 15086–15090.

159 G. Skorupskii, B. A. Trump, T. W. Kasel, C. M. Brown, C. H. Hendon and M. Dincă, *Nat. Chem.*, 2020, **12**, 131–136.

160 X. Song, X. Wang, Y. Li, C. Zheng, B. Zhang, C. Di, F. Li, C. Jin, W. Mi, L. Chen and W. Hu, *Angew. Chem. Int. Ed.*, 2020, **59**, 1118–1123.

161 M.-S. Yao, J.-J. Zheng, A.-Q. Wu, G. Xu, S. S. Nagarkar, G. Zhang, M. Tsujimoto, S. Sakaki, S. Horike, K. Otake and S. Kitagawa, *Angew. Chem. Int. Ed.*, 2020, **59**, 172–176.

162 Y. Jiang, I. Oh, S. H. Joo, O. Buyukcakir, X. Chen, S. H. Lee, M. Huang, W. K. Seong, S. K. Kwak, J.-W. Yoo and R. S. Ruoff, *J. Am. Chem. Soc.*, 2019, **141**, 16884–16893.

163 M. Ko, A. Aykanat, M. K. Smith and K. A. Mirica, *Sensors*, 2017, **17**, 2192.

164 D. Sheberla, J. C. Bachman, J. S. Elias, C.-J. Sun, Y. Shao-Horn and M. Dinca, *Nat Mater*, 2017, **16**, 220–224.

165 L.-P. Tang, L.-M. Tang, H. Geng, Y.-P. Yi, Z. Wei, K.-Q. Chen and H.-X. Deng, *Appl Phys Lett*, 2018, **112**, 012101.

166 S. Chen, J. Dai and X. C. Zeng, *Phys Chem Chem Phys*, 2015, **17**, 5954–5958.

167 M. E. Foster, K. Sohlberg, M. D. Allendorf and A. A. Talin, *J. Phys. Chem. Lett.*, 2018, **9**, 481–486.

168 L. Sun, S. S. Park, D. Sheberla and M. Dincă, *J. Am. Chem. Soc.*, 2016, **138**, 14772–14782.

169 T. Kambe, R. Sakamoto, T. Kusamoto, T. Pal, N. Fukui, K. Hoshiko, T. Shimojima, Z. Wang, T. Hirahara, K. Ishizaka, S. Hasegawa, F. Liu and H. Nishihara, *J Am Chem Soc*, 2014, **136**, 14357–14360.

170 M. E. Foster, K. Sohlberg, C. D. Spataru and M. D. Allendorf, *J Phys Chem C*, 2016, **120**, 15001–15008.

171 R. Dong, P. Han, H. Arora, M. Ballabio, M. Karakus, Z. Zhang, C. Shekhar, P. Adler, P. St. Petkov, A. Erbe, S. C. B. Mannsfeld, C. Felser, T. Heine, M. Bonn, X. Feng and E. Cánovas, *Nat Mater*, 2018, **17**, 1027–1032.

172 H. Arora, R. Dong, T. Venanzi, J. Zscharschuch, H. Schneider, M. Helm, X. Feng, E. Cánovas and A. Erbe, *Adv. Mater.*, 2020, **32**, 1907063.

173 R. Dong, M. Pfeffermann, D. Skidin, F. Wang, Y. Fu, A. Narita, M. Tommasini, F. Moresco, G. Cuniberti, R. Berger, K. Müllen and X. Feng, *J Am Chem Soc*, 2017, **139**, 2168–2171.

174 R. Dong, Z. Zhang, D. C. Tranca, S. Zhou, M. Wang, P. Adler, Z. Liao, F. Liu, Y. Sun, W. Shi, Z. Zhang, E. Zschech, S. C. B. Mannsfeld, C. Felser and X. Feng, *Nat Commun*, 2018, **9**, 2637.

175 Q. Zhao, S.-H. Li, R.-L. Chai, X. Ren and C. Zhang, *ACS Appl. Mater. Interfaces*, 2020, **12**, 7504–7509.

176 J. Liu, Y. Zhou, Z. Xie, Y. Li, Y. Liu, J. Sun, Y. Ma, O. Terasaki and L. Chen, *Angew. Chem. Int. Ed.*, 2020, **59**, 1081–1086.

177 H. Jia, Y. Yao, J. Zhao, Y. Gao, Z. Luo and P. Du, *J Mater Chem A*, 2018, **6**, 1188–1195.

178 N. Hisanori, Y. Nobuhiro, Y. Teppei, S. Kanji and K. Nobuo, *Chem Eur J*, 2018, **24**, 1806–1810.

179 C. Yang, R. Dong, M. Wang, P. St. Petkov, Z. Zhang, M. Wang, P. Han, M. Ballabio, S. A. Bräuninger, Z. Liao, J. Zhang, F. Schwotzer, E. Zschech, H.-H. Klauss, E. Cánovas, S. Kaskel, M. Bonn, S. Zhou, T. Heine and X. Feng, *Nat. Commun.*, 2019, **10**, 3260.

180 Z. Meng, A. Aykanat and K. A. Mirica, *J Am Chem Soc*, 2019, **141**, 2046–2053.

181 H. Zhong, K. H. Ly, M. Wang, Y. Krupskaya, X. Han, J. Zhang, J. Zhang, V. Kataev, B. Büchner, I. M. Weidinger, S. Kaskel, P. Liu, M. Chen, R. Dong and X. Feng, *Angew. Chem. Int. Ed.*, 2019, **58**, 10677–10682.

182 F. Wang, Z. Liu, C. Yang, H. Zhong, G. Nam, P. Zhang, R. Dong, Y. Wu, J. Cho, J. Zhang and X. Feng, *Adv. Mater.*, 2020, **32**, 1905361.

183 J. Dong, X. Han, Y. Liu, H. Li and Y. Cui, *Angew. Chem. Int. Ed.*, , DOI:10.1002/anie.202004796.

184 Z. Meng, R. M. Stolz and K. A. Mirica, *J. Am. Chem. Soc.*, 2019, **141**, 11929–11937.

185 M. Wang, M. Ballabio, M. Wang, H.-H. Lin, B. P. Biswal, X. Han, S. Paasch, E. Brunner, P. Liu, M. Chen, M. Bonn, T. Heine, S. Zhou, E. Cánovas, R. Dong and X. Feng, *J. Am. Chem. Soc.*, 2019, **141**, 16810–16816.

186 T. Li, W.-D. Zhang, Y. Liu, Y. Li, C. Cheng, H. Zhu, X. Yan, Z. Li and Z.-G. Gu, *J Mater Chem A*, 2019, **7**, 19676–19681.

187 A. Mähringer, A. C. Jakowetz, J. M. Rotter, B. J. Bohn, J. K. Stolarczyk, J. Feldmann, T. Bein and D. D. Medina, *ACS Nano*, 2019, **13**, 6711–6719.

188 X. Du, J. Zhang, H. Wang, Z. Huang, A. Guo, L. Zhao, Y. Niu, X. Li, B. Wu and Y. Liu, *Mater Chem Front*, 2020, **4**, 243–251.

189 L. Sun, B. Liao, D. Sheberla, D. Kraemer, J. Zhou, E. A. Stach, D. Zakharov, V. Stavila, A. A. Talin, Y. Ge, M. D. Allendorf, G. Chen, F. Léonard and M. Dincă, *Joule*, 2017, **1**, 168–177.

190 D. Maspoch, D. Ruiz-Molina and J. Veciana, *J Mater Chem*, 2004, **14**, 2713–2723.

191 M. Kurmoo, *Chem Soc Rev*, 2009, **38**, 1353–1379.

192 M. Clemente-Leon, E. Coronado, C. Marti-Gastaldo and F. M. Romero, *Chem Soc Rev*, 2011, **40**, 473–497.

193 D.-F. Weng, Z.-M. Wang and S. Gao, *Chem Soc Rev*, 2011, **40**, 3157–3181.

194 E. Coronado and G. Minguez Espallargas, *Chem. Soc. Rev.*, 2013, **42**, 1525–1539.

195 T. Grancha, J. Ferrando-Soria, M. Castellano, M. Julve, J. Pasan, D. Armentano and E. Pardo, *Chem Commun*, 2014, **50**, 7569–7585.

196 K. Liu, X. Zhang, X. Meng, W. Shi, P. Cheng and A. K. Powell, *Chem Soc Rev*, 2016, **45**, 2423–2439.

197 G. Mínguez Espallargas and E. Coronado, *Chem. Soc. Rev.*, 2018, **47**, 533–557.

198 E. Coronado, *Nat. Rev. Mater.*, 2020, **5**, 87–104.

199 A. E. Thorarinsdottir and T. D. Harris, *Chem. Rev.*, , DOI:10.1021/acs.chemrev.9b00666.

200 O. Kahn and C. J. Martinez, *Science*, 1998, **279**, 44–48.

201 J.-F. Létard, P. Guionneau, L. Goux-Capes, P. Gütlich and H. A. Goodwin, *Spin Crossover Transit. Met. Compd. III*, 2004, **235**, 221–249.

202 C.-M. Jureschi, J. Linares, A. Boulmaali, P. Dahoo, A. Rotaru and Y. Garcia, *Sensors*, 2016, **16**, 187.

203 C. Lefter, V. Davesne, L. Salmon, G. Molnár, P. Demont, A. Rotaru and A. Bousseksou, *Magnetochemistry*, 2016, **2**, 18.

204 K. S. Kumar and M. Ruben, *Coord Chem Rev*, 2017, **346**, 176–205.

205 A. Bousseksou, Ed., *Comptes Rendus Chim.*, 2018, **21**, 1055–1300.

206 Y. Garcia, V. Niel, M. C. Muñoz and J. A. Real, in *Spin Crossover in Transition Metal Compounds I*, Springer Berlin Heidelberg, Berlin, Heidelberg, P. Gütlich and H. A. Goodwin., 2004, vol. 223, pp. 229–257.

207 G. Molnár, M. Mikolasek, K. Ridier, A. Fahs, W. Nicolazzi and A. Bousseksou, *Ann. Phys.*, 2019, **531**, 1900076.

208 J. A. Real, A. B. Gaspar and M. C. Munoz, *Dalton Trans*, 2005, **0**, 2062–2079.

209 A. Bousseksou, G. Molnár, L. Salmon and W. Nicolazzi, *Chem Soc Rev*, 2011, **40**, 3313–3335.
210 P. Gütlich, A. B. Gaspar and Y. Garcia, *Beilstein J Org Chem*, 2013, **9**, 342–391.
211 A. B. Gaspar, G. Molnár, A. Rotaru and H. J. Shepherd, *Comptes Rendus Chim.*, 2018, **21**, 1095–1120.
212 G. Chastanet, M. Lorenc, R. Bertoni and C. Desplanches, *Comptes Rendus Chim.*, 2018, **21**, 1075–1094.
213 S. Brooker, *Chem Soc Rev*, 2015, **44**, 2880–2892.
214 J. A. Real, A. B. Gaspar, V. Niel and M. C. Muñoz, *Coord Chem Rev*, 2003, **236**, 121–141.
215 M. Nihei, T. Shiga, Y. Maeda and H. Oshio, *Coord Chem Rev*, 2007, **251**, 2606–2621.
216 K. S. Murray, *Eur J Inorg Chem*, 2008, **2008**, 3101–3121.
217 A. B. Gaspar, M. Seredyuk and P. Gütlich, *J Mol Struct*, 2009, **924–926**, 9–19.
218 J. Olguín, *Coord. Chem. Rev.*, 2020, **407**, 213148.
219 K. A. Hofmann and F. Küspert, *Z Anorg Allg Chem*, 1897, **15**, 204–207.
220 M. C. Muñoz and J. A. Real, *Coord Chem Rev*, 2011, **255**, 2068–2093.
221 Z.-P. Ni, J.-L. Liu, M. N. Hoque, W. Liu, J.-Y. Li, Y.-C. Chen and M.-L. Tong, *Coord. Chem. Rev.*, 2017, **335**, 28–43.
222 R. Ohtani and S. Hayami, *Chem. - Eur. J.*, 2017, **23**, 2236–2248.
223 G. Agustí, R. Ohtani, K. Yoneda, A. B. Gaspar, M. Ohba, J. F. Sánchez-Royo, M. C. Muñoz, S. Kitagawa and J. A. Real, *Angew Chem Int Ed*, 2009, **48**, 8944–8947.
224 P. D. Southon, L. Liu, E. A. Fellows, D. J. Price, G. J. Halder, K. W. Chapman, B. Moubaraki, K. S. Murray, J.-F. Létard and C. J. Kepert, *J. Am. Chem. Soc.*, 2009, **131**, 10998–11009.
225 C. Bartual-Murgui, N. A. Ortega-Villar, H. J. Shepherd, M. C. Munoz, L. Salmon, G. Molnar, A. Bousseksou and J. A. Real, *J Mater Chem*, 2011, **21**, 7217–7222.
226 C. Bartual-Murgui, A. Akou, L. Salmon, G. Molnár, C. Thibault, J. A. Real and A. Bousseksou, *Small*, 2011, **7**, 3385–3391.
227 C. Bartual-Murgui, L. Salmon, A. Akou, N. A. Ortega-Villar, H. J. Shepherd, M. C. Muñoz, G. Molnár, J. A. Real and A. Bousseksou, *Chem. – Eur. J.*, 2012, **18**, 507–516.
228 F. J. Muñoz-Lara, A. B. Gaspar, M. C. Muñoz, M. Arai, S. Kitagawa, M. Ohba and J. A. Real, *Chem. – Eur. J.*, 2012, **18**, 8013–8018.
229 F. J. Muñoz Lara, A. B. Gaspar, D. Aravena, E. Ruiz, M. C. Muñoz, M. Ohba, R. Ohtani, S. Kitagawa and J. A. Real, *Chem Commun*, 2012, **48**, 4686–4688.
230 F. J. Muñoz-Lara, A. B. Gaspar, M. C. Muñoz, V. Ksenofontov and J. A. Real, *Inorg. Chem.*, 2013, **52**, 3–5.
231 X. Bao, H. J. Shepherd, L. Salmon, G. Molnár, M.-L. Tong and A. Bousseksou, *Angew. Chem. Int. Ed.*, 2013, **52**, 1198–1202.
232 L. Pineiro-Lopez, M. Seredyuk, M. C. Munoz and J. A. Real, *Chem Commun*, 2014, **50**, 1833–1835.
233 L. Piñeiro-López, F. J. Valverde-Muñoz, M. Seredyuk, M. C. Muñoz, M. Haukka and J. A. Real, *Inorg. Chem.*, 2017, **56**, 7038–7047.
234 C. D. Polyzou, N. Lalioti, V. Psycharis and V. Tangoulis, *New J Chem*, 2017, **41**, 12384–12387.
235 F.-L. Liu, D. Li, L.-J. Su and J. Tao, *Dalton Trans*, 2018, **47**, 1407–1411.
236 M. Ohba, K. Yoneda, G. Agustí, M. C. Muñoz, A. B. Gaspar, J. A. Real, M. Yamasaki, H. Ando, Y. Nakao, S. Sakaki and S. Kitagawa, *Angew. Chem. Int. Ed.*, 2009, **48**, 4767–4771.
237 D. Aravena, Z. A. Castillo, M. C. Muñoz, A. B. Gaspar, K. Yoneda, R. Ohtani, A. Mishima, S. Kitagawa, M. Ohba, J. A. Real and E. Ruiz, *Chem. – Eur. J.*, 2014, **20**, 12864–12873.
238 A. Mishima, T. Koshiyama, J. A. Real and M. Ohba, *J Mater Chem C*, 2017, **5**, 3706–3713.
239 H. Ando, Y. Nakao, H. Sato, M. Ohba, S. Kitagawa and S. Sakaki, *Chem. Phys. Lett.*, 2011, **511**, 399–404.
240 M. M. Deshmukh, M. Ohba, S. Kitagawa and S. Sakaki, *J. Am. Chem. Soc.*, 2013, **135**, 4840–4849.
241 M. J. Murphy, K. A. Zenere, F. Ragon, P. D. Southon, C. J. Kepert and S. M. Neville, *J. Am. Chem. Soc.*, 2017, **139**, 1330–1335.
242 N. F. Sciortino, F. Ragon, Y. M. Klein, C. E. Housecroft, C. G. Davies, G. N. L. Jameson, G. Chastanet and S. M. Neville, *Inorg. Chem.*, 2018, **57**, 11068–11076.
243 K. A. Zenere, S. G. Duyker, E. Trzop, E. Collet, B. Chan, P. W. Doheny, C. J. Kepert and S. M. Neville, *Chem Sci*, 2018, **9**, 5623–5629.
244 S. Sakaida, K. Otsubo, O. Sakata, C. Song, A. Fujiwara, M. Takata and H. Kitagawa, *Nat Chem*, 2016, **8**, 377–383.
245 T. Haraguchi, K. Otsubo and H. Kitagawa, *Eur J Inorg Chem*, 2018, **2018**, 1697–1706.
246 V. Rubio-Giménez, G. Escorcia-Ariza, C. Bartual-Murgui, C. Sternemann, M. Galbiati, J. Castells-Gil, J. Real, S. Tatay and C. Martí-Gastaldo, *Chem. Mater.*, 2019, **31**, 7277–7287.
247 V. Martínez, A. B. Gaspar, M. C. Muñoz, R. Ballesteros, N. Ortega-Villar, V. M. Ugalde-Saldívar, R. Moreno-Esparza and J. A. Real, *Eur. J. Inorg. Chem.*, 2009, **2009**, 303–310.
248 W. Xue, B.-Y. Wang, J. Zhu, W.-X. Zhang, Y.-B. Zhang, H.-X. Zhao and X.-M. Chen, *Chem Commun*, 2011, **47**, 10233–10235.
249 B. Djukic and M. T. Lemaire, *Inorg. Chem.*, 2009, **48**, 10489–10491.
250 L. Poggini, M. Gonidec, J. H. González-Estefan, G. Pecastaings, B. Gobaut and P. Rosa, *Adv. Electron. Mater.*, 2018, **4**, 1800204.
251 L. Poggini, M. Gonidec, R. K. Canjeevaram Balasubramanyam, L. Squillantini, G. Pecastaings, A. Caneschi and P. Rosa, *J Mater Chem C*, 2019, **7**, 5343–5347.
252 J. G. Haasnoot, *Coord. Chem. Rev.*, 2000, **200–202**, 131–185.
253 A. Grosjean, P. Négrier, P. Bordet, C. Etrillard, D. Mondieig, S. Pechev, E. Lebraud, J.-F. Létard and P. Guionneau, *Eur. J. Inorg. Chem.*, 2013, **2013**, 796–802.
254 E. Coronado, J. R. Galán-Mascarós, M. Monrabal-Capilla, J. García-Martínez and P. Pardo-Ibáñez, *Adv. Mater.*, 2007, **19**, 1359–1361.
255 C. Lefter, I. A. Gural'skiy, H. Peng, G. Molnár, L. Salmon, A. Rotaru, A. Bousseksou and P. Demont, *Phys. Status Solidi RRL – Rapid Res. Lett.*, 2014, **8**, 191–193.
256 C. Lefter, S. Tricard, H. Peng, G. Molnár, L. Salmon, P. Demont, A. Rotaru and A. Bousseksou, *J. Phys. Chem. C*, 2015, **119**, 8522–8529.
257 I. Soroceanu, A. Graur, E. Coca, L. Salmon, G. Molnar, P. Demont, A. Bousseksou and A. Rotaru, *J. Phys. Chem. Lett.*, 2019, **10**, 7391–7396.
258 A. Rotaru, I. A. Gural'skiy, G. Molnar, L. Salmon, P. Demont and A. Bousseksou, *Chem Commun*, 2012, **48**, 4163–4165.
259 A. Rotaru, J. Dugay, R. P. Tan, I. A. Guralskiy, L. Salmon, P. Demont, J. Carrey, G. Molnár, M. Respaud and A. Bousseksou, *Adv Mater*, 2013, **25**, 1745–1749.
260 C. Lefter, R. Tan, J. Dugay, S. Tricard, G. Molnár, L. Salmon, J. Carrey, W. Nicolazzi, A. Rotaru and A. Bousseksou, *Chem. Phys. Lett.*, 2016, **644**, 138–141.
261 A. Diaconu, S.-L. Lupu, I. Rusu, I.-M. Risca, L. Salmon, G. Molnár, A. Bousseksou, P. Demont and A. Rotaru, *J. Phys. Chem. Lett.*, 2017, **8**, 3147–3151.

262 J. Dugay, M. Giménez-Marqués, T. Kozlova, H. W. Zandbergen, E. Coronado and H. S. J. van der Zant, *Adv. Mater.*, 2015, **27**, 1288–1293.
263 A. Holovchenko, J. Dugay, M. Giménez-Marqués, R. Torres-Cavanillas, E. Coronado and H. S. J. van der Zant, *Adv Mater*, 2016, **28**, 7228–7233.
264 J. Dugay, W. Evers, R. Torres-Cavanillas, M. Giménez-Marqués, E. Coronado and H. S. J. Van der Zant, *J. Phys. Chem. Lett.*, 2018, **9**, 5672–5678.
265 P. Ferry, M.-C. María, O. E. A, C. Eugenio and van der Z. H. S. J, *Adv. Mater.*, 2011, **23**, 1545–1549.
266 R. Torres-Cavanillas, R. Sanchis-Gual, J. Dugay, M. Coronado-Puchau, M. Giménez-Marqués and E. Coronado, *Adv. Mater.*, 2019, **0**, 1900039.
267 M. S. Alam, M. Stocker, K. Gieb, P. Müller, M. Haryono, K. Student and A. Grohmann, *Angew. Chem. Int. Ed.*, 2010, **49**, 1159–1163.
268 E. J. Devid, P. N. Martinho, M. V. Kamalakar, I. Šalitroš, Ú. Prendergast, J.-F. Dayen, V. Meded, T. Lemma, R. González-Prieto, F. Evers, T. E. Keyes, M. Ruben, B. Doudin and S. J. van der Molen, *ACS Nano*, 2015, **9**, 4496–4507.
269 C. Lefter, S. Rat, J. S. Costa, M. D. Manrique-Juárez, C. M. Quintero, L. Salmon, I. Séguy, T. Leichle, L. Nicu, P. Demont, A. Rotaru, G. Molnár and A. Bousseksou, *Adv. Mater.*, 2016, **28**, 7508–7514.
270 Y. Zhang, I. Séguy, K. Ridier, V. Shalabaeva, M. Piedrahita-Bello, A. Rotaru, L. Salmon, G. Molnár and A. Bousseksou, *J. Phys. Condens. Matter*, 2020, **32**, 214010.
271 X. Zhang, S. Mu, G. Chastanet, N. Daro, T. Palamarciuc, P. Rosa, J.-F. Létard, J. Liu, G. E. Sterbinsky, D. A. Arena, C. Etrillard, B. Kundys, B. Doudin and P. A. Dowben, *J. Phys. Chem. C*, 2015, **119**, 16293–16302.
272 O. Sato, T. Kawakami, M. Kimura, S. Hishiya, S. Kubo and Y. Einaga, *J. Am. Chem. Soc.*, 2004, **126**, 13176–13177.
273 N. Shimamoto, S. Ohkoshi, O. Sato and K. Hashimoto, *Inorg. Chem.*, 2002, **41**, 678–684.
274 K. R. Dunbar, C. Achim and M. Shatruk, in *Spin-Crossover Materials*, John Wiley & Sons, Ltd, 2013, pp. 171–202.
275 D. Aguilà, Y. Prado, E. S. Koumousi, C. Mathonière and R. Clérac, *Chem Soc Rev*, 2016, **45**, 203–224.
276 Y.-S. Meng, O. Sato and T. Liu, *Angew. Chem. Int. Ed.*, 2018, **57**, 12216–12226.
277 G. Molnár, S. Cobo, T. Mahfoud, E. J. M. Vertelman, P. J. van Koningsbruggen, P. Demont and A. Bousseksou, *J. Phys. Chem. C*, 2009, **113**, 2586–2593.
278 T. Mahfoud, G. Molnár, S. Bonhommeau, S. Cobo, L. Salmon, P. Demont, H. Tokoro, S.-I. Ohkoshi, K. Boukheddaden and A. Bousseksou, *J. Am. Chem. Soc.*, 2009, **131**, 15049–15054.
279 N. Hoshino, F. Iijima, G. N. Newton, N. Yoshida, T. Shiga, H. Nojiri, A. Nakao, R. Kumai, Y. Murakami and H. Oshio, *Nat. Chem.*, 2012, **4**, 921–926.
280 P. Horcajada, C. Serre, D. Grosso, C. Boissière, S. Perruchas, C. Sanchez and G. Férey, *Adv. Mater.*, 2009, **21**, 1931–1935.
281 A. Demessence, P. Horcajada, C. Serre, C. Boissière, D. Grosso, C. Sanchez and G. Férey, *Chem Commun*, 2009, 7149–7151.
282 A. Demessence, C. Boissière, D. Grosso, P. Horcajada, C. Serre, G. Férey, G. J. A. A. Soler-Illia and C. Sanchez, *J Mater Chem*, 2010, **20**, 7676–7681.
283 R. Dong, T. Zhang and X. Feng, *Chem Rev*, 2018, **118**, 6189–6235.
284 H. Maeda, R. Sakamoto and H. Nishihara, *Langmuir*, 2016, **32**, 2527–2538.
285 R. Sakamoto, K. Takada, T. Pal, H. Maeda, T. Kambe and H. Nishihara, *Chem Commun*, 2017, **53**, 5781–5801.
286 C. Lingyun, W. Tingting and W. Cheng, *C Chin J Chem*, 2018, **36**, 754–764.
287 D. J. Ashworth and J. A. Foster, *J Mater Chem A*, 2018, **6**, 16292–16307.
288 W. Liu, R. Yin, X. Xu, L. Zhang, W. Shi and X. Cao, *Adv. Sci.*, 2019, **6**, 1802373.
289 R. Sakamoto, T. Yagi, K. Hoshiko, S. Kusaka, R. Matsuoka, H. Maeda, Z. Liu, Q. Liu, W.-Y. Wong and H. Nishihara, *Angew Chem Int Ed*, 2017, **56**, 3526–3530.
290 Y.-N. Li, S. Wang, Y. Zhou, X.-J. Bai, G.-S. Song, X.-Y. Zhao, T.-Q. Wang, X. Qi, X.-M. Zhang and Y. Fu, *Langmuir*, 2017, **33**, 1060–1065.
291 X. Bai, D. Chen, L. Li, L. Shao, W. He, H. Chen, Y. Li, X. Zhang, L. Zhang, T. Wang, Y. Fu and W. Qi, *ACS Appl Mater Interfaces*, 2018, **10**, 25960–25966.
292 I. Langmuir, *J Am Chem Soc*, 1917, **39**, 1848–1906.
293 R. Makiura, S. Motoyama, Y. Umemura, H. Yamanaka, O. Sakata and H. Kitagawa, *Nat Mater*, 2010, **9**, 565–571.
294 I. Langmuir and V. J. Schaefer, *J Am Chem Soc*, 1937, **59**, 2400–2414.
295 R. Makiura and H. Kitagawa, *Eur J Inorg Chem*, 2010, **2010**, 3715–3724.
296 R. Makiura, K. Tsuchiyama and O. Sakata, *CrystEngComm*, 2011, **13**, 5538–5541.
297 S. Motoyama, R. Makiura, O. Sakata and H. Kitagawa, *J Am Chem Soc*, 2011, **133**, 5640–5643.
298 R. Makiura and O. Konovalov, *Dalton Trans*, 2013, **42**, 15931–15936.
299 R. Makiura and O. Konovalov, *Sci Rep*, 2013, **3**, 2506.
300 R. Makiura, R. Usui, Y. Sakai, A. Nomoto, A. Ogawa, O. Sakata and A. Fujiwara, *ChemPlusChem*, 2014, **79**, 1352–1360.
301 K. Hoshiko, T. Kambe, R. Sakamoto, K. Takada and H. Nishihara, *Chem Lett*, 2014, **43**, 252–253.
302 Y. Jiang, G. H. Ryu, S. H. Joo, X. Chen, S. H. Lee, X. Chen, M. Huang, X. Wu, D. Luo, Y. Huang, J. H. Lee, B. Wang, X. Zhang, S. K. Kwak, Z. Lee and R. S. Ruoff, *ACS Appl Mater Interfaces*, 2017, **9**, 28107–28116.
303 M. Moradi, L. G. Tulli, J. Nowakowski, M. Baljozovic, T. A. Jung and P. Shahgaldian, *Angew Chem Int Ed*, 2017, **56**, 14395–14399.
304 V. Rubio-Giménez, S. Tatay, F. Volatron, F. J. Martínez-Casado, C. Martí-Gastaldo and E. Coronado, *J. Am. Chem. Soc.*, 2016, **138**, 2576–2584.
305 M. Tsotsalas, A. Umemura, F. Kim, Y. Sakata, J. Reboul, S. Kitagawa and S. Furukawa, *J Mater Chem*, 2012, **22**, 10159–10165.
306 J. Benito, S. Sorribas, I. Lucas, J. Coronas and I. Gascon, *ACS Appl Mater Interfaces*, 2016, **8**, 16486–16492.
307 A. Ciesielski and P. Samorì, *Chem Soc Rev*, 2014, **43**, 381–398.
308 M. Yi and Z. Shen, *J Mater Chem A*, 2015, **3**, 11700–11715.
309 M. I. Kairi, S. Dayou, N. I. Kairi, S. A. Bakar, B. Vigolo and A. R. Mohamed, *J Mater Chem A*, 2018, **6**, 15010–15026.
310 X. Huang, Z. Zeng and H. Zhang, *Chem Soc Rev*, 2013, **42**, 1934–1946.
311 H. Li, J. Wu, Z. Yin and H. Zhang, *Acc. Chem. Res.*, 2014, **47**, 1067–1075.
312 J. Yu, Q. Wang, D. O'Hare and L. Sun, *Chem Soc Rev*, 2017, **46**, 5950–5974.
313 V. Nicolosi, M. Chhowalla, M. G. Kanatzidis, M. S. Strano and J. N. Coleman, *Science*, , DOI:10.1126/science.1226419.
314 C. Tan, X. Cao, X.-J. Wu, Q. He, J. Yang, X. Zhang, J. Chen, W. Zhao, S. Han, G.-H. Nam, M. Sindoro and H. Zhang, *Chem Rev*, 2017, **117**, 6225–6331.

315 Z. Meiting, L. Qipeng, M. Qinglang and Z. Hua, *Small Methods*, 2017, **1**, 1600030.
316 Q. Zeng, L. Wang, Y. Huang, S.-L. Zheng, Y. He, J. He, W.-M. Liao, G. Xu, M. Zeller and Z. Xu, *Chem Commun*, 2020, **56**, 3645–3648.
317 B. J. Córdova Wong, D. Xu, S.-S. Bao, L.-M. Zheng and J. Lei, *ACS Appl. Mater. Interfaces*, 2019, **11**, 12986–12992.
318 S. Suárez-García, N. N. Adarsh, G. Molnár, A. Bousseksou, Y. Garcia, M. M. Dîrtu, J. Saiz-Poseu, R. Robles, P. Ordejón and D. Ruiz-Molina, *ACS Appl. Nano Mater.*, 2018, **1**, 2662–2668.
319 J. López-Cabrelles, S. Mañas-Valero, I. J. Vitórica-Yrezábal, P. J. Bereciartua, J. A. Rodríguez-Velamazán, J. C. Waerenborgh, B. J. C. Vieira, D. Davidovikj, P. G. Steeneken, H. S. J. van der Zant, G. Mínguez Espallargas and E. Coronado, *Nat Chem*, 2018, **10**, 1001–1007.
320 A. Gallego, C. Hermosa, O. Castillo, I. Berlanga, C. J. Gómez-García, E. Mateo-Martí, J. I. Martínez, F. Flores, C. Gómez-Navarro, J. Gómez-Herrero, S. Delgado and F. Zamora, *Adv Mater*, 2013, **25**, 2141–2146.
321 B. Garai, A. Mallick, A. Das, R. Mukherjee and R. Banerjee, *Chem Eur J*, 2018, **23**, 7361–7366.
322 C. Kutzscher, A. Gelbert, S. Ehrling, C. Schenk, I. Senkovska and S. Kaskel, *Dalton Trans*, 2017, **46**, 16480–16484.
323 Y. Ding, Y.-P. Chen, X. Zhang, L. Chen, Z. Dong, H.-L. Jiang, H. Xu and H.-C. Zhou, *J Am Chem Soc*, 2017, **139**, 9136–9139.
324 M. Arnold, P. Kortunov, D. J. Jones, Y. Nedellec, J. Kärger and J. Caro, *Eur. J. Inorg. Chem.*, 2007, **2007**, 60–64.
325 D. Zacher, A. Baunemann, S. Hermes and R. A. Fischer, *J Mater Chem*, 2007, **17**, 2785–2792.
326 C.-W. Kung, T.-H. Chang, L.-Y. Chou, J. T. Hupp, O. K. Farha and K.-C. Ho, *Chem Commun*, 2015, **51**, 2414–2417.
327 A. Huang, H. Bux, F. Steinbach and J. Caro, *Angew. Chem. Int. Ed.*, 2010, **49**, 4958–4961.
328 A. Huang, W. Dou and J. Caro, *J. Am. Chem. Soc.*, 2010, **132**, 15562–15564.
329 G. Blanita, G. Borodi, M. D. Lazar, A.-R. Biris, L. Barbu-Tudoran, I. Coldea and D. Lupu, *RSC Adv*, 2016, **6**, 25967–25974.
330 Y. Yoo and H.-K. Jeong, *Chem Commun*, 2008, 2441–2443.
331 H. Bux, F. Liang, Y. Li, J. Cravillon, M. Wiebcke and J. Caro, *J. Am. Chem. Soc.*, 2009, **131**, 16000–16001.
332 O. M. Yaghi, G. Li and H. Li, *Chem. Mater.*, 1997, **9**, 1074–1076.
333 A. Schoedel, C. Scherb and T. Bein, *Angew. Chem. Int. Ed.*, 2010, **49**, 7225–7228.
334 US7968739B2, 2007, 5.
335 R. Ameloot, L. Stappers, J. Fransaer, L. Alaerts, B. F. Sels and D. E. De Vos, *Chem. Mater.*, 2009, **21**, 2580–2582.
336 I. Stassen, M. Styles, G. Grenci, H. V. Gorp, W. Vanderlinden, S. D. Feyter, P. Falcaro, D. D. Vos, P. Vereecken and R. Ameloot, *Nat Mater*, 2016, **15**, 304–310.
337 X. Ma, P. Kumar, N. Mittal, A. Khlyustova, P. Daoutidis, K. A. Mkhoyan and M. Tsapatsis, *Science*, 2018, **361**, 1008–1011.
338 M. Krishtab, I. Stassen, T. Stassin, A. J. Cruz, O. O. Okudur, S. Armini, C. Wilson, S. De Gendt and R. Ameloot, *Nat Commun*, 2019, **10**, 3729.
339 A. J. Cruz, I. Stassen, M. Krishtab, K. Marcoen, T. Stassin, S. Rodríguez-Hermida, J. Teyssandier, S. Pletincx, R. Verbeke, V. Rubio-Giménez, S. Tatay, C. Martí-Gastaldo, J. Meersschaut, P. M. Vereecken, S. De Feyter, T. Hauffman and R. Ameloot, *Chem. Mater.*, 2019, **31**, 9462–9471.
340 T. Stassin, S. Rodríguez-Hemida, B. Schrode, A. J. Cruz, F. Carraro, D. Kravchenko, V. Creemers, I. Stassen, T. Hauffman, D. E. De Vos, P. Falcaro, R. Resel and R. Ameloot, *Chem Commun*, 2019, **55**, 10056–10059.
341 T. Stassin, I. Stassen, N. Wauteraerts, A. J. Cruz, M. Kräuter, A. M. Coclite, D. De Vos and R. Ameloot, *Eur. J. Inorg. Chem.*, 2020, **2020**, 71–74.
342 T. Stassin, I. Stassen, J. Marreiros, A. J. Cruz, R. Verbeke, M. Tu, H. Reinsch, M. Dickmann, W. Egger, I. F. J. Vankelecom, D. E. De Vos and R. Ameloot, *Chem. Mater.*, 2020, **32**, 1784–1793.
343 K. B. Lausund and O. Nilsen, *Nat Commun*, 2016, **7**, 13578.
344 K. B. Lausund, V. Petrovic and O. Nilsen, *Dalton Trans*, 2017, **46**, 16983–16992.
345 D. D. Medina, J. M. Rotter, Y. Hu, M. Dogru, V. Werner, F. Auras, J. T. Markiewicz, P. Knochel and T. Bein, *J. Am. Chem. Soc.*, 2015, **137**, 1016–1019.
346 E. Virmani, J. M. Rotter, A. Mähringer, T. von Zons, A. Godt, T. Bein, S. Wuttke and D. D. Medina, *J Am Chem Soc*, 2018, **140**, 4812–4819.
347 H. Lee, L. J. Kepley, H. G. Hong, S. Akhter and T. E. Mallouk, *J. Phys. Chem.*, 1988, **92**, 2597–2601.
348 C. M. Bell, S. W. Keller, V. M. Lynch and T. E. Mallouk, *Mater Chem Phys*, 1993, **35**, 225–232.
349 H. C. Yang, K. Aoki, H. G. Hong, D. D. Sackett, M. F. Arendt, S. L. Yau, C. M. Bell and T. E. Mallouk, *J. Am. Chem. Soc.*, 1993, **115**, 11855–11862.
350 A. Katsuhiko, Y. Yusuke, R. Gaulthier, J. Qingmin, Y. Yusuke, W. K. C.-W and H. J. P, *Chem Lett*, 2014, **43**, 36–68.
351 O. Shekhah, H. Wang, D. Zacher, R. A. Fischer and C. Wöll, *Angew Chem Int Ed*, 2009, **48**, 5038–5041.
352 O. Zybaylo, O. Shekhah, H. Wang, M. Tafipolsky, R. Schmid, D. Johannsmann and C. Woll, *Phys Chem Chem Phys*, 2010, **12**, 8093–8098.
353 A. Bétard and R. A. Fischer, *Chem Rev*, 2012, **112**, 1055–1083.
354 J. Liu and C. Woll, *Chem Soc Rev*, 2017, **46**, 5730–5770.
355 H. Gliemann and C. Wöll, *Mater Today*, 2012, **15**, 110–116.
356 L. Heinke, H. Gliemann, P. Tremouilhac and C. Wöll, in *The Chemistry of Metal-Organic Frameworks: Synthesis, Characterization, and Applications*, Wiley-VCH Verlag GmbH & Co. KGaA, 2016, pp. 523–550.
357 D. Zacher, O. Shekhah, C. Woll and R. A. Fischer, *Chem Soc Rev*, 2009, **38**, 1418–1429.
358 O. Shekhah, J. Liu, R. A. Fischer and Ch. Woll, *Chem Soc Rev*, 2011, **40**, 1081–1106.
359 D. Zacher, K. Yusenko, A. Bétard, S. Henke, M. Molon, T. Ladnorg, O. Shekhah, B. Schüpbach, T. de los Arcos, M. Krasnopolski, M. Meilikhov, J. Winter, A. Terfort, C. Wöll and R. A. Fischer, *Chem Eur J*, 2011, **17**, 1448–1455.
360 J.-L. Zhuang, A. Terfort and C. Wöll, *Coord Chem Rev*, 2016, **307**, 391–424.
361 D. Zacher, R. Schmid, C. Wöll and R. A. Fischer, *Angew Chem Int Ed*, 2011, **50**, 176–199.
362 Z.-G. Gu and J. Zhang, *Coord Chem Rev*, 2019, **378**, 513–532.
363 T. P. Vello, M. Strauss, C. A. R. Costa, C. C. Corrêa and C. C. Bof Bufon, *Phys Chem Chem Phys*, 2020, **22**, 5839–5846.
364 P. Falcaro, K. Okada, T. Hara, K. Ikigaki, Y. Tokudome, A. W. Thornton, A. J. Hill, T. Williams, C. Doonan and M. Takahashi, *Nat Mater*, 2016, **16**, 342–348.
365 K. Ikigaki, K. Okada, Y. Tokudome, T. Toyao, P. Falcaro, C. J. Doonan and M. Takahashi, *Angew. Chem. Int. Ed.*, 2019, **58**, 6886–6890.
366 O. Shekhah, H. Wang, S. Kowarik, F. Schreiber, M. Paulus, M. Tolan, C. Sternemann, F. Evers, D. Zacher, R. A. Fischer and C. Wöll, *J Am Chem Soc*, 2007, **129**, 15118–15119.
367 C. Munuera, O. Shekhah, H. Wang, C. Woll and C. Ocal, *Phys Chem Chem Phys*, 2008, **10**, 7257–7261.

368 Z.-G. Gu, A. Pfriem, S. Hamsch, H. Breitwieser, J. Wohlgemuth, L. Heinke, H. Gliemann and C. Wöll, *Microporous Mesoporous Mater.*, 2015, **211**, 82–87.
369 H. K. Arslan, O. Shekhah, D. C. F. Wieland, M. Paulus, C. Sternemann, M. A. Schroer, S. Tiemeyer, M. Tolan, R. A. Fischer and C. Wöll, *J Am Chem Soc*, 2011, **133**, 8158–8161.
370 Y.-Y. Wang, S.-M. Chen, R. Haldar, C. Wöll, Z.-G. Gu and J. Zhang, *Adv Mater Interfaces*, 2018, **5**, 1800985.
371 O. Shekhah, *Materials*, 2010, **3**, 1302–1315.
372 S. Wannapaiboon, M. Tu and R. A. Fischer, *Adv. Funct. Mater.*, 2014, **24**, 2696–2705.
373 K. Khaletskaya, S. Turner, M. Tu, S. Wannapaiboon, A. Schneemann, R. Meyer, A. Ludwig, G. Van Tendeloo and R. A. Fischer, *Adv. Funct. Mater.*, 2014, **24**, 4804–4811.
374 S. Wannapaiboon, M. Tu, K. Sumida, K. Khaletskaya, S. Furukawa, S. Kitagawa and R. A. Fischer, *J Mater Chem A*, 2015, **3**, 23385–23394.
375 M. Tu, S. Wannapaiboon, K. Khaletskaya and R. A. Fischer, *Adv. Funct. Mater.*, 2015, **25**, 4470–4479.
376 W. Guo, M. Zha, Z. Wang, E. Redel, Z. Xu and C. Wöll, *ACS Appl. Mater. Interfaces*, 2016, **8**, 24699–24702.
377 Z. Zhou, M.-X. Li, L. Wang, X. He, T. Chi and Z.-X. Wang, *Cryst. Growth Des.*, 2017, **17**, 6719–6724.
378 M. R. Tchalala, P. M. Bhatt, K. N. Chappanda, S. R. Tavares, K. Adil, Y. Belmabkhout, A. Shkurenko, A. Cadiau, N. Heymans, G. De Weireld, G. Maurin, K. N. Salama and M. Eddaoudi, *Nat. Commun.*, 2019, **10**, 1328.
379 N. L. Torad, S. Zhang, W. A. Amer, M. M. Ayad, M. Kim, J. Kim, B. Ding, X. Zhang, T. Kimura and Y. Yamauchi, *Adv. Mater. Interfaces*, 2019, **6**, 1900849.
380 M.-S. Yao, X.-J. Lv, Z.-H. Fu, W.-H. Li, W.-H. Deng, G.-D. Wu and G. Xu, *Angew Chem Int Ed*, 2017, **56**, 16510–16514.
381 V. Chernikova, O. Shekhah and M. Eddaoudi, *ACS Appl Mater Interfaces*, 2016, **8**, 20459–20464.
382 H. K. Arslan, O. Shekhah, J. Wohlgemuth, M. Franzreb, R. A. Fischer and C. Wöll, *Adv Funct Mater*, 2011, **21**, 4228–4231.
383 S. Vozar, Y.-C. Poh, T. Serbowicz, M. Bachner, P. Podsiadlo, M. Qin, E. Verploegen, N. Kotov and A. J. Hart, *Rev. Sci. Instrum.*, 2009, **80**, 023903–023903.
384 S. Cobo, G. Molnár, J. A. Real and A. Bousseksou, *Angew Chem Int Ed*, 2006, **45**, 5786–5789.
385 G. Molnár, S. Cobo, J. A. Real, F. Carcenac, E. Daran, C. Vieu and A. Bousseksou, *Adv Mater*, 2007, **19**, 2163–2167.
386 G. Agustí, S. Cobo, A. B. Gaspar, G. Molnár, N. O. Moussa, P. Á. Szilágyi, V. Pálfi, C. Vieu, M. Carmen Muñoz, J. A. Real and A. Bousseksou, *Chem Mater*, 2008, **20**, 6721–6732.
387 A. Akou, C. Bartual-Murgui, K. Abdul-Kader, M. Lopes, G. Molnár, C. Thibault, C. Vieu, L. Salmon and A. Bousseksou, *Dalton Trans*, 2013, **42**, 16021–16028.
388 K. Otsubo, T. Haraguchi, O. Sakata, A. Fujiwara and H. Kitagawa, *J Am Chem Soc*, 2012, **134**, 9605–9608.
389 T. Haraguchi, K. Otsubo, O. Sakata, A. Fujiwara and H. Kitagawa, *Inorg Chem*, 2015, **54**, 11593–11595.
390 T. Haraguchi, K. Otsubo, O. Sakata, S. Kawaguchi, A. Fujiwara and H. Kitagawa, *Chem Commun*, 2016, **52**, 6017–6020.
391 T. Haraguchi, K. Otsubo, O. Sakata, A. Fujiwara and H. Kitagawa, *J Am Chem Soc*, 2016, **138**, 16787–16793.
392 S. Sakaida, T. Haraguchi, K. Otsubo, O. Sakata, A. Fujiwara and H. Kitagawa, *Inorg Chem*, 2017, **56**, 7606–7609.
393 V. Rubio-Giménez, C. Bartual-Murgui, M. Galbiati, A. Núñez-López, J. Castells-Gil, B. Quinard, P. Seneor, E. Otero, P. Ohresser, A. Cantarero, E. Coronado, J. A. Real, R. Mattana, S. Tatay and C. Martí-Gastaldo, *Chem Sci*, 2019, **10**, 4038–4047.
394 I. Stassen, D. De Vos and R. Ameloot, *Chem Eur J*, 2016, **22**, 14452–14460.
395 P. Sundberg and M. Karppinen, *Eur. J. Inorg. Chem.*, 2014, **2014**, 968–974.
396 J. E. Bratvold, G. Carraro, D. Barreca and O. Nilsen, *Appl. Surf. Sci.*, 2015, **347**, 861–867.
397 E. Ahvenniemi and M. Karppinen, *Dalton Trans*, 2016, **45**, 10730–10735.
398 D. J. Hagen, L. Mai, A. Devi, J. Sainio and M. Karppinen, *Dalton Trans*, 2018, **47**, 15791–15800.
399 L. D. Salmi, M. J. Heikkilä, E. Puukilainen, T. Sajavaara, D. Grosso and M. Ritala, *Microporous Mesoporous Mater*, 2013, **182**, 147–154.
400 M. Nisula, J. Linnera, A. J. Karttunen and M. Karppinen, *Chem. – Eur. J.*, 2017, **23**, 2988–2992.
401 A. Ghazy, M. Safdar, M. Lastusaari and M. Karppinen, *Chem Commun*, 2020, **56**, 241–244.
402 A. Tanskanen and M. Karppinen, *Sci Rep*, 2018, **8**, 8976.
403 A. Khayyami, A. Philip and M. Karppinen, *Angew. Chem. Int. Ed.*, 2019, **58**, 13400–13404.
404 J. Heiska, M. Nisula, E.-L. Rautama, A. J. Karttunen and M. Karppinen, *Dalton Trans*, 2020, **49**, 1591–1599.
405 M. D. Manrique-Juárez, S. Rat, L. Salmon, G. Molnár, C. M. Quintero, L. Nicu, H. J. Shepherd and A. Bousseksou, *Coord. Chem. Rev.*, 2016, **308**, 395–408.
406 H. J. Shepherd, G. Molnár, W. Nicolazzi, L. Salmon and A. Bousseksou, *Eur. J. Inorg. Chem.*, 2013, **2013**, 653–661.
407 M. Mikolasek, G. Félix, W. Nicolazzi, G. Molnár, L. Salmon and A. Bousseksou, *New J Chem*, 2014, **38**, 1834–1839.
408 L. Salmon and L. Catala, *Comptes Rendus Chim.*, 2018, **21**, 1230–1269.
409 T. Mallah and M. Cavallini, *Comptes Rendus Chim.*, 2018, **21**, 1270–1286.
410 C. D. Polyzou and V. Tangoulis, *J. Coord. Chem.*, 2019, **72**, 389–418.
411 I. Boldog, A. B. Gaspar, V. Martínez, P. Pardo-Ibañez, V. Ksenofontov, A. Bhattacharjee, P. Gütlich and J. A. Real, *Angew. Chem. Int. Ed.*, 2008, **47**, 6433–6437.
412 F. Volatron, L. Catala, E. Rivière, A. Gloter, O. Stéphan and T. Mallah, *Inorg. Chem.*, 2008, **47**, 6584–6586.
413 V. Martínez, I. Boldog, A. B. Gaspar, V. Ksenofontov, A. Bhattacharjee, P. Gütlich and J. A. Real, *Chem. Mater.*, 2010, **22**, 4271–4281.
414 J. Larionova, L. Salmon, Y. Guari, A. Tokarev, K. Molvinger, G. Molnár and A. Bousseksou, *Angew. Chem. Int. Ed.*, 2008, **47**, 8236–8240.
415 H. Peng, S. Tricard, G. Félix, G. Molnár, W. Nicolazzi, L. Salmon and A. Bousseksou, *Angew Chem Int Ed*, 2014, **53**, 10894–10898.
416 J. R. Galán-Mascarós, E. Coronado, A. Forment-Aliaga, M. Monrabal-Capilla, E. Pinilla-Cienfuegos and M. Ceolin, *Inorg. Chem.*, 2010, **49**, 5706–5714.
417 M. Giménez-Marqués, M. L. García-Sanz de Larrea and E. Coronado, *J Mater Chem C*, 2015, **3**, 7946–7953.
418 D. Nieto-Castro, F. A. Garcés-Pineda, A. Moneo-Corcuera, B. Pato-Doldan, F. Gispert-Guirado, J. Benet-Buchholz and J. R. Galán-Mascarós, *Inorg. Chem.*, , DOI:10.1021/acs.inorgchem.9b03284.
419 A. Lapresta-Fernández, M. P. Cuéllar, J. M. Herrera, A. Salinas-Castillo, M. del C. Pegalajar, S. Titos-Padilla, E. Colacio and L. F. Capitán-Vallvey, *J Mater Chem C*, 2014, **2**, 7292–7303.
420 Y. Raza, F. Volatron, S. Moldovan, O. Ersen, V. Huc, C. Martini, F. Brisset, A. Gloter, O. Stephan, A. Bousseksou, L. Catala and T. Mallah, *Chem Commun*, 2011, **47**, 11501–11503.

421 O. Iasco, M.-L. Boillot, A. Bellec, R. Guillot, E. Riviere, S. Mazerat, S. Nowak, D. Morineau, A. Brosseau, F. Miserque, V. Repain and T. Mallah, *J Mater Chem C*, 2017, **5**, 11067–11075.
422 V. Shalabaeva, S. Rat, M. D. Manrique-Juarez, A.-C. Bas, L. Vendier, L. Salmon, G. Molnar and A. Bousseksou, *J Mater Chem C*, 2017, **5**, 4419–4425.
423 M. Ruben and K. S. Kumar, *Angew. Chem. Int. Ed.*, , DOI:10.1002/anie.201911256.
424 Z.-G. Gu, S.-C. Chen, W.-Q. Fu, Q. Zheng and J. Zhang, *ACS Appl Mater Interfaces*, 2017, **9**, 7259–7264.
425 G. Wu, J. Huang, Y. Zang, J. He and G. Xu, *J. Am. Chem. Soc.*, 2016, **139**, 1360–1363.
426 B. Wang, Y. Luo, B. Liu and G. Duan, *ACS Appl. Mater. Interfaces*, , DOI:10.1021/acsami.9b14319.
427 L. E. Kreno, K. Leong, O. K. Farha, M. Allendorf, R. P. Van Duyne and J. T. Hupp, *Chem Rev*, 2012, **112**, 1105–1125.
428 D. J. Wales, J. Grand, V. P. Ting, R. D. Burke, K. J. Edler, C. R. Bowen, S. Mintova and A. D. Burrows, *Chem Soc Rev*, 2015, **44**, 4290–4321.
429 P. Kumar, A. Deep and K.-H. Kim, *TrAC Trends Anal. Chem.*, 2015, **73**, 39–53.
430 F.-Y. Yi, D. Chen, M.-K. Wu, L. Han and H.-L. Jiang, *ChemPlusChem*, 2016, **81**, 675–690.
431 Y. Li, A.-S. Xiao, B. Zou, H.-X. Zhang, K.-L. Yan and Y. Lin, *Polyhedron*, 2018, **154**, 83–97.
432 M. G. Campbell and M. Dincă, *Sensors*, 2017, **17**, 1108.
433 S.-J. Choi and I.-D. Kim, *Electron Mater Lett*, 2018, **14**, 221–260.
434 M. G. Campbell, S. F. Liu, T. M. Swager and M. Dincă, *J Am Chem Soc*, 2015, **137**, 13780–13783.
435 L.-A. Cao, M.-S. Yao, H.-J. Jiang, S. Kitagawa, X.-L. Ye, W.-H. Li and G. Xu, *J Mater Chem A*, 2020, **8**, 9085–9090.
436 M. K. Smith, K. E. Jensen, P. A. Pivak and K. A. Mirica, *Chem Mater*, 2016, **28**, 5264–5268.
437 M. K. Smith and K. A. Mirica, *J Am Chem Soc*, 2017, **139**, 16759–16767.
438 L. Mendecki and K. A. Mirica, *ACS Appl. Mater. Interfaces*, 2018, **10**, 19248–19257.
439 C. Bartual-Murgui, A. Akou, C. Thibault, G. Molnar, C. Vieu, L. Salmon and A. Bousseksou, *J Mater Chem C*, 2015, **3**, 1277–1285.
440 G. Levchenko, G. Bukin, H. Fylymonov, Q. Li, A. B. Gaspar and J. A. Real, *J. Phys. Chem. C*, 2019, **123**, 5642–5646.
441 M. P. Cuéllar, A. Lapresta-Fernández, J. M. Herrera, A. Salinas-Castillo, M. del C. Pegalajar, S. Titos-Padilla, E. Colacio and L. F. Capitán-Vallvey, *Sens. Actuators B Chem.*, 2015, **208**, 180–187.
442 T. Miyamachi, M. Gruber, V. Davesne, M. Bowen, S. Boukari, L. Joly, F. Scheurer, G. Rogez, T. K. Yamada, P. Ohresser, E. Beaurepaire and W. Wulfhekel, *Nat. Commun.*, 2012, **3**, 938 EP-.
443 T. Jasper-Toennies, M. Gruber, S. Karan, H. Jacob, F. Tuczek and R. Berndt, *Nano Lett*, 2017, **17**, 6613–6619.
444 H. J. Shepherd, I. A. Gural'skiy, C. M. Quintero, S. Tricard, L. Salmon, G. Molnár and A. Bousseksou, *Nat. Commun.*, 2013, **4**, 2607.
445 M. D. Manrique-Juárez, F. Mathieu, A. Laborde, S. Rat, V. Shalabaeva, P. Demont, O. Thomas, L. Salmon, T. Leichle, L. Nicu, G. Molnár and A. Bousseksou, *Adv. Funct. Mater.*, 2018, **28**, 1801970.
446 I. A. Gural'skiy, C. M. Quintero, J. S. Costa, P. Demont, G. Molnár, L. Salmon, H. J. Shepherd and A. Bousseksou, *J Mater Chem C*, 2014, **2**, 2949–2955.
447 S. Rat, M. Piedrahita-Bello, L. Salmon, G. Molnár, P. Demont and A. Bousseksou, *Adv Mater*, 2018, **30**, 1705275.
448 Y.-C. Chen, Y. Meng, Z.-P. Ni and M.-L. Tong, *J Mater Chem C*, 2015, **3**, 945–949.
449 Y.-S. Koo and J. R. Galán-Mascarós, *Adv Mater*, 2014, **26**, 6785–6789.